Very Low Frequency Measurements carried out with an Unmanned Aircraft System

Inaugural-Dissertation
zur
Erlangung des Doktorgrades
der Mathematisch-Naturwissenschaftlichen Fakultät
der Universität zu Köln

vorgelegt von

Rudolf Eröss

aus Köln

Köln 2015

Gutachter:

1. Berichterstatter (Betreuer):	Prof. Dr. B. Tezkan
2. Berichterstatter:	Prof. Dr. A. Junge
Tag der mündlichen Prüfung:	24.06.2015

Abstract

The present thesis, for the first time ever, carries out measurements with the Very Low Frequency (VLF) method with an unmanned helicopter. It is a feasibility study to test the applicability of using the VLF method together with an Unmanned Airborne System (UAS). This sensor-platform combination provides fast data acquisition at low cost. Additionally, a UAS is able to carry out surveys over heavily structured or dangerous terrain at low altitudes. This overcomes limitations of ground-based measurements as well as of measurements with manned aircraft.

In the geophysical VLF technique, transfer functions relate the vertical magnetic field to the horizontal field components. These transfer functions contain information about lateral resistivity changes of the subsurface. The presented UAS-VLF measurements are conducted at two sites. As a reference, ground-based VLF and Radiomagnetotellurics (RMT) measurements are carried out additionally to the UAS-VLF measurements. Conception and execution of the measurements is made in cooperation with *Mobile Geophysical Technologies* (Celle, Germany). The components of the UAS are the unmanned helicopter *Scout B1-100* from *Aeroscout* (Lucerne, Switzerland), the *Analogue Digital Unit (ADU)* data logger, and the *Super High-Frequency induction coil Triple (SHFT)* Sensor from *metronix*.

Achieving meaningful results with this novel sensor-platform combination poses several challenges. No information on how to construct a suitable suspension for the devices was available prior to the present study. On the one hand, the suspension has to minimize interferences such as pendulum motions, gyrations, and electromagnetic noise of the helicopter. On the other hand, it must preserve the airworthiness of the helicopter. For this, measurements of the electromagnetic helicopter noise are carried out and influences of sensor rotations on the transfer functions are investigated. It is shown that small rotations have a large impact on the transfer functions. Furthermore, the *ADU* data logger must have a distance of 2 m and the *SHFT* sensor a distance of 4 m to the helicopter. With the help of this information, a suitable suspension was constructed by *Aeroscout*.

A processing algorithm for the measured UAS-VLF data is developed. Two methods are presented to determine the transfer functions for available VLF transmitters in a certain survey area. The transfer functions determined with a bivariate approach are less disturbed than those determined with a scalar approach. A rotation of the transfer functions is performed in order to be able to interpret the transfer functions with the 2D inversion algorithm MARE2DEM. In the last step of the processing, the transfer functions are in some cases shifted in order to obtain meaningful inversion models.

The first UAS-VLF field campaign took place in Wavre, Switzerland. The site is characterized by strong anthropogenic anomalies enabling a first proof-of-concept study for the UAS-VLF method. The second field campaign took place in Cuxhaven, Germany. This site features a salt- to freshwater transition zone. The transfer functions obtained at the respective sites enable to determine the locations of the anomalies correctly. Furthermore, the transfer functions are used to obtain resistivity models of the subsurface. For this, RMT data provide the background resistivities. This is the first time that resistivity models are determined from UAS-VLF measurements. The inversion models obtained with UAS-VLF data agree well with the ground-based VLF and RMT results. It is shown that forward models explain the measured data well and demonstrate the reliability of the information obtained from UAS-VLF measurements.

Kurzzusammenfassung

In dieser Arbeit werden erstmalig geophysikalischen Very Low Frequency (VLF) Messungen zusammen mit einem unbemannten Hubschrauber durchgeführt. Es ist eine Machbarkeitsstudie, welche untersucht ob es möglich ist die VLF Methode mit einem Unmanned Airborne Systems (UAS) zu kombinieren. Diese Kombination ermöglicht eine schnelle und kostengünstige Aufnahme von Messdaten. Darüber hinaus können Daten über schwer zugänglichem oder gefährlichem Gelände in geringer Flughöhe aufgenommen werden. Dies umgeht Einschränkungen sowohl von bodengebundenen Messungen, als auch von Messungen mit bemannten Flugkörpern.

Bei der VLF Methode stellen Transferfunktionen eine Beziehung zwischen der vertikalen magnetischen Feldkomponente und den horizontalen magnetischen Feldkomponenten her. Diese Transferfunktionen enthalten Informationen über laterale Leitfähigkeitsveränderungen im Erdboden. Für zwei unterschiedliche Messgebiete werden UAS-VLF Messungen vorgestellt. Als Referenz dienen parallel durchgeführte, bodengebundene VLF und Radiomagnetotellurik (RMT) Messungen. Die Planung und anschließende Verwirklichung der Messungen wurde in Zusammenarbeit mit *Mobile Geophysical Technologies* (Celle, Deutschland) durchgeführt. Die hierfür verwendeten Komponenten des UAS bestehen aus dem unbemannten Hubschrauber *Scout B1- 100* von *Aeroscout* (Luzern, Schweiz), dem *Analog Digital Unit (ADU)* Datenlogger und dem *Super High Frequency Induktionspulentriple (SHFT)* Sensor von *metronix*.

Um mit dieser neuartigen Sensor-Plattform-Kombination sinnvolle Ergebnisse zu erhalten, müssen einige Herausforderungen gemeistert werden. Bisher stehen keine Informationen darüber zur Verfügung, wie eine Aufhängung für die Geräte zu konstruieren ist. Einerseits muss die Aufhängung den Einfluss etwaiger Störquellen auf die Geräte wie etwa Pendelbewegungen und Vibrationen oder elektromagnetischem Rauschen des Hubschraubers minimieren. Andererseits muss Flugtauglichkeit des unbemannten Hubschraubers erhalten bleiben. Hierfür werden Messungen des elektromagnetischen Hubschrauberrauschens durchgeführt und der Einfluss von Sensorrotationen auf die Übertragungsfunktionen untersucht. Es wird gezeigt, dass bereits kleine Sensordrehungen großen Einfluss auf die Übertragungsfunktionen haben. Außerdem sollte der *ADU* Datenlogger einen Abstand von 2 m und der *SHFT* Sensor einen Abstand von 4 m zum Hubschrauber haben. Anhand dieser Vorgaben ist von *Aeroscout* eine geeignete Aufhängung konstruiert worden.

Für die Auswertung der UAS-VLF Daten wird ein Programmpaket entwickelt. Zwei Berechnungsmethoden werden vorgestellt, welche die Transferfunktionen aus den in einem gegebenen Messgebiet vorhandenen VLF Sendern bestimmen. Auf Übertragungsfunktionen die mit der bivariaten Methode berechnet werden, haben Störungen weniger Einfluss als Übertragungsfunktionen die mit der skalaren Methode berechnet werden. Die berechneten Übertragungsfunktionen werden rotiert um eine Interpretation mit dem MARE2DEM 2D-Inversionsalgorithmus zu ermöglichen. Im letzten Schritt der Datenverarbeitung werden Verschiebungen der Übertragungsfunktionen korrigiert. Dies ist teilweise notwendig um aussagekräftige Inversionsmodelle zu erhalten.

Das erste Gebiet, in welchem UAS-VLF Messungen realisiert wurden, liegt in Wavre in der Schweiz. Hier wird zunächst erprobt ob und wie gut anthropogene Anomalien mit der UAS-VLF Methode detektiert werden können. Das zweite Messgebiet liegt bei Cuxhaven in Deutschland über einem Salz- zu Süßwasserübergang. Die jeweils berechneten Übertragungsfunktionen ermöglichen es, die Position der Anomalien im Untergrund korrekt zu lokalisieren. Die Übertragungsfunktionen können außerdem dazu verwendet werden Leitfähigkeitsmodelle des Untergrunds zu erhalten. Hierfür werden die RMT Daten zur Bestimmung der Hintergrundleitfähigkeiten verwendet. Dies ist das erste mal, dass Leitfähigkeitsmodelle aus gemessenen UAS-VLF Daten abgeleitet werden. Die mit der UAS-VLF Methode bestimmten Positionen der Anomalien im Untergrund stimmen mit den Positionen, welche mit bodengebundenen VLF und RMT Messungen bestimmt wurden, überein. Es wird gezeigt, dass Vorwärtsmodellierungen in der Lage sind die gemessenen UAS-VLF Daten zu erklären und dass sie die Verlässlichkeit der gewonnen Informationen bestätigen.

Contents

Abstract **i**

Kurzzusammenfassung **iii**

Contents **v**

Abbreviations **vii**

1 Introduction **1**
- 1.1 Motivation and Objectives 1
- 1.2 Overview 2

2 Theory **5**
- 2.1 Electromagnetic Theory 5
- 2.2 Very Low Frequency Method 9
  - 2.2.1 Concept of the Method 9
  - 2.2.2 Calculation of the Tipper 11
- 2.3 Radiomagnetotellurics Method 12
- 2.4 Modelling and Inversion 14
  - 2.4.1 Inverse Problem 14
  - 2.4.2 Least Squares Solution 17
  - 2.4.3 Linearization 17
  - 2.4.4 Regularization 18
  - 2.4.5 Occam's Inversion 18
  - 2.4.6 Evaluation of the Modelling Results 19
- 2.5 Radiomagnetotellurics Modelling 19
- 2.6 Very Low Frequency Modelling 20

3 Unmanned Aircraft System **23**
- 3.1 Unmanned Aircraft in General 23
- 3.2 Applied Unmanned Aircraft 24

3.3 Devices and Suspension 26

4 Processing of Very Low Frequency Data 29
4.1 Data Import and Recording Method 29
4.2 Time Series Analysis 31
4.3 Identification of Transmitters 33
4.4 Determination of the Transfer Functions 36
4.5 Validation of the Processing 46
4.6 Rotation of the Transfer Functions 49
4.7 Shift of the Transfer Functions 51

5 Pre Flight Investigations 55
5.1 Noise Measurements 55
5.2 Rotation of the Sensor 69

6 Field Campaigns 79
6.1 Wavre 79
  6.1.1 Survey Area 80
  6.1.2 RMT 81
  6.1.3 VLF 93
6.2 Cuxhaven 104
  6.2.1 Survey Area 104
  6.2.2 RMT 107
  6.2.3 VLF 108

7 Summary and Conclusions 123

8 Outlook 127

References 129

Appendix I

Danksagung V

Erklärung VII

Abbreviations

ADU	**A**nalog/**D**igital Signal Conditioning **U**nit-07
ASCII	**A**merican **S**tandard **C**ode for **I**nformation **I**nterchange
dB	**d**eci**b**el
GPS	**G**lobal **P**ositioning **S**ystem
ICAO	**I**nternational **C**ivil **A**viation **O**rganization
MB	**m**ega**b**yte
RPA	**R**emotely **P**iloted **A**ircraft
ROV	**R**emote **O**perated **V**ehicles
SHFT	**S**uper **H**igh-**F**requency induction coil **T**riple
SI	**I**nternational **S**ystem of Units
UA	**U**nmanned **A**ircraft
UAS	**U**nmanned **A**ircraft **S**ystem
UAV	**U**nmanned **A**erial **V**ehicle
USB	**U**niversal **S**erial **B**us
RMT	**R**adio**m**agneto**t**ellurics
VLF	**V**ery **L**ow **F**requency

1 Introduction

1.1 Motivation and Objectives

The major aim of the present thesis is to answer the question whether it is possible to conduct measurements with the geophysical Very Low Frequency (VLF) method on board of an unmanned aircraft and receive meaningful data. Why should one try to do such a thing, as ground-based measurements and manned aircraft measurements with the VLF method already exist and are well established (e. g. Pedersen et al. [1994]; Bosch and Müller [2005])?

The reason is that measurements on board of an unmanned aircraft have several advantages compared to ground-based measurements. Firstly, an unmanned aircraft can measure over heavily structured or even impassable terrain. It can fly autonomously with a constant velocity over pre-defined profiles, thereby measuring on a regular grid with straight profile lines [Clarke, 2014]. The velocity of an unmanned aircraft can be adapted to the type of geophysical problem investigated. In general, a measurement conducted with an unmanned aircraft covers a greater area in the same time than a ground-based measurement.

In comparison to a manned aircraft, an unmanned aircraft can fly at very low altitudes down to a couple of meters above ground (e. g. Tezkan et al. [2011]). Additionally, unmanned aircraft are able to fly with very slow velocities – especially compared to manned aeroplanes. This enables measurements with a higher accuracy and helps to find even small geophysical anomalies since the electromagnetic fields originating from subsurface anomalies decay with increasing altitude [Pedersen and Oskooi, 2004]. The listed advantages make geophysical measurements on board unmanned aircraft valuable for medium sized survey areas, that is several profiles with profile lengths of several hundred meters.

Several steps need to be taken to enable measurements with the geophysical VLF method combined with an unmanned aircraft and receive meaningful and interpretable data sets. The most important step is to realize a flight. To tackle this hurdle, an appropriate suspension which preserves a stable and safe flight and simultaneously enables low noise environment for the sensor, which is mounted as low as possible, is needed. A logger and a sensor implemented in inappropriate way may result in a perilous double pendulum – endangering safe flight.

The next step is to find survey areas that are adequate for first UAS-VLF measurements. A suitable survey area should contain subsurface anomalies that are detectable under the difficult conditions which a proof-of-concept study poses. For the first measurement campaign, an area with two anthropogenic anomalies is chosen. Here, the system is tested above relatively easy to detect subsurface anomalies. For the second measurement campaign, an area with a more natural target is chosen. It is investigated whether the UAS-VLF method is able to detect a salt- to freshwater transition zone. In both survey areas, ground-based VLF and RMT measurements are carried out firstly as a reference for comparison with the results of the UAS-VLF and secondly also to obtain the background resistivities of the survey areas.

Another important step is an adequate data processing, considering that the sensor is in a certain altitude above ground. First, an appropriate time series processing is performed and a method to identify the used transmitters is defined. Second, a method to determine the transfer functions (scalar or bivariate) is developed – including filtering and other corrections of the resulting transfer functions. Third, a quantitative interpretation of the data using the derived subsurface resistivity models is conducted.

The following questions are addressed in the present thesis:

- Is it possible to perform VLF measurements with an unmanned aircraft and obtain meaningful data?
- What additional problems occur during data processing if data of an UAS is used?
- How can crucial problems – like gyrations of the sensor and airworthiness of the UAS – be solved and how can the received data be processed appropriately?
- Are the subsurface anomalies detectable?
- Is it possible to obtain meaningful resistivity models of the subsurface from the UAS-VLF data?
- Are the obtained UAS-VLF results comparable with ground-based results?
- Do the obtained results agree with results of other geophysical methods?

1.2 Overview

This study is organized as follows. An introductory overview of basic electromagnetic concepts is given in Chapter 2. After this, the concept behind the geophysical methods (VLF and RMT) applied in the present work is explained. For the VLF method, a scalar and a bivariate approach to determine the Tipper is presented. The final sections of Chapter 2 are dedicated to explain the applied modelling and inversion theory. In Chapter 3, the terminology of unmanned aircraft is discussed and the UAS and the applied devices are introduced. Subsequently, the processing of the VLF data is explained step by step in Chapter 4. The first three sections describe the data acquisition method, the time series analysis and how VLF transmitters are identified. Afterwards, in sections four and five, it is described how the determination of the transfer functions is performed for the scalar and for the bivariate approach and the results are verified. The last sections of Chapter 4 describe additional adjustments to the transfer functions. Chapter 5 describes preparative experiments regarding helicopter noise and rotations of the sensor. It draws conclusions for the special suspension that needed to be constructed to enable the UAS-VLF measurements. An overview of the survey areas of the two measuring campaigns is given in Chapter 6. Chapter 6, additionally, presents the modelling and inversion results of the RMT and VLF data of the two measuring campaigns. Finally, in Chapter 7, results of the present work are summarized and suggestions for further research is given in Chapter 8.

2 Theory

The present chapter first gives an introduction into the basics of the electromagnetic theory. Then, the Very Low Frequency (VLF) method is introduced. The possibilities, advantages, and disadvantages of the VLF method regarding geophysical problems are discussed. Subsequently, a description of the Radiomagnetotellurics (RMT) method is presented. At the end of this chapter, the theory underlying the applied modelling and inversion algorithms is explained. Following this general overview, the applied algorithms are described.

2.1 Electromagnetic Theory

Geophysical induction methods are most commonly applied with the goal of determining the electrical resistivities ρ (or electrical conductivities $\sigma = 1/\rho$) of the subsurface. The resistivities ρ of the subsurface vary in many orders of magnitude depending on the properties of the materials in the ground.

In general, clays have different resistivities than rocks. In addition, the resistivities depend on the water saturation of the subsurface material and the salinity of the saturating water also plays an important role for the resistivities. Generally, matter with more free electrons has a lower resistivity than matter with less free electrons [Telford et al., 1990].

The equations that describe the interaction of electromagnetic fields with matter are Maxwell's equations. The Maxwell's equations consist of four coupled first order linear differential equations. They can be written in differential or integral form:

$$\nabla \cdot \mathbf{D} = q \qquad \int_S \mathbf{D} \cdot d\mathbf{S} = \int_V q \cdot dV \tag{1}$$

$$\nabla \cdot \mathbf{B} = 0 \qquad \int_S \mathbf{B} \cdot d\mathbf{S} = 0 \tag{2}$$

$$\nabla \times \mathbf{H} = \frac{\partial \mathbf{D}}{\partial t} + \mathbf{j} \qquad \oint_l \mathbf{H} \cdot d\mathbf{l} = \int_S \left(\mathbf{j} + \frac{\partial \mathbf{D}}{\partial t} \right) \cdot d\mathbf{S} \tag{3}$$

$$\nabla \times \mathbf{E} = -\frac{\partial \mathbf{B}}{\partial t} \qquad \oint_l \mathbf{E} \cdot d\mathbf{l} = -\int_S \frac{\partial \mathbf{B}}{\partial t} \cdot d\mathbf{S} \tag{4}$$

The variables are specified in Table 1. Using Gauss' and Stocks' theorem, Maxwell's equations can be derived in their integral form [Jackson, 1975]. Gauss's law (equation (1)) describes the relationship between the electrical field D and the electric charges q that cause it. Equation (2) states that magnetic fields B are source free, it is called Gauss's law for magnetic fields. Ampère's law (equation (3)) states that fields can be generated in two ways, by line currents $\mathbf{j}$ and displacement currents $\frac{\partial \mathbf{D}}{\partial t}$. Equation (4), Faraday's law, states that a varying magnetic field B causes an electric field E of opposite sign. Of superior importance for geophysical electromagnetic induction methods are equations (3) and (4).

Table 1: Variables and constants used in electrodynamics. Vectors written in bold. Dimensions of the quantities are given in the International System of Units (SI).

Parameter	Symbol	SI Unit
electric field intensity	$\mathbf{E}$	$\frac{\mathrm{V}}{\mathrm{m}}$
electric displacement field (flux density)	$\mathbf{D}$	$\frac{\mathrm{As}}{\mathrm{m}^2}$
magnetic field (flux density)	$\mathbf{B}$	$T = \frac{\mathrm{Vs}}{\mathrm{m}^2}$
magnetic field intensity	$\mathbf{H}$	$\frac{\mathrm{A}}{\mathrm{m}}$
current density	$\mathbf{j}$	$\frac{\mathrm{A}}{\mathrm{m}^2}$
electrical permittivity	$\epsilon = \epsilon_0 \epsilon_r$	$\frac{\mathrm{As}}{\mathrm{Vm}}$
electrical permittivity of free space	$\epsilon_0 = 8.845 \cdot 10^{-12}$	$\frac{\mathrm{As}}{\mathrm{Vm}}$
relative electrical permittivity	ϵ_r	non-dimensional
magnetic permeability	$\mu = \mu_0 \mu_r$	$\frac{\mathrm{Vs}}{\mathrm{Am}}$
permeability of free space	$\mu_0 = 4\pi \cdot 10^{-7}$	$\frac{\mathrm{Vs}}{\mathrm{Am}}$
relative permeability	μ_r	non-dimensional
electrical conductivity	σ	$\frac{\mathrm{A}}{\mathrm{Vm}}$
electrical resistivity	ρ	$\Omega\mathrm{m} = \frac{\mathrm{Vm}}{\mathrm{A}}$
angular frequency	$\omega = 2\pi f$	$\frac{1}{\mathrm{s}}$
frequency	f	$\frac{1}{\mathrm{s}}$

The relation to subsurface matter, which is the target in applied geophysics, is given by Ohm's law:

$$\mathbf{j} = \sigma \mathbf{E} \tag{5}$$

The so called constitutive equations,

$$\mathbf{B} = \mu \mathbf{H} \qquad \mathbf{D} = \varepsilon \mathbf{E} \tag{6}$$

describe firstly the relationship between the electric field intensity $\mathbf{E}$ and the electric displacement field $\mathbf{D}$, and secondly between the magnetic field $\mathbf{B}$ and the magnetic field intensity $\mathbf{H}$ in media. However, they reduce to scalar quantities in isotropic media. For most subsurface materials, the magnetic permeability μ equals the vacuum permeability μ_0. These assumptions are often made in the applied geophysics and are applied in the present thesis.

From the material equations (5) and (6), the telegraph and Helmholtz equations can be derived. These describe the damped propagation of electromagnetic fields. With the two assumptions that outside external sources and in regions of homogeneous conductivity, no free charges exist, and the current density is source free in homogeneous regions, $\nabla\cdot\mathbf{E} = 0$ and $\nabla\cdot\mathbf{j} = 0$. With these simplifications, and by taking the curl of Faraday's law and substituting $\nabla \times \mathbf{B}$ with Ampère's law, the telegraph equation is:

$$\Delta\mathbf{F} = \mu\sigma\frac{\partial}{\partial t}\mathbf{F} + \mu\varepsilon\frac{\partial^2}{\partial^2 t}\mathbf{F} \qquad \mathbf{F} \in \{\mathbf{E}, \mathbf{H}\} \tag{7}$$

The derived equation for $\mathbf{H}$ is identical. The first term on the right contains the conductivity and describes diffusion whereas the second term describes the wave propagation of the field. By Fourier transformation, the wave equation can be transformed into the frequency domain resulting in the Helmholtz equation (with $\partial_t = \mathbf{i}\omega$),

$$\Delta\mathbf{F} = i\omega\mu\sigma\mathbf{F} + \mu\varepsilon\omega^2\mathbf{F} \qquad \mathbf{F} \in \{\mathbf{E}, \mathbf{H}\} \tag{8}$$

with the wavenumber k, which implies the physical properties of media as $k^2 = \mu\varepsilon\omega^2 - i\mu\sigma\omega$. The quasi static approximation ($\mu\varepsilon\omega^2 \ll \mu\sigma\omega$) is commonly applied to equation (7) and (8) and simplifies them to:

$$\Delta\mathbf{F} = \mu\sigma\frac{\partial}{\partial t}\mathbf{F} \qquad \mathbf{F} \in \{\mathbf{E}, \mathbf{H}\} \tag{9}$$

$$\Delta\mathbf{F} = i\omega\mu\sigma\mathbf{F} \qquad \mathbf{F} \in \{\mathbf{E}, \mathbf{H}\} \tag{10}$$

This approximation is valid if conducting currents ($\sigma\mathbf{E}$) are much larger than displacement currents ($\partial_t\mathbf{D}$). However, in high resistivity environments (e. g. an air layer) and high operating frequencies, the validity of the approximation is questionable (e. g. for UAS-VLF modelling).

For a homogeneous half-space equation (10) reduces to:

$$\frac{\partial^2\mathbf{F}}{\partial z^2} = i\omega\mu\sigma\mathbf{F} = k^2\mathbf{F} \qquad \mathbf{F} \in \{\mathbf{E}, \mathbf{H}\} \tag{11}$$

and its general solution,

$$\mathbf{F} = \mathbf{F}_0 e^{-ik} + \mathbf{F}_1 e^{+ik} \tag{12}$$

simplifies to $\mathbf{F}_0 e^{-ik}$ describing an exponential decay with depth z. With the electric field given by **E**=$E_x e^{-ik}$ and the magnetic field given by **B**=$B_y e^{-ik}$ with E_x and B_y interrelated through Faraday's law (equation (4)) follows:

$$\frac{\partial E_x}{\partial z} = -E_{x0} k e^{-kz} = -i\omega B_y = -i\omega B_{y0} e^{-kz} \tag{13}$$

The so called magnetotelluric impedance is then given by the relation of the electric and the magnetic field [Brasse, 2007]:

$$Z(\omega) = \frac{E_{x0}}{B_{y0}} = \frac{i\omega}{k} = \frac{i\omega}{\sqrt{i\omega\mu\sigma}} = \sqrt{\frac{i\omega}{\mu\sigma}} \tag{14}$$

Maxwell's equations (3) and (4) yield to two decoupled sets of equations. With $\partial_x \equiv 0$ and assuming time dependence $e^{i\omega t}$ they become,

$$\partial_y B_z - \partial_z B_y = \mu_0(\sigma E_x + j_x) \quad \partial_z E_x = -i\omega B_y \quad -\partial_y E_x = -i\omega B_z \tag{15}$$

$$\partial_y E_z - \partial_z E_y = i\omega B_x \quad \partial_z B_x = \mu_0(\sigma E_y + j_y) \quad -\partial_y B_x = \mu_0(\sigma E_z + j_z) \tag{16}$$

The first set of equations (i. e. (15)), in which the strike direction is parallel to the **E**-field, is called transverse electric (TE)-mode or E-polarization. The complementary second set of equations (i.e. (16)), in which the strike direction is parallel to the **B**-field, is called transverse magnetic (TM)-mode or B-polarization [Chave and Jones, 2012]. Strike directions for two dimensional models characterize the direction along which a conductivity structure is constant.

The depth where the absolute value of an electromagnetic wave of frequency f has decayed to $1/e$ is defined as skin or penetration depth δ:

$$\delta = \sqrt{\frac{2}{\mu\omega\sigma}} \tag{17}$$

With $\mu = \mu_0$, $\omega = 2\pi/T$ and $\rho = 1/\sigma$ equation (17) becomes an approximation for the skin depth:

$$\delta \approx 500\sqrt{\rho/f} \qquad [\mathrm{m}] \tag{18}$$

Thus, the skin depth is a function of resistivity and frequency.

Another method to determine the depth of investigation is to consider the phase ϕ information of the subsurface, which leads to the equation for $z*$:

$$z^* = \sqrt{\frac{\rho}{\omega\mu}} \sin(\phi) \tag{19}$$

For details on electromagnetic theory it is referred to Jackson [1975], or with a relation to geophysics Telford et al. [1990].

2.2 Very Low Frequency Method

Here, at first, the physical concept behind the VLF method is explained. Subsequently, the methods to calculate the transfer functions are described.

2.2.1 Concept of the Method

The geophysical VLF method is a passive electromagnetic method. It exploits existing radio transmitters (usually used for communication with submarines). VLF transmitters are distributed globally. They use the frequency range of 15 kHz to 30 kHz, the so called VLF band. The possibility to use VLF transmitters to investigate the subsurface was described first by Paal [1965]. Since then, the VLF method is widely used as a near-surface geological mapping tool. An advantage of the VLF method is that there is no need to set up transmitters in the field. This makes measurements easier regarding logistical effort and cheaper compared to methods that need transmitters in the field. The depth of investigation for the available VLF frequencies usually ranges from several meters to 100 m, depending on the resistivity distribution of the subsurface. Since VLF is based on electromagnetic induction, it is sensitive to good conductors. The reason is that in good conductors the current density becomes stronger. One major disadvantage is that it is not possible to derive any direct quantitative information on the electrical properties of the subsurface with the VLF method, it is only possible to detect lateral conductivity changes. To derive a subsurface resistivity distribution is usually the main goal and advantage of geophysical electromagnetic methods. However, VLF is an effective mapping method, large areas can be investigated in a very time efficient way compared to other electromagnetic methods, because the sensor does not require direct contact to the surface. Another disadvantage of the VLF method is the dependency on signals of remote transmitters, that is their existence and quality in terms of signal to noise, in a certain measuring area. The sensitivity of the VLF method to anthropogenic noise sources, such as high voltage power lines or railway lines, can also impede the quality of measured data.

For measurements conducted with the geophysical VLF method, it is necessary to record the vertical magnetic field component H_z and at least one of the horizontal magnetic field components H_x or H_y. Usually, the magnetic fields are measured along a profile. The recorded fields are a combination of the primary fields of VLF transmitters and the secondary fields (induced by the primary fields of VLF transmitters).

The vertical magnetic field component H_z is only present over or in the vicinity of lateral conductivity changes in the subsurface. The primary horizontal magnetic field (created by remote VLF transmitters) induces eddy currents in conductive bodies in the subsurface. These eddy currents create the secondary vertical magnetic field H_z that is essential for the VLF method. In areas without lateral conductivity changes, the H_z component is zero. In other words, the VLF method is able to detect lateral conductivity changes in the subsurface (cf. Figure 1).

Vozoff [1972] assumes that the vertical component of the magnetic field H_z is linearly related to the horizontal components H_x and H_y, resulting in the following relationship:

$$H_z(\omega) = A(\omega) \cdot H_x(\omega) + B(\omega) \cdot H_y(\omega) \qquad (20)$$

This linear relation – the transfer function – between the horizontal and the vertical magnetic field (A, B) is also called the Tipper vector where, ω is the angular frequency and $(H_x, H_y, H_z)^T$ is the complex magnetic field vector [Pedersen et al., 1994].

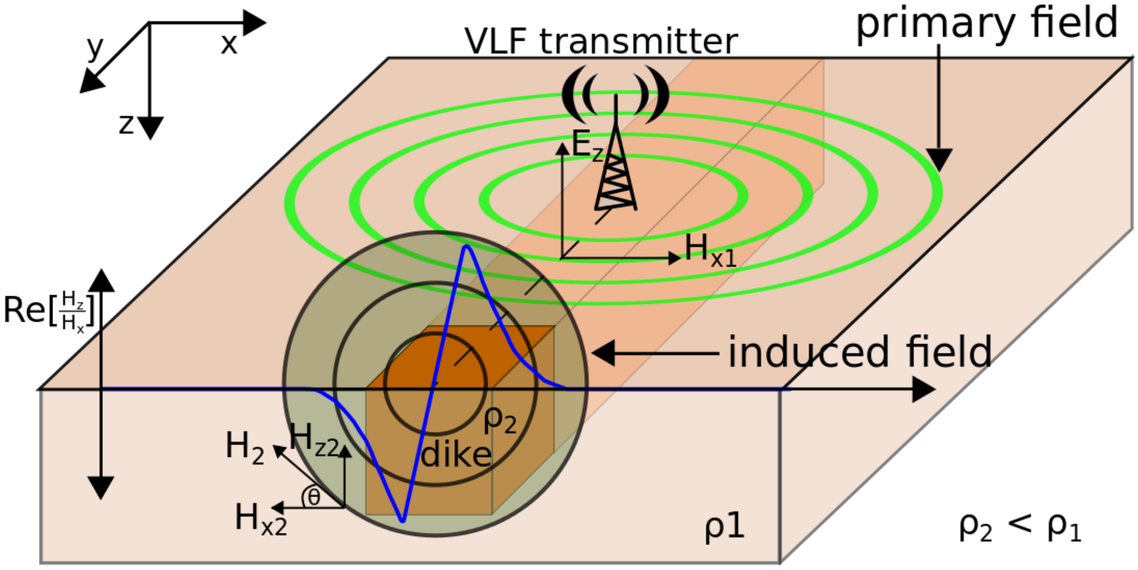

Figure 1: Sketch of the VLF method. The primary magnetic field H_{x1} (green lines), generated by a VLF transmitter, induces eddy currents in a conductive subsurface body. These currents create the secondary magnetic field components H_{x2} and H_{z2} (shaded circles). The blue line shows the real part of the magnetic transfer function (or tipper) B, that is Re(H_z/H_x) = Re(B), along a profile at a selected VLF frequency [Bosch and Müller, 2005; Eröss et al., 2013].

As stated above, the VLF method is only sensitive for lateral conductivity changes. For a layered Earth (one dimensional case), both components of the Tipper vector equal zero. In a two dimensional case, the occurrence of the vertical magnetic field component H_z is utilized. In case of a linear, lateral conductivity change exactly parallel to one of the axes of a chosen coordinate system (geological strike axis), the corresponding Tipper component (orthogonal to the profile) is zero and the other one is not zero (2D case). That is, if the strike of an anomaly is parallel to the y-axis, the B component of the Tipper equals zero and the A component differs from zero.

The common case in the field is that neither A nor B equal zero. This either indicates a three dimensional anomaly or that the strike of the anomaly is not orthogonal to the chosen profile direction, resulting in a contribution to both Tipper components [Vozoff, 1972].

2.2.2 Calculation of the Tipper

In general, one can distinguish between two methods to calculate the tipper: the scalar and the bivariate approach. Both are briefly introduced in the following.

For the scalar approach, it is assumed that the subsurface anomaly (i. e. a good conducting body) is 2D and that one of the axes of the coordinate system is parallel to the anomaly. As a result, one component of the Tipper equals zero [Vozoff, 1972]. In the case of a strike exactly parallel to the y-axis (B = 0), equation (20) simplifies to

$$H_z(\omega) = A(\omega) \cdot H_x(\omega) \tag{21}$$

considering H_z as noise free and the A component of the Tipper can simply be calculated as

$$\frac{H_z(\omega)}{H_x(\omega)} = A(\omega) \tag{22}$$

and vice versa for the B component (after [Pedersen and Oskooi, 2004]). However, Pedersen et al. [1994] describe as a drawback that determining the transfer functions out of a single frequency can bias the result, emphasizing anomalies aligned with the direction of the used transmitter.

The bivariate approach is more complex, but has some advantages. It exploits the fact that often more than one transmitter is available at a certain measuring site and at a certain time. Ideally, the Tipper vector is calculated with two independent measurements at the same angular frequency ω but different transmitter directions (ideally 90°). In reality this is not possible because every transmitter uses a unique frequency and the transmitters are distributed irregularly. Therefore, it is assumed that the Tipper is independent of frequency in the VLF band. In this case, the Tipper can be calculated by all received transmitters or a number of chosen transmitters. Using all the information the different transmitters provide at once leads to a more stable Tipper vector with increasing number of frequencies [Pedersen et al., 1994]. The Tipper vector is calculated via a least squares approach (gennerally explained in e.g. Chave and Jones [2012])

$$\mathbf{T} = (\mathbf{G}^T \cdot \mathbf{G})^{-1} \cdot \mathbf{G}^T \cdot \mathbf{d} \tag{23}$$

with the Tipper vector $\mathbf{T}(\omega)$

$$\mathbf{T}(\omega) = (A(\omega), B(\omega))^T \tag{24}$$

and the M $\times$ N matrix $\mathbf{G}(\omega)$ containing the horizontal components H_x and H_y of the magnetic field,

$$\mathbf{G} = (\mathbf{H}_x(\omega_i), \mathbf{H}_y(\omega_i)) \tag{25}$$

and $\mathbf{d}(\omega) = \mathbf{H}_z(\omega_i)$ the vector containing the vertical magnetic field component H_z at certain frequencies. ω_i indicates the different transmitter frequencies. For example, if only three transmitters are used, $\mathbf{G}$ is a matrix of dimension 3 $\times$ 2 [Hansen et al., 2012].

It is notable that the least squares problem can only be solved if the inverse $(\mathbf{G}^T \cdot \mathbf{G})^{-1}$ exists, which requires det$(\mathbf{G}^T \cdot \mathbf{G})^{-1} \neq 0$. This is the case if transmitters for two or more directions are available. For exact two transmitters of different directions, the least squares solution is exact because in this case equation (23) is a set of two equations and two variables. For transmitters of three or more directions, the solution is a least squares approximation. If all transmitters are in one direction, no additional information is gained and det$(\mathbf{G}^T \cdot \mathbf{G})^{-1}$ can become zero. The reason is that two (linearly) independent realizations are required to find the transfer functions [Hansen et al., 2012].

2.3 Radiomagnetotellurics Method

Figure 2 shows the principle of the Radiomagnetotellurics (RMT) method. Horizontal magnetic and electric fields are measured orthogonal to each other. With the usage of transmitters of different frequencies, a broader range of depths can be investigated compared to VLF. This way, information of the subsurface resistivity distribution is gained. The quantities derived from the measured magnetic and electrical fields are the apparent resistivity ρ_a and the phase ϕ.

Like the VLF method, the RMT method uses radio transmitters, that is no transmitter is needs to be applied in the field. However, the used frequencies are in range from 10 kHz to 1 MHz. Therefore, RMT is a method to investigate depths from few meters up to 100 m and strongly dependent on the resistivity distribution of the subsurface. Similar to VLF, RMT is an induction method and sensitive to good conductors since the induced current densities are stronger in good conductors. Electric fields are measured with grounded electrodes and magnetic fields are measured with inductions coils. The big advantage of the RMT method compared to VLF is the possibility to derive a resistivity model – and thus quantitative information – of the subsurface. As for VLF, disadvantages of the RMT method are the dependency of the quality on foreign transmitter signals and the sensitivity to anthropogenic noise sources such as high voltage power lines or railway lines.

The theory to calculate apparent resistivity ρ_a and phase ϕ is similar to the magnetotelluric

(MT) theory [Cagniard, 1953]. The complex impedance tensor Z specifies the ratio between the measured electric and magnetic fields (Equation 26).

$$\begin{pmatrix} E_x(\omega) \\ E_y(\omega) \end{pmatrix} = \begin{pmatrix} Z_{xx} Z_{xy} \\ Z_{yx} Z_{yy} \end{pmatrix} \begin{pmatrix} H_x(\omega) \\ H_y(\omega) \end{pmatrix} \tag{26}$$

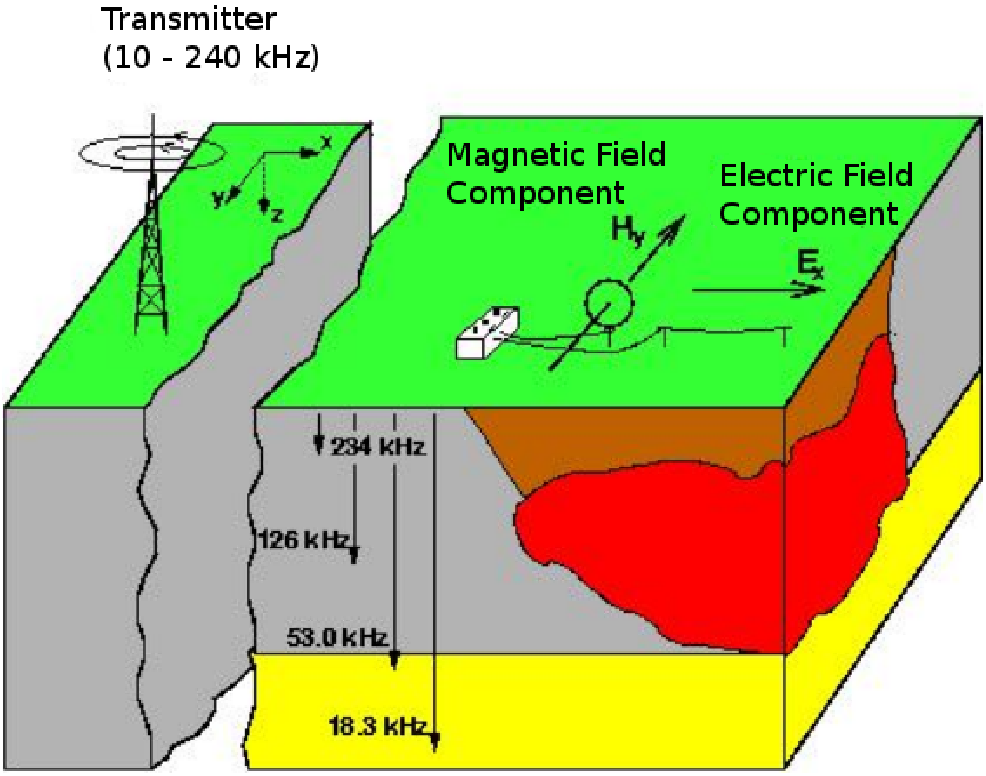

Figure 2: Sketch of the RMT method. The magnetic field H_y generated by a radio transmitter (modified after Recher [2002]).

For a 2D resistivity distribution, two modes can be distinguished. The tangential electric, with the strike of the anomaly parallel to the transmitter direction, and the tangential magnetic, with the strike of the anomaly orthogonal to the transmitter direction. The apparent resistivities ρ_a and phases ϕ for both modes are calculated as follows:

$$\rho_{a_{ij}} = \frac{1}{\omega\mu} |Z_{ij}(\omega)|^2 \tag{27}$$

$$\phi_{ij}(\omega) = arctan\left(\frac{imag(Z_{ij})}{real(Z_{ij})}\right) \qquad \text{, with } i,j \in x,y, i \neq j \tag{28}$$

where μ is the magnetic permeability and ω the angular frequency [Recher, 2002].

2.4 Modelling and Inversion

Measured geophysical field data can usually be used to compute resistivity models of the subsurface, which is the goal of electromagnetic geophysical methods. The search for a resistivity model that explains the measured data well including possible a priori information, is commonly termed inversion. In contrast, the process of computing synthetic data from a constructed resistivity model, is called forward modelling (the obtained data is synthetic since it stems from an artificial model and is not measured). For the inversion process, measured and synthetic data are compared and if they differ (by a certain defined level), the resistivity distribution of the subsurface model is changed (model update) and repeatedly compared with the measured data. This process can be iterated until measured and synthetic data agree to a satisfactory degree. For example, if their deviation falls below a certain defined level. Often experience and time is needed to achieve meaningful models in this way. Since manual model updates are very time consuming even for simple subsurface resistivity distributions, the inversion process can be automated (cf. Figure 3).

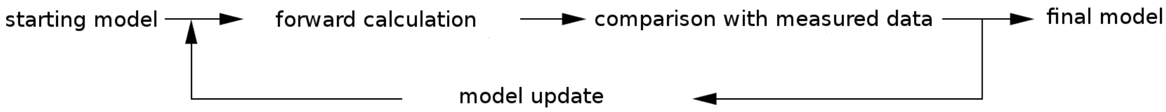

Figure 3: Sketch of the inversion process [Recher, 2002].

Therefore, the inversion uses an iterative scheme – changing the model parameters $\mathbf{m}$ of the subsurface model – to fit the observed data $\mathbf{d}$. The goal is to match measured and synthetic data within a predefined error range [Recher, 2002]. The inversion is repeated iteratively and the model parameters m_k are updated until the predefined goal is achieved or no further improvement is possible:

$$m_{k+1} = m_k + \Delta m_k \tag{29}$$

2.4.1 Inverse Problem

As stated above, the goal of an inversion is to find a resistivity model that explains the (VLF or RMT) data d_i, $i = 1, ..., N$, which contains the measured information. N is the number of measured data. For this, a parametrization of the subsurface represented by the model parameters m_i, $i = 1, ..., M$, is needed. For a more concise notation, the m_j can be considered as components of an M-dimensional column vector $\mathbf{m}$

$$\mathbf{m} = (m_1, m_2, ..., m_M)^T \tag{30}$$

and the observed data $\mathbf{d}$ of components of the N-dimensional column vector [Chave and Jones, 2012]:

$$\mathbf{d} = (d_1, d_2, ..., d_N)^T \tag{31}$$

For an inversion it is necessary to have a so called forward algorithm. This algorithm enables to calculate the synthetic data that would be observed with a given model parametrization. This part of the inversion is called forward problem (equation (32)). The forward calculation derives electromagnetic fields out of geophysical quantities, that is the model parameters that form a resistivity distribution of the subsurface – strait forward – to emphasize: in this part no inversion takes place. In the best case, the measured data $\mathbf{d}$ would equal the forward calculation of the model $\mathbf{m}$,

$$\mathbf{d} = \mathbf{f}(\mathbf{m}) = (f_1(\mathbf{m}), f_2(\mathbf{m}), ..., f_N(\mathbf{m}))^T \text{ , with } i = 1, 2, ..., N \tag{32}$$

which is the transformation from model to data space. Here, the functions f_i are implicitily defined by a code that solves the Maxwell equation. The solution is converted to the appropriate quantity defineing d_i [Chave and Jones, 2012].

Forward Problem

If the physical parameters of the Earth are independent of one Cartesian coordinate (2D case), Rodi and Mackie [2001] show that Maxwell's equations can be decoupled in the transverse electric and transverse magnetic polarization. The source of the electromagnetic fields can be modelled as a current sheet at a height $z = -h$. In the quasi static approximation, to calculate RMT data [Schmucker and Weidelt, 1975], it is enough to solve,

$$\frac{\partial^2 E_x}{\partial y^2} + \frac{\partial^2 E_x}{\partial z^2} = -i\omega\mu\sigma E_x \tag{33}$$

$$\left.\frac{\partial E_x}{\partial z}\right|_{z=-h} = i\omega\mu \tag{34}$$

for the TE-mode with E_x in strike direction and

$$\frac{\partial}{\partial y}\left(\rho\frac{\partial H_x}{\partial y}\right) + \frac{\partial}{\partial z}\left(\rho\frac{\partial H_x}{\partial z}\right) = -i\omega\mu H_x \tag{35}$$

$$\left.H_x\right|_{z=0} = 1 \tag{36}$$

for the TM-mode with E_x orthogonal to strike direction (cf. Section 2.1), where μ is the magnetic permeability and ω the angular frequency. The apparent resistivity of the TE polarization after equation (26) is defined as

$$\rho_a = \frac{1}{\omega\mu}\left(Z_{xy}\right) = \frac{1}{\omega\mu}\left(\frac{E_x}{H_y}\right) \qquad [\Omega m] \tag{37}$$

with H_y implied from Maxwell's equations as

$$H_y = \frac{1}{\omega\mu}\frac{\partial E_x}{\partial z} \tag{38}$$

For the TM polarization it is

$$\rho_a = \frac{1}{\omega\mu}\left(Z_{yx}\right) = \frac{1}{\omega\mu}\left(\frac{E_y}{H_x}\right) \qquad [\Omega m] \tag{39}$$

and

$$E_y = \rho\frac{\partial H_x}{\partial z} \tag{40}$$

Here, the model parameters (resistivities and thicknesses) and the angular frequency are the input parameters of the forward calculation. The forward code calculates the apparent resistivities ρ_a and phases ϕ for given frequencies ω and for a given resistivity model.

However, a model (of discrete parameters) is commonly not able to reproduce measured and thus noisy data. Considering errors in the prediction, data and model parameters of a subsurface model are related in the following way:

$$d_i = f_i(m_1, m_2, ..., m_M) + e_i \text{ , with } i = 1, 2, ..., N \tag{41}$$

With these considerations and assuming the inverse of $\mathbf{f}$ exists (and $\mathbf{e}$ = 0), it is easy to see where the term *inversion* comes from, since the solution of the linear case of equation (41) is

$$\mathbf{m} = \mathbf{f}^{-1}(\mathbf{d}) \tag{42}$$

In other words, solving equation (41) equals finding the inverse of $\mathbf{f}$, which is $\mathbf{f}^{-1}$ [Chave and Jones, 2012].

However, for most problems investigated in geophysical context, the inverse of $\mathbf{f}$ does not exist. Therefore, the goal is to find an estimate of the model $\mathbf{m}$ to explain the measured data $\mathbf{d}$ in the best way. If the data noise is uncorrelated and normally distributed, this can be achieved by a least-squares approach [Chave and Jones, 2012].

2.4.2 Least Squares Solution

Geophysical problems for which the number of unknown model parameters is smaller than the number of data points ($M < N$) are stated over-determined problems. For this kind of over-determined problems, it is possible to use the least squares method to match the measured data as closely as possible or in a predefined way (e. g. RMS), but not exactly. In geophysics, this means to minimize the data misfit or objective function $\Phi_d(\mathbf{m})$, that is the discrepancy between $\mathbf{d}$ and the forward functional $f(\mathbf{m})$=$\mathbf{Gm}$ [Chave and Jones, 2012]

$$\Phi_d(\mathbf{m}) = (\mathbf{d} - \mathbf{Gm})^T(\mathbf{d} - \mathbf{Gm}) \tag{43}$$

Minimization of $\Phi_d(\mathbf{m})$ requires $\frac{\partial\Phi(\mathbf{m})}{\partial\mathbf{m_i}}$=0. Calculating the derivative of $\Phi_d(\mathbf{m})$ with respect to m leads to

$$\mathbf{G}^T\mathbf{Gm} - \mathbf{G}^T\mathbf{d} = 0 \tag{44}$$

If the inverse of $\mathbf{G}^T\mathbf{G}$ exists, the model vector is received by the data vector for this unconstrained least square approach. Solving for m results in the normal equation:

$$\mathbf{m} = (\mathbf{G}^T\mathbf{G})^{-1}\mathbf{G}^T\mathbf{d} \tag{45}$$

2.4.3 Linearization

In geophysics, the relation between $\mathbf{m}$ and $\mathbf{d}$ is often not linear. That is the earth response $f(\mathbf{m})$ is not linear with the change of the physical properties m. However, it is assumed that linear behaviour for very small changes of the properties. In this case, the forward function $f(\mathbf{m})$ can be linearized. The linearization is accomplished by expanding $f(\mathbf{m})$ in a Taylor series around a known model $\mathbf{m_0}$. Then equation (41) can be written as

$$\mathbf{d} = f(\mathbf{m}) = f(\mathbf{m_0}) + \mathbf{A_{m_0}}(\mathbf{m} - \mathbf{m_0}) + R_2 \tag{46}$$

where $A_{\mathbf{m_0}}$ is the matrix of the model parameters of the spatial derivatives of the forward functional. In geophysics, this matrix is called Jacobian or sensitivity matrix

$$[\mathbf{A_{m_0}}]_{ij} = \left.\frac{\partial f_i(\mathbf{m})}{\partial m_j}\right|_{\mathbf{m}=\mathbf{m_0}} \tag{47}$$

R_2 represents terms of second and higher expansion. Neglecting this second and higher expansion terms, the first order approximation of f(**m**) is

$$\tilde{\mathrm{f}}(\mathbf{m};\mathbf{m}_0) = \mathbf{d} = f(\mathbf{m_0}) + \mathbf{A_{m_0}}(\mathbf{m} - \mathbf{m_0}) \tag{48}$$

resulting in the now linearized forward problem $\tilde{\mathrm{f}}$ around model $\mathbf{m_0}$ [Chave and Jones, 2012].

2.4.4 Regularization

In two or three dimensional geophysical modelling problems, the number of model parameters usually increases rapidly. In the more dimensional case, the number of unknown model parameters is larger than the number of data points ($M > N$) and therefore a so called "ill-posed" problem. For such an ill-posed problem, the least squares solution would provide a great number of solutions, or no solution at all (cf. Section 2.4.2). Therefore, a regularization is needed to stabilize the inversion problem. The inversion code from Rodi and Mackie [2001] applied in this work, uses the Tikhonov-regularization [Tikhonov and Arsenin, 1977] to minimize the objective function $\Phi(\mathbf{m})$

$$\Phi(\mathbf{m}) = \Phi_d(\mathbf{m}) + \lambda\,\Omega(\mathbf{m}) \tag{49}$$

$$= (\mathbf{d} - f(\mathbf{m}))(\mathbf{d} - f(\mathbf{m}))^T + \lambda\,|\mathbf{Lm}|^2 \tag{50}$$

as the sum of the data fit (equation (43)) and a regularization term. Ω is called stabilizing functional, λ is the regularization parameter and $\mathbf{L}$ is a differential operator (e. g. second-difference operator [Rodi and Mackie, 2001]). λ denotes the weighting between data fit and model smoothing. The second term is the stabilizing functional on the model. The next section shows how the regularization is used to solve the inversion problem.

2.4.5 Occam's Inversion

The inversion strategy of the algorithms used in the present thesis are based on the so called Occam's inversion [Constable et al., 1987]. For the following derivation see Recher [2002] and Rodi and Mackie [2001]. To solve the inverse problem, a Tikhonov regularization (cf. also equation (50)) is used to minimize the objective function

$$\mathbf{\Phi}(\mathbf{m}) = (\mathbf{d} - f(\mathbf{m}))^T\mathbf{V}^{-1}(\mathbf{d} - f(\mathbf{m})) + \lambda\,\mathbf{m}^T\mathbf{L}^T\mathbf{Lm} \tag{51}$$

$\mathbf{V}$ is the matrix of the variance of the error and the matrix $\mathbf{L}$ acts as a Laplace operator on $\mathbf{m}$. The linearized forward function $f(\mathbf{m})$ around the reference model $\mathbf{m}_0$ is given by (cf. equation (48)),

$$\tilde{\mathrm{f}}(\mathbf{m};\mathbf{m}_0) = f(\mathbf{m}_0) + \mathbf{A}_{\mathbf{m_0}}(\mathbf{m} - \mathbf{m}_0) \tag{52}$$

with the Jacobian $A_{\mathbf{m_0}}$ (cf. equation (46)) the objective function becomes

$$\tilde{\Phi}(\mathbf{m};\mathbf{m}_0) = (\mathbf{d} - \tilde{\mathrm{f}}(\mathbf{m};\mathbf{m}_0))^T\mathbf{V}^{-1}(\mathbf{d} - \tilde{\mathrm{f}}(\mathbf{m};\mathbf{m}_0)) + \lambda\,\mathbf{m}^T\mathbf{L}^T\mathbf{Lm} \tag{53}$$

To calculate the minimum of the objective function, the first $\partial_j\tilde{\Phi}(\mathbf{m};\mathbf{m}_0)$ and second $\partial_j\partial_k\tilde{\Phi}(\mathbf{m};\mathbf{m}_0)$ partial derivatives have to be determined

$$\partial_j \tilde{\Phi}(\mathbf{m};\mathbf{m}_0) = -2\mathbf{A}(\mathbf{m}_0)^T\mathbf{V}^{-1}(\mathbf{d} - \tilde{\mathrm{f}}(\mathbf{m};\mathbf{m}_0)) + 2\lambda\mathbf{L}^T\mathbf{L}\mathbf{m} \tag{54}$$

$$\partial_j\partial_k \tilde{\Phi}(\mathbf{m};\mathbf{m}_0) = 2\mathbf{A}(\mathbf{m}_0)^T\mathbf{V}^{-1}\mathbf{A}(\mathbf{m}_0) + 2\lambda\mathbf{L}^T\mathbf{L}\mathbf{m} \tag{55}$$

Considering the following identities, $\tilde{f}(\mathbf{m}_0;\mathbf{m}_0) = f(\mathbf{m}_0)$, $\partial_j\tilde{\Phi}(\mathbf{m}_0;\mathbf{m}_0) = \partial_j\Phi(\mathbf{m}_0)$ and $\partial_j\partial_k\tilde{\Phi}(\mathbf{m}_0;\mathbf{m}_0) = \partial_j\partial_k\Phi(\mathbf{m}_0)$, the objective function and its gradient can finally be written as:

$$\tilde{\Phi}(\mathbf{m};\mathbf{m}_0) = \Phi(\mathbf{m}_0) + \partial_j\Phi(\mathbf{m}_0)^T(\mathbf{m} - \mathbf{m}_0) \tag{56}$$

$$+ \frac{1}{2}(\mathbf{m} - \mathbf{m}_0)^T\partial_j\partial_k\tilde{\Phi}(\mathbf{m}_0)(\mathbf{m} - \mathbf{m}_0) \tag{57}$$

$$\partial_j\tilde{\Phi}(\mathbf{m};\mathbf{m}_0) = \partial_j\Phi(\mathbf{m}_0) + \partial_j\partial_k\tilde{\Phi}(\mathbf{m}_0)(\mathbf{m} - \mathbf{m}_0) = \mathbf{g}(\mathbf{m};\mathbf{m}_0) \tag{58}$$

2.4.6 Evaluation of the Modelling Results

One way to quantitatively judge the resulting model of an inversion is to regard the root mean square (RMS) error. It is important that the predicted data fits good to the measured data,

$$\mathrm{RMS} = \sqrt{\frac{1}{N}\sum_{i=1}^{N}\frac{(d_i - f(\mathbf{m})_i)^2}{d_i^2}} \tag{59}$$

or in case of the misfit of MARE2DEM models (cf. 2.6)

$$\mathrm{RMS} = \sqrt{\frac{1}{N}\sum_{i=1}^{N}\frac{(d_i - f(\mathbf{m})_i)^2}{1}} \tag{60}$$

The RMS is usually stated in percent. From the RMS value, it is not possible to judge how reliable results of a certain model are. For this, another way to judge the final model is to consider the sensitivities. For this consideration, the Jacobian of the last iteration is used. For example one column contains the partial derivatives of one model parameter. From this, it is possible to see the influence of one model parameter on the response. Finally, with a suitable illustration, it is possible to determine the parts of the model, where the sensitivity is high enough to be meaningful.

2.5 Radiomagnetotellurics Modelling

Rodi and Mackie [2001] present a non linear conjugate gradient algorithm for 2D magnetotelluric finite differences inversion. This algorithm is used for the RMT inversion in the present thesis.

To solve equations (33) to (40), Maxwell's equations are approximated by finite differences [Madden, 1972; Mackie et al., 1993]. The finite difference equations are expressed as a system of linear equations for each polarization and frequency. $E_{x,y}$ and $H_{y,x}$ are now calculated as a linear combination on a given site, interpolating and/or averaging the according horizontal field. The grids used for the finite differences method of the Mackie algorithm are structured grids. The Occam's method (cf. Section 2.4.5) is used for the inversion.

The algorithm presented in Rodi and Mackie [2001] uses the nonlinear conjugate gradients (NLCG) method to avoid the computation of the whole Jacobian, as, for example, required by the Gauss-Newton method. The aim is to iteratively find a global minimum of the objective function Φ – in dependence of the step size α – along the gradient:

$$\tilde{\Phi}(\mathbf{m}_l + \alpha_l \mathbf{p}_l) = \min_{\alpha} \tilde{\Phi}(\mathbf{m}_l + \alpha_l \mathbf{p}_l) \tag{61}$$

$$\mathbf{m}_{l+1} = \mathbf{m}_l + \alpha_l \mathbf{p}_l \qquad \text{l = 0, 1, 2, ..., K} \tag{62}$$

The inversion begins with $\mathbf{m}_0$ and the model sequence is $\mathbf{m}_l$, (l = 0, 1, 2, ..., K). The search direction of the gradient $\mathbf{p}_l$ is determined by the steepest descent direction:

$$\mathbf{p}_0 = -\mathbf{C}_0 \mathbf{g}_0 \tag{63}$$

$$\mathbf{p}_l = -\mathbf{C}_l \mathbf{g}_l + \beta_l \mathbf{p}_{l-1} \qquad \text{l = 0, 1, 2, ..., K} \tag{64}$$

with gradient g of the objective function (cf. equation (58)), using the Polak-Ribiere technique [Polak, 1971],

$$\beta_l = \frac{\mathbf{g}_l^T \mathbf{C}_l (\mathbf{g}_l - \mathbf{g}_{l-1})}{\mathbf{g}_{l-1}^T \mathbf{C}_{l-1} \mathbf{g}_{l-1}} \tag{65}$$

The preconditioner **C** plays an important role to find the gradient,

$$\mathbf{C}_l = (\gamma_l \mathbf{I} + \tau \mathbf{L}^T \mathbf{L})^{-1} \tag{66}$$

where γ_l is a specified scalar. In this form, equation (66) acts like the approximated Hessian. The preconditioner **C** is allowed to vary during the iteration. The use of an adequate preconditioner leads to a faster and more stable determination of $\mathbf{p}_l$. For further information it is referred to Rodi and Mackie [2001]. A user manual for the algorithm is given in Mackie et al. [1997].

2.6 Very Low Frequency Modelling

Key and Ovall [2011] present a parallel finite element algorithm for 2D MT modelling and inversion. Since this algorithm named MARE2DEM is used for the VLF modelling and inversion in the present thesis, the following section gives a brief explanation of the code. The overview is strongly oriented on Key and Ovall [2011] and Key et al. [2012].

In order to solve Maxwell's equations, MARE2DEM uses the finite element method. The FE method approximates an exact solution of a differential equation with a piecewise linear one. After Fourier transformation, the coupled differential Maxwell's equation can be written as

$$-\nabla \cdot (\sigma\lambda\nabla E_x) - \nabla \cdot (ik_x\lambda\nabla H_x) + \sigma E_x = f_1 \tag{67}$$

$$-\nabla \cdot (ik_x\nabla E_x) - \nabla \cdot (i\omega\mu\lambda\nabla H_x) + i\omega\mu H_x = f_2 \tag{68}$$

where

$$\lambda^{-1} = k_x^2 - i\omega\mu\sigma = k_x^2 - \omega^2\mu\epsilon - i\omega\mu\sigma \tag{69}$$

$f_{1,2}$ are source terms and it is assumed that $\lambda^{-1} \neq 0$, which should be true for conductivities in geophysical applications and frequencies not equal to zero.

After the electric field E_x and the magnetic field H_x are determined from equations (67) and (68), the transverse field components are computed. The last step is to convert the 2D wavenumber domain fields into 3D spatial domain fields by utilizing the inverse Fourier transformation [Key and Ovall, 2011]. In other words, the MARE2DEM code uses 2D finite elements to solve for E_x and H_x with the conductivity strike along x. The other field components for the forward calculation are formed from their spatial gradients, so the Tipper is H_z/H_y which is determined from the TE-mode (cf. equations (15)).

For the inversion, the MARE2DEM code uses Occam's method (cf. Section 2.4.5). It is noticeable that for VLF inversions with Tipper data only, the background resistivity is essentially unconstrained in the inversion. However, given a starting model, the code is able to solve for lateral conductivity variations that fit the measured Tipper data. Especially the absolute value of the conductivity of an isolated 2D conductor can be erroneous, but the lateral position of a 2D anomaly is resolved well. Concerning the depth information of a resistivity model obtained by inverting only one frequency (as performed in the present thesis), lateral variation of the tipper data can help to constrain depth of a subsuface structure [Key, 2014].

3 Unmanned Aircraft System

There is a lot of confusion about how to properly name and abbreviate an Unmanned Aircraft System (UAS). The same acronym is often applied for multiple meanings. UAS is also used for Unmanned Aerial System and Unmanned Airborne System. In the past, the same ambiguity appeared for the now obsolete term UAV (Unmanned Aerial Vehicle, Unmanned Air Vehicle) [ICAO, 2011]. The official definition of UAS by the International Civil Aviation Organization (ICAO) in ICAO [2011] is given as: Unmanned aircraft system. An aircraft and its associated elements which are operated with no pilot on board". However, Austin [2011] defines UAS differently:
"An unmanned aircraft system is just that – a system. It must always be considered as such. The system comprises a number of sub-systems which include the aircraft (often referred to as a UAV or unmanned air vehicle), its payloads, the control station(s) (and, often, other remote stations), aircraft launch and recovery sub-systems where applicable, support sub-systems, communication sub-systems, transport sub-systems, etc".

The present thesis uses the latter definition, that is the term UAS is used in an all-encompassing sense, including the Unmanned Aircraft (UA), everything that is needed to operate it and its payloads, that is for the present thesis the electromagnetic devices.

Other denotations such as Remotely Piloted Aircraft (RPA) or Remote Operated Vehicles (ROV) are deliberately not used in the present thesis. An overview on the topic of UA is given in Clarke [2014].

The following sections give a brief overview of UAS in geophysics. The UA used in the present thesis is presented and the applied electromagnetic devices are described as well as the developed suspension.

3.1 Unmanned Aircraft in General

The first reported aerial geophysical survey was carried out by Logachev and Hawkes [1946] from 19 – 21 July in 1936. It was called an "experimental magnetic survey by airplane". Since this first aerial campaign, a lot of time has passed and manned aerial geophysical surveying has become common (e. g. BURVAL [2003]).

In comparison to this, geophysical surveys with UAS are quite recent. A first attempt to carry out geophysical VLF measurements with a UAS was made by Kipfinger [1998]. However, the main result of this study was that the received data was very noisy and a further investigation of the noise (originating from the UA) was proposed. After the UA crashed, further researches became difficult. From today's perspective, one could guess that UAS technology was not sufficiently advanced at the time.

In the previous decade, due to rapid developments in fields such as miniaturization, compute power, positioning, communication combined with the construction of modern aircraft and UAS, the number of developmental initiatives and purposes in geosciences related to UAS increased rapidly. An overview about the developments is given in Colomina and Molina [2014].

Modern UAS have characteristics "such as the ability to hover, to quickly re-orient the aircraft or a device that it carries, to sustain a very steady flight along a pre-determined bearing, to remain airborne for long periods, and to offer flexibility in the choice of take-off and landing locations and conditions" [Clarke, 2014]. They are capable of flying at low altitudes and constant predefined velocities, an advantage when measuring at profiles difficult or impossible to investigate using ground-based measurements. Another obvious but important aspect is that no crew is on board, which might be endangered in critical flight conditions. Additionally, the lower expenditures of UAS compared to manned aircraft projects is also a relevant factor (e. g. less fuel, less people involved). Furthermore, manned aircraft operate at higher altitudes than UAS. This may be a disadvantage as the vertical magnetic field decreases with altitude as $\exp(-2\pi\ h/\lambda)$ where λ is the scale length of a surface conductor and h is the flight height [Pedersen and Oskooi, 2004].

The advantages of UAS compared to manned aircraft and ground-based measurements resulted in the first geophysical measurements using the magnetics method on board an unmanned helicopter [Tezkan et al., 2011]. This successful pilot project was the predecessor of this work. However, whereas Tezkan et al. [2011] used the magnetics method, the VLF method combined with a UA is subject of the present thesis.

3.2 Applied Unmanned Aircraft

The Scout B1-100 UAV (cf. Figure 4), of *Aeroscout* – an unmanned helicopter – is used to carry out the geophysical measurements. The helicopter is 1.3 m high, 3.3 m long, has a width of 1 m and the main rotor diameter is 3.2 m.

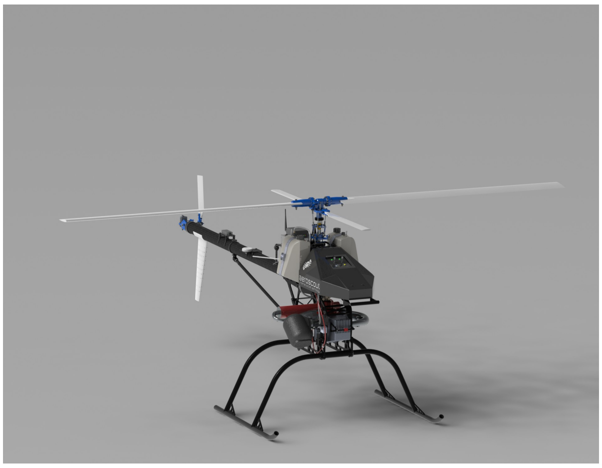

Figure 4: Picture of the Scout B1-100 UAV from Aeroscout [2014], Switzerland.

This UA is capable of 90 minutes autonomous flight. A complete route can be programmed, optionally using a differential Global Positioning System (GPS) for positioning. The payload options are flexible up to 18 kg, a valuable feature for different geophysical methods and their corresponding devices. Table 2 shows the major characteristics of the Scout B1-100 UAV.

Table 2: Technical parameters of the Scout B1-100 UAV [Aeroscout, 2014].

Technical Data	
Main rotor diameter	3.2 m
Tail rotor diameter	0.65 m
Main rotor speed	860 rpm
Empty weight	50 kg
Gasoline engine	100 ccm, 2-stroke
Engine power	18 hp
Electric starter	16 V
Fuel tank volume	2 × 5.0 L (approx. 90 min endurance)
Material of rotor blades	carbon
Material of main body	aluminum
Length	3.3 m
Width	1.0 m
Height	1.3 m
Free payload capacity	18.0 kg

3.3 Devices and Suspension

The Super High-Frequency induction coil Triple (SHFT) sensor and Analog/Digital Signal Conditioning Unit-07 (ADU) data logger from *metronix* are used to carry out the VLF measurements.

The SHFT sensor is able to measure three orthogonal components of the magnetic field simultaneously. The device covers the frequency range from 1 kHz to 300 kHz and it weighs 5.5 kg [metronix SHFT, 2014].

The ADU data logger is able to record signals in the range of 1 Hz to 250 kHz. It weighs 7 kg and is able to record all three magnetic field components simultaneously [metronix ADU, 2014]. Both, the sensor and the data logger are needed to carry out a measurement. To improve the airworthiness, a weight reduction of the devices was realized by Johannes Stoll (*Mobile Geophysical Technologies*) in cooperation with *metronix*.

To be able to carry out the UAS-VLF measurements, an appropriate suspension has to be developed and constructed. In general, the suspension has to fulfil three requirements in order to reduce noise and to enable a stable flight of the UAS. First, the sensor and the logger need to be in a certain distance from each other and the UA to reduce the electromagnetic noise to a tolerable level, that is the signal of an anomaly must be stronger than the noise created by the UA (cf. Section 5.1). Second, vibrations and rotations of the sensor have to be mitigated. Third, pendulum motions of sensor and logger have to be minimized to ensure airworthiness of the UAS and to prevent the sensor from unintended movements. The three described requirements of the suspension were developed jointly with *Aeroscout* and *Mobile Geophysical Technologies*.

A suitable suspension was especially constructed by *Aeroscout* to meet these requirements (Figure 5). The main issue was to find a compromise between a: a short distance between the devices and the helicopter and between the two devices (flight stability) and b: a large distance between the devices to the helicopter and each other (low noise). Investigations regarding the noise dependencies are presented in Section 5.1. Details on how the UAS-VLF measurements are carried out are given in Section 4.1.

A video of a UAS-VLF survey flight is provided on the *Aeroscout* homepage, `http://www.aeroscout.ch/index.php/services` or on YouTube, `https://www.youtube.com/watch?v=Ddz2C6oUNo4`.

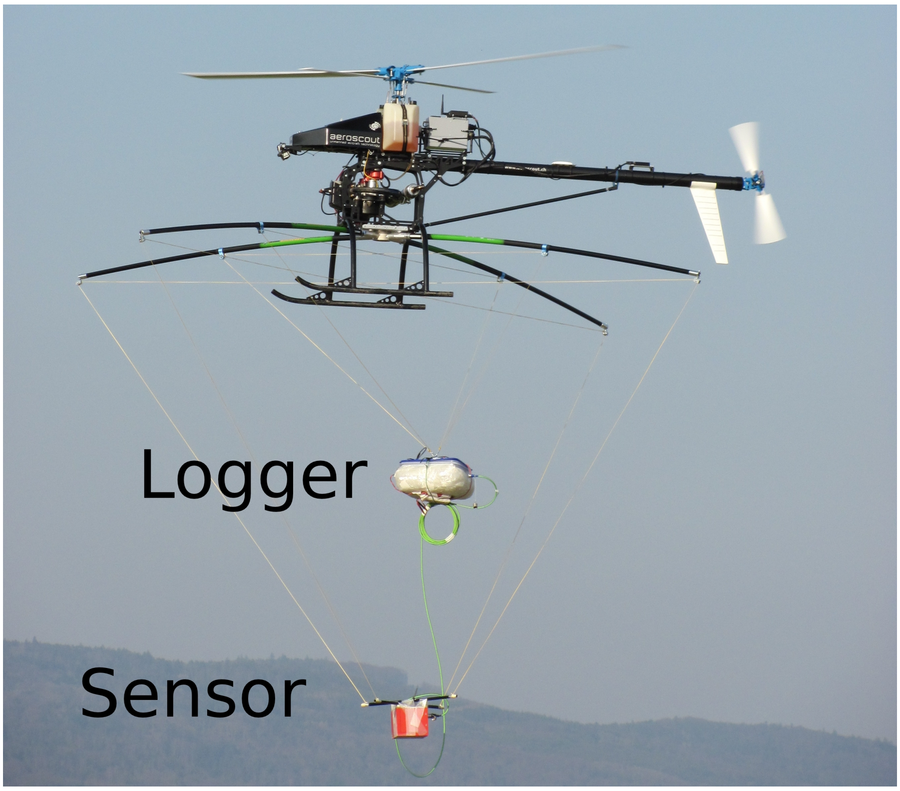

Figure 5: The UAS-VLF system: Scout B1-100 UAV with suspension, ADU-07 logger, and SHFT sensor in action.

4 Processing of Very Low Frequency Data

In this chapter the processing chain is described step by step. For the present thesis, a UAS-VLF data processing tool is developed from scratch. This means the following analysis and processing procedures are self-developed using Matlab. The processing tool imports the data (Section 4.1), discretizes the time series, and afterwards performs a Fourier transformation (Section 4.2). Subsequently, the VLF transmitters are identified (Section 4.3) and the transfer functions are determined with a scalar and a bivariate approach (Section 4.4). To verify the correctness of the new code, the results are compared to those of the robust magnetotelluric data processing approach of Becken [2013] (Section 4.5). After this comparison, a rotation of the transfer function is presented and motivated (Section 4.6). Finally, a possible shift of the transfer functions is motivated and discussed (Section 4.7).

4.1 Data Import and Recording Method

The naming convention of the ADU-07 data files is: 256_V01_C07_R000_THx_BH_65,536H.ats,

- ADU serial number (256)
- XML version – file containing relevant information about the measurement (V01)
- Channel number (C07)
- Run number (R000)
- Channel type (THx)
- Board type (BH)
- Sample rate (65,536 Hz)
- **A**DU **T**ime **S**eries (.ats)

In order to import the data correctly, the channel type and the sample rate are most crucial. Nevertheless, the majority of the information, that is GPS coordinates and measuring time, are included in the header containing the first 1024 bytes of the binary .ats file. This header information is read out by distinguishing between the type of information (INTEGER, FLOAT, CHAR, etc.).

The time series information begins from byte 1,025 of the .ats file. The data type of the time series is LONGINT (INT32). Resulting in a time series of the length of <sample rate × measuring time> samples, or <sample rate × measuring time in seconds × 4 (because of LONGINT)> bytes. As a consequence the data files rapidly become very big for high sampling rates. The ADU-07 is able to sample at different sample rates. For example if the sampling rate is 524,288 Hz and the measuring time is 1 s, the size of the resulting data file is 524,288 × 1 × 4 = 2,097,152 byte = 2.1 megabyte (MB) for one channel, that is one magnetic field component. All three components would make 6.3 MB of data recorded per second. A sampling rate of 65,536 Hz reduces the recorded amount of data per second by almost one magnitude to 0.8 MB.

This potentially large amount of data is remarkable during a field measurement for two reasons. Firstly, the data logger must achieve the requested writing speed to the storage medium. Otherwise, after a short time, the logger aborts the measurement. Secondly, the storage medium must have enough free disk space. For the measurements presented in the present thesis a 3,000 MB Universal Serial Bus (USB) stick is used as data storage.

For stationary measurements (i. e. at fixed locations) for example of 5 s, a sampling rate of 524,288 Hz is feasible (6.3 MB/s, 31.5 MB in total). That is the high sampling rate is no problem for the logger and a USB stick is sufficient if the measurement time is short enough. In contrast, during continuous measurements, where a measurement of a whole profile of hundreds of meters is carried out at once, the data logger will eventually abort the measurement.

For example, one 200 m profile would consist of 1,260 MB of recorded data. Since the writing speed of the logger to the USB stick is probably less than 6.3 MB/s (depending on the stick), temporary storage space of the logger is used. This poses a problem because once the temporary storage is full, the measurement aborts. This occurred several times during the measurement campaigns of the present study, when a high sampling rate was combined with a long recording time.

The problem is the time a UAS-VLF measurement takes. A measurement consists of several steps:
1. A measurement begins by plugging the USB stick in the logger, before the helicopter takes off and flies to the start of the profile (during this time, data is already recorded).
2. Subsequently, the helicopter has to carry out the measurement along a profile (e. g. 350 m).
3. Usually, the helicopter turns around and carries out a second measurement on a neighbouring profile on the return flight.
4. Finally, the UAS flies back to the take off point and need to touch down safely.
This whole process can take 20 minutes or more. For a sampling rate of 524,288 Hz per second, the collected data sum up to 7,560 MB of time series data. Therefore, in the present study, a sampling rate of 65,536 Hz is used for the UAS-VLF measurements. Though a lower sampling rate still produces a huge amount of data (depending on profile length and number),

but is feasible for UAS-VLF measurements. However, for fast writing USB stick with enough storage capacities, a sample rate of 524,288 is feasible. Nevertheless, this would not solve processing problems caused by data where one single file is around 400 MB and more – keeping in mind that the time series are saved in binary format, which is a very efficient way of data storage compared to other standards (e. g. American Standard Code for Information Interchange (ASCII)). However, the converted data files are much larger than they are in binary format and thus it is even more time consuming to work with them.

The applied solution to circumvent the generated big VLF-UAS data files is to note the exact plug-in time of the USB stick by hand. From the plug-in time the begin time of the measurement is known. Secondly, to extract the actual profile data of the UAS-VLF measurements, the fly by time at profile meter zero is noted. With a predefined profile length and a constant speed of the UAS of 1 m/s, the essential part of the .ats file is cut out, reducing the amount of data significantly. This process has the downside that the moment at which the UAS is atop profile meter zero is determined by visual judgement and thus imprecise. An obvious solution for the future could be an accurate GPS that is synchronized with the logger.

4.2 Time Series Analysis

Even if the part of the .ats files with the time series of a profile is separated into different files, the time series are still very large. As a consequence, matrix operations frequently cause "memory overflow" errors. Thus, the time series are cut in sections of 1 s, that is one time series section contains the number of the samples recorded in 1 s (cf. Figure 6).

Subsequently, a cosine taper is applied to reduce the effect of spectral leakage [Harris, 1978] caused by the Fourier transformation of a time series of finite length [Bloomfield, 2004]. To visualize this processing step, a section of $\sim$8k samples is cut out exemplarily. The cosine taper decreases the time series at its begin and end smoothingly to zero (cf. Figure 7). Periodic and unperiodic noise features are visible in the magnetic field components H_x and H_y with variations in amplitude. In the H_z component a noise spike is visible between sample 3,000 and 4,000.

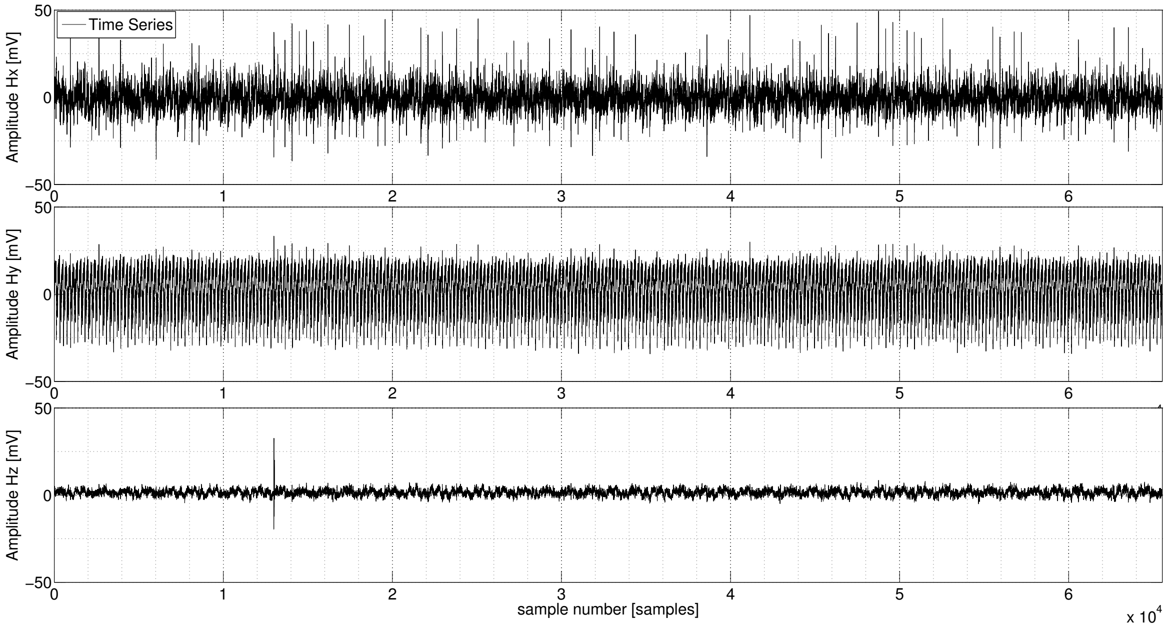

Figure 6: Raw time series of an UAS measurement of ∼65k samples (1 s) of the three magnetic field components.

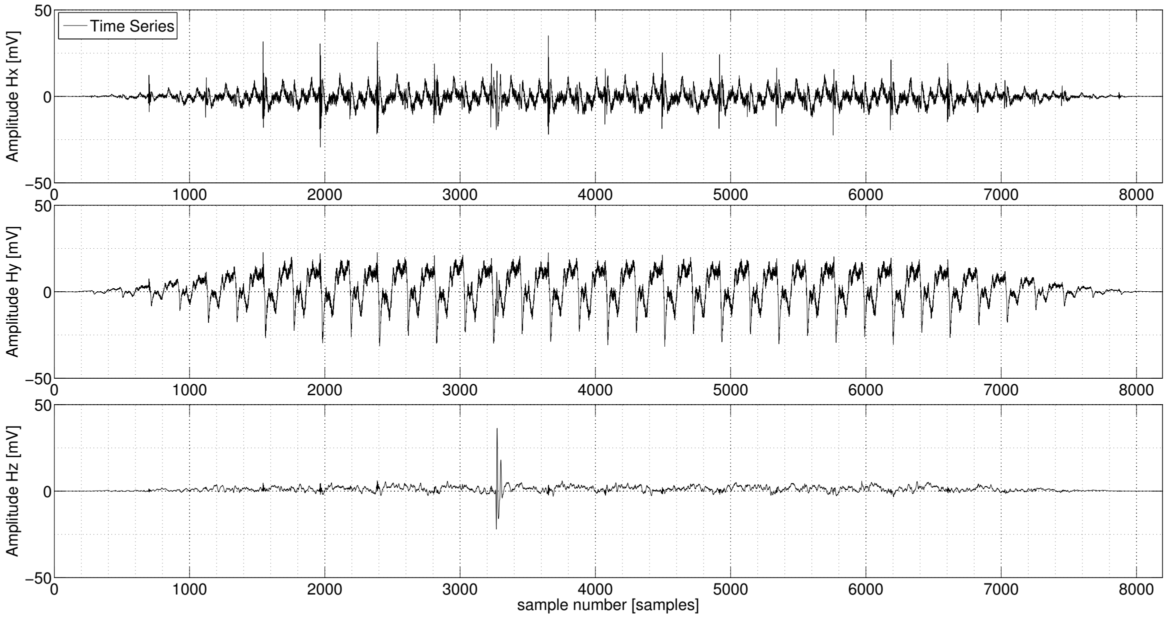

Figure 7: Times series section of ∼8k samples (1/8 s) of the three magnetic field components. A cosine taper is applied decreasing the flanks of the time series to zero. Noise is visible in all three time series of the magnetic field components. In the horizontal components over the whole section, whereas one distinct spike is visible in the vertical component. Additionally, the recorded amplitudes are bigger in the horizontal components.

After tapering, the next step is to apply a Fourier transformation to the shortened time series. To visualize the VLF transmitters, the power spectra of the time series are determined. In this processing step, the VLF transmitters become visible in the power spectra (cf. Figure 8). It is important to note that the signal of the VLF transmitters are no Dirac delta functions of their frequency in the spectra, but blurred Dirac delta functions around the VLF transmitter frequency. This becomes clearer in Figure 10 of the following section and the consequences are discussed in Section 4.4.

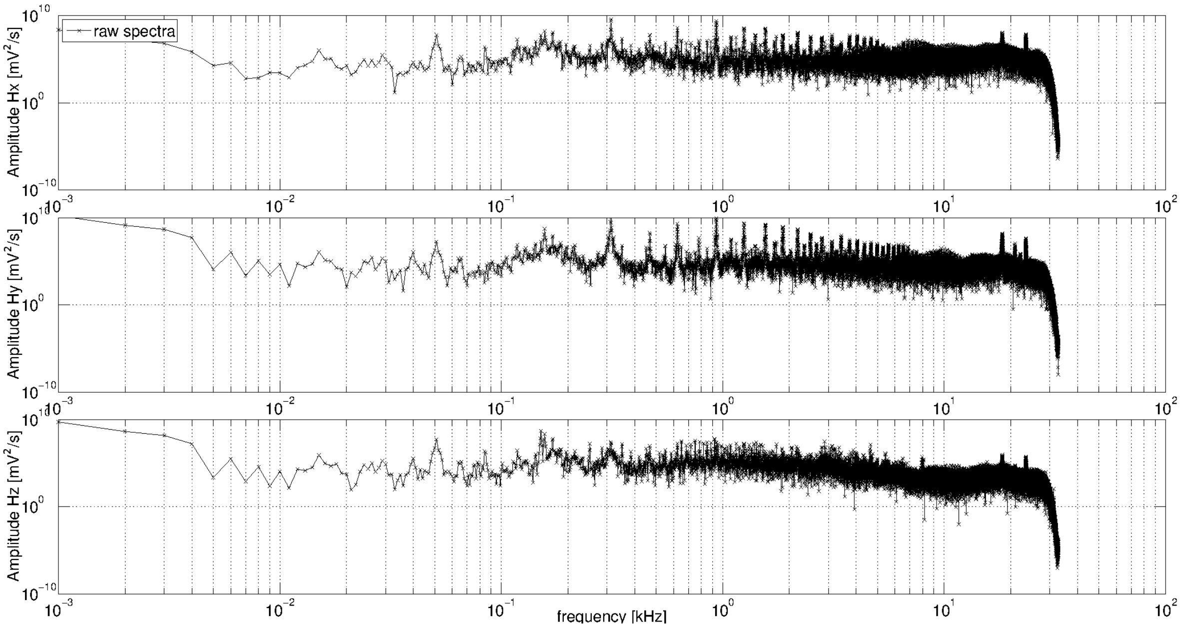

Figure 8: Full spectra of the three magnetic field components. The 18.3 kHz and 23.4 kHz transmitters, for example, are visible in all three spectra.

4.3 Identification of Transmitters

During the work with the measured VLF data, it turned out that it is important to know whether a transmitter is available at a certain profile location or not in order to be able to calculate the transfer functions correctly. Therefore, the process of identifying transmitters is automated. This process contains two steps. First, a moving median is applied to each power spectrum (dashed green line in Figure 9) and the difference of each frequency point of the spectrum to the median is determined. The amplitude difference is detemined in decibel (dB), that is $20 \cdot \log_{10}(y)$. The empirical value to identify potentially usable transmitters from UAS-VLF data, is found to be at amplitudes of 30 dB to 34 dB above the median (red dots in Figure 9). Trying to use transmitters below this dB levels leads to unfeasible transfer functions. This is in agreement with typical magnetic signal to noise ratios of 30 dB described in Bastani and

Pedersen [2001]. VLF radio transmitters communicate at frequencies in the range of 15 kHz to 30 kHz (cf. Section 2.2.1).

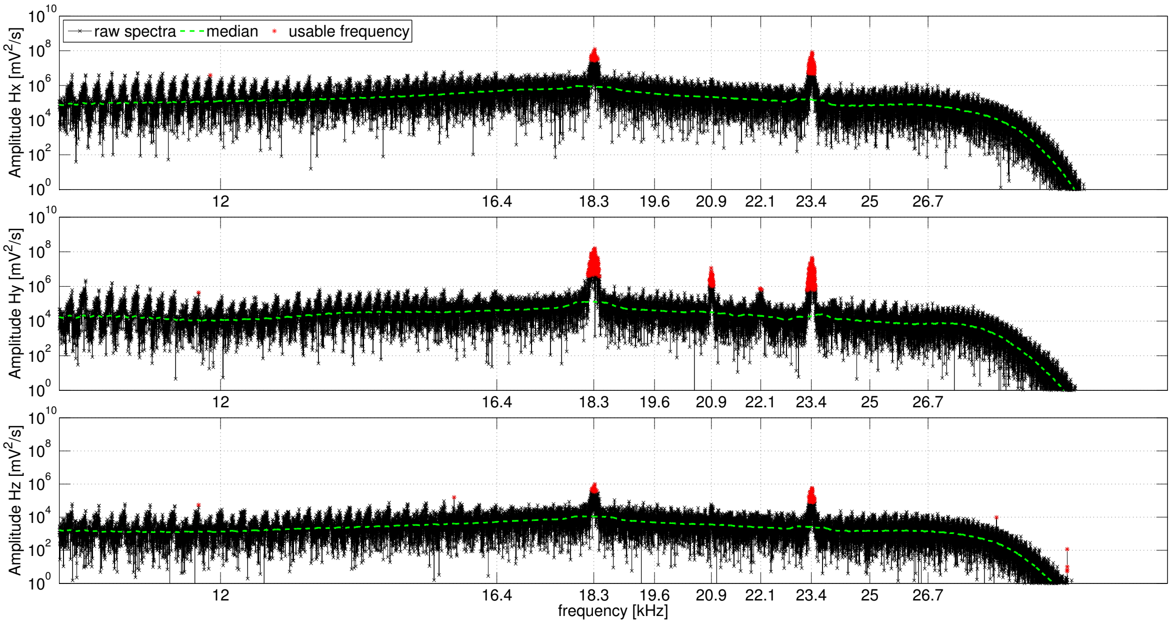

Figure 9: Spectra of the three magnetic field components. Potentially usable frequencies are marked red (difference to median greater than 30 dB). The 18.3 kHz and 23.4 kHz transmitters are clearly visible with the naked eye, additionally visualized through the red points. The 20.9 kHz frequency is resolved singly in the H_y component of the magnetic field.

Second, the total number of consecutive red points is counted. Due to noise features, individual frequencies exceed the defined dB levels, despite no transmitter exists for these frequencies, in other cases the transmitter signal barely exceeds the noise level. These as potentially available marked transmitter frequencies are not feasible to determine the Tipper. A transmitter counts as resolved if more than 10 frequencies (i. e. red points) exceed the 30 dB margin. Figure 10 shows a zoom of Figures 8 and 9 to emphasize the second step of the automated detection of transmitters. Red points outline potentially available transmitters. In addition to the number of red dots, the distance of the points to each other in a frequency interval is determined. A transmitter is finally defined as resolved if 10 or more points of potentially available transmitters are located within a 40 Hz section (equalling 40 points).

If both criteria are fulfilled, the respective frequency is marked in the spectra as an averaged transmitter in purple (matching the original VLF frequency of the transmitter). The expression "averaged" is used because the average frequency of all red dots equals the transmitting frequency of the respective transmitter. In Figure 10, the criteria of more than 10 red points located inside a 40 Hz interval for the potentially available 22.1 kHz transmitter is not met

(H_y component). The interval contains some (red) points of the possibly usable frequency category, but the transmitter is not counted as resolved and, therefore, not marked purple.

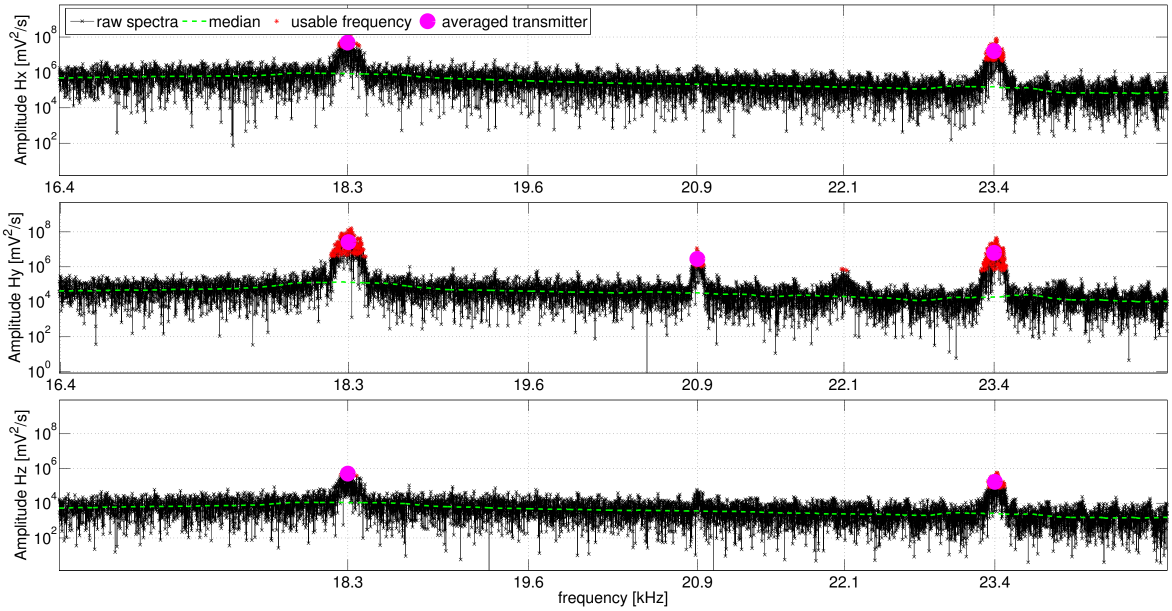

Figure 10: Spectra of the three magnetic field components. Potentially usable frequencies are marked red (difference to median greater than 30 dB). The 18.3 kHz and 23.4 kHz transmitters are clearly visible and additionally visualized through the red points. Transmitters that count as resolved are marked in purple. An example for a potential transmitter (red dots) that does not meet the requirements of the second transmitter detection step is visible in the H_y component of the spectra at 22.1 kHz.

Within an actual UAS-VLF field campaign, hundreds of spectra are generated. Thus, a display method to give a comprehensive overview of the available transmitters over the whole profile is developed. For this, a plot is produced with frequencies on the y-axis and profile location on the x-axis (cf. Figure 11). In this plot, a transmitter only marked if is identified by the method explained above. In the H_z component resolved transmitters are plotted as big red dots exactly at the VLF frequency. For a better overview, the H_x and H_y components are plotted slightly above and below the frequency axis, respectively. This way it is possible to recognize usable transmitters for a given profile at one glance, checking if the H_z component is available and additionally taking into account the horizontal components H_x and H_y. In Figure 11, the 23.4 kHz frequency shows a very stable behaviour. All three magnetic components are continuously received over the whole profile, with the exception of one point in the H_z component at profile meter 103. This indicates that 23.4 kHz is very suitable for calculating the transfer functions.

In comparison, the 18.3 kHz frequency shows numerous gaps. Though the H_z component is detected throughout the entire profile, the H_x and H_y components are not. However, the H_y component is resolved throughout the profile. Therefore, the 18.3 kHz frequency is used to calculate the Tipper, but the result may be disturbed or erroneous due to transmitter signal quality. In contrast, the H_x component of the 20.9 kHz frequency is not resolved at all and barely resolved in the H_z component. Nevertheless, the H_y component is resolved well over the whole profile. Determining transfer functions with the 20.9 kHz transmitter frequency will most probably produce results difficult to interpret. The obtained transfer functions will have numerous discontinuities as the signal to noise level is too low in the H_x and – more important – the H_z component.

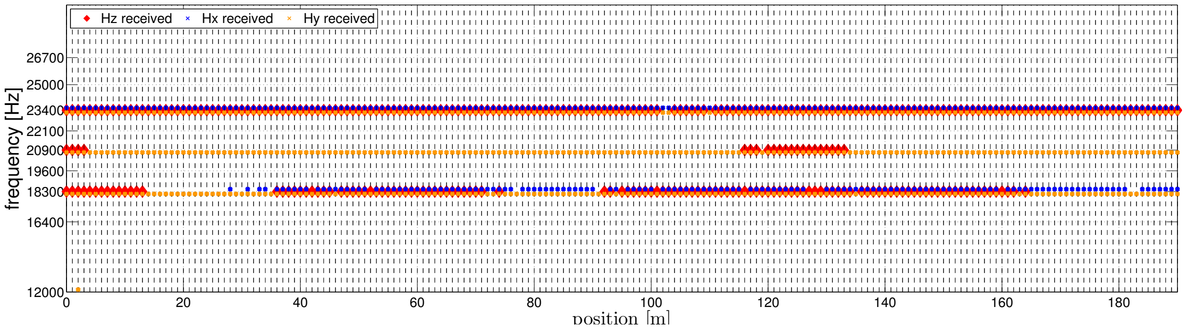

Figure 11: On the y-axis frequencies of common VLF transmitters are denoted. The x-axis shows the location along the profile. Resolved transmitters receive colour marks. Red dots mark H_z, blue dots H_x, and yellow dots H_y component of the magnetic field. The 23.4 kHz frequency is resolved over the whole profile in all three magnetic field components and thus definitely suitable for further processing.

The most time consuming processing part – in terms of computational time – is to calculate the spectra and to apply the moving median to the spectra. Thus, to be able to work with the spectra and develop analysis methods for such a big data set, preliminary results are stored. This way, it is possible to determine the transfer functions quickly with different approaches. The drawback is the large amount of storage space required. In addition to the measured data, the processed data for a profile of 200 m length need $\sim$ 900 MB of space. This is important to note as one of the challenges of UAS-VLF measurements is the appropriate handling of large amounts of data.

4.4 Determination of the Transfer Functions

After the received transmitters are determined, the next processing step is to calculate the transfer functions. Depending on the number of available transmitters, the Tipper is calculated with the scalar or bivariate approach (Section 2.2.2). In order to compare different processing approaches and estimate their influence on the determined transfer functions, the following figures show the transfer functions of an exemplary UAS-VLF profile (Section 6.1.3) for the different calculation steps and methods.

The data is recorded continuously over 191 s, covering a profile length of 191 m. To calculate the transfer functions, the time series is cut into 1 s sections, corresponding to 191 data points. The profile crosses two anomalies approximately at profile meters 55 and 145. The emphasis of this section lies on the quality of the shape of the transfer functions (i. e. the less discontinuities – thus the smoother the course of the Tipper is – the better is its quality) and how distinct anomalies are in the transfer functions. The available transmitters for this measurement are summarized in Figure 11.

Scalar with one Frequency

The most basic way to calculate the Tipper is to simply divide the vertical magnetic component by the horizontal component for every profile location, that is $H_z(\omega) = A(\omega) \cdot H_x(\omega)$ and $H_z(\omega) = B(\omega) \cdot H_y(\omega)$, where H_i are the magnetic field components, (A, B) is the Tipper vector and ω is a transmitter frequency (scalar method in Section (2.2.2)). For this example, the used frequency ω is 23.4 kHz. The result is shown in Figure 12. The transfer functions show many small and a few big discontinuities. The presented profile crosses two major anomalies, visible as a zero crossing in both the real and the imaginary parts of the transfer functions. The first anomaly is located at approximately 55 m and the second anomaly at approximately 145 m. Since this section focuses on the quality of the transfer functions and does not focus on the subsurface information, the interpretation of the data will be given in Chapter 6.

Scalar with Stacked Spectra

One possible way to refine the processing is to calculate the Tipper out of stacked spectra. For this, each time series of 1 s (65,536 samples) is divided for example by four, leading to four sections of 0.25 s time series (16384 samples each). Each of these sections is Fourier transformed and subsequently stacked. Afterwards, the transfer functions are calculated from the resulting spectra (cf. Figure 13). However, the effect of stacking the spectra does not notably improve the quality, that is smoothness, of the transfer functions. In comparison to the unstacked Tipper, the stacked Tipper still shows lots of discontinuities. Calculating the Tipper from spectra of 1 s on the one hand and from stacked spectra calculated out of four time series of 0.25 s length on the other hand shows no distinct difference with the exception of a few outliers. Thus, some parts are smoother, but others show more or stronger discontinuities.

This method of refining the Tipper is tested in various combinations. From changing the number of stacks of the spectra (2, 4, 8, and 16), over trying to stack the time series itself, or both in combination (time series and spectra), or to increasing the length of the initially used time series of one s to two or more. The result is always similar to the here presented result. The quality, of the transfer functions is not increased significantly.

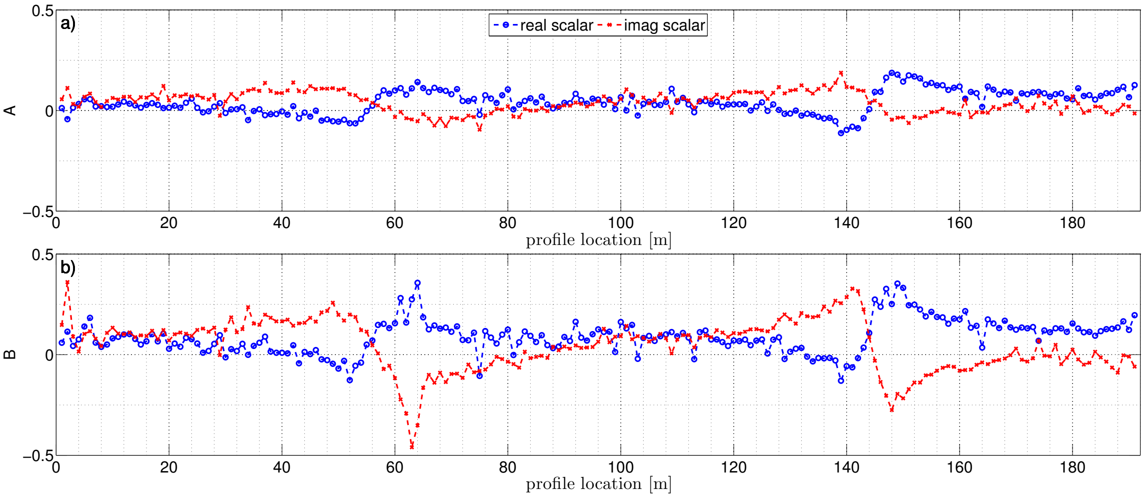

Figure 12: Magnetic transfer functions displayed against profile location. Top panel Tipper component A, bottom panel Tipper component B. Blue is the real part and red the imaginary part of the Tipper. The transfer functions are calculated with the scalar method for the 23.4 kHz frequency.

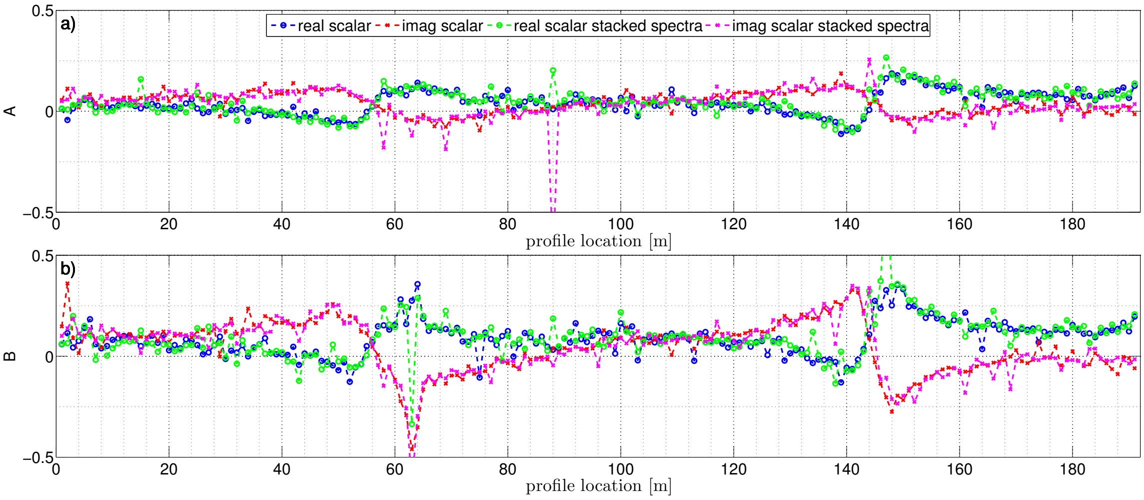

Figure 13: Magnetic transfer functions displayed against profile location. Top panel Tipper component A, bottom panel Tipper component B. Blue/green is the real part and red/purple the imaginary part of the Tipper. The transfer functions are calculated with the scalar method at 23.4 kHz.

Scalar over a Frequency Band

Since the presented stacking methods do not lead to a significant improvement of the transfer functions, in the present thesis another stacking approach is used. The following stacking method to calculate the Tipper is based on the effect of spectral leakage [Harris, 1978]. For a time series of infinite length and frequency ω, a Fourier transformation leads to a signal in the power spectrum with a delta peak at ω. However, time series of measured data have a finite length. A Fourier transformation of such a time series does not lead to a spectrum with a delta peak. Rather, the signal extends to neighbouring frequencies. The reason is that the measured data is multiplied by a rectangular window function, resulting in a convolution in the frequency domain of the sinus VLF transmitter signal with the rectangular window. The effect of spectral leakage is commonly decreased by applying other window functions or so called taper.

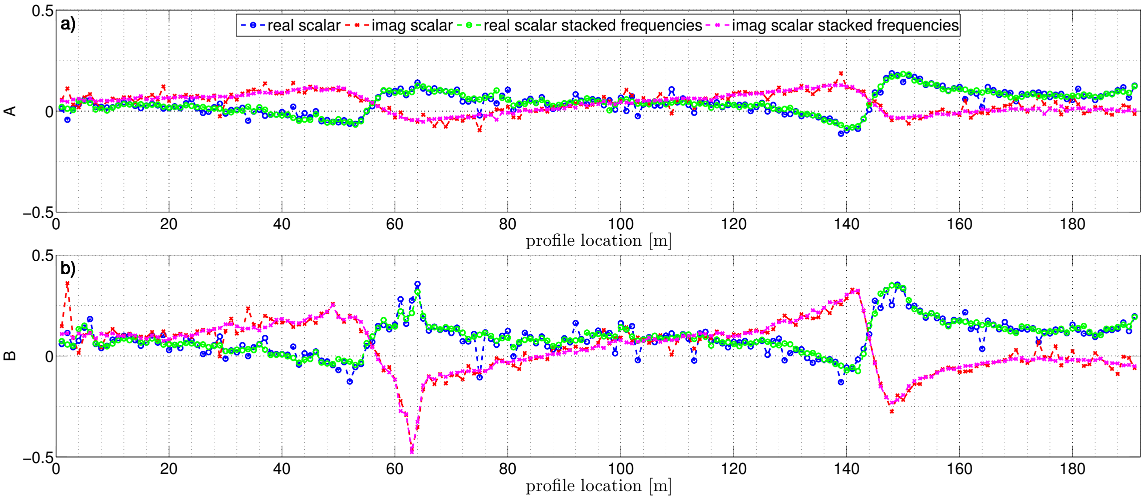

Figure 14: Magnetic transfer functions displayed against profile location. Top panel Tipper component A, bottom panel Tipper component B. Blue/green is the real part and red/purple the imaginary part of the Tipper. The transfer functions are calculated with the scalar method at 23.4 kHz. The comparison between calculating the Tipper out of one frequency solely and the one stacked over a frequency range.

Following Parseval's theorem, the energy of a signal in the time domain equals its energy in the frequency domain. Therefore, the information of the signal is not limited to the exact transmitter frequency, but is also partly allocated in the neighbouring frequencies, too. The Tipper is calculated separately in an interval for each frequency and the transfer functions are averaged afterwards. The method is illustrated for the A component of the scalar method in equation (70) and (71),

$$A_i = \frac{H_z(\omega_i)}{H_x(\omega_i)} \qquad \text{, with } i = -N, ..., N \tag{70}$$

$$A = \frac{1}{N} \sum_{i=-N}^{N} A_i \tag{71}$$

with Tipper component A, frequency ω_i and the interval around the original frequency of the transmitter defined by N. Based on experience, a good value for N is 40. Smaller N leads to a rapid decrease in smoothness of the transfer functions. Larger N has less influence on the transfer functions and the quality begins to decrease after a certain N_{max}.

The resulting transfer functions of such a stacking are displayed in Figure 14. A considerable increase in the quality of the derived Tipper is achieved. The transfer functions are clearly smoother compared to the previous ones.

Scalar with Different Transmitter Frequencies

Another option to improve the quality of the transfer functions is to determine the transfer functions with other available frequencies. In Figure 15, the transfer functions of the 23.4 kHz frequency are compared to the 18.3 kHz frequency and the 20.9 kHz frequency. For the availability of transmitter frequencies in this example see Figure 11.

Compared to the Tipper of the 23.4 kHz frequency, the Tipper of the 18.3 kHz frequency shows two distinct differences. The amplitudes around the measured anomalies vary and the transfer functions are shifted. A change in the smoothness of the Tipper is not noticeable.

In contrast, the Tipper of the 20.9 kHz frequency shows a remarkable decrease of smoothness compared to the 23.4 kHz frequency, especially in the A component of the Tipper. This decrease in quality is no surprise considering the bad resolution of the 20.9 kHz transmitter frequency – especially in the H_y component (cf. Figure 11). In the B component of the Tipper, the first anomaly is not identifiable in the real part (green). Nevertheless, in general, as for the 18.3 kHz frequency, the amplitudes of the transfer functions around the anomalies and the course of the transfer functions at the locations without anomalies are different compared to the 23.4 kHz frequency.

A possible reason for the shifts of the transfer functions in y-direction – especially of the real part – is given in Section 5.2, where the influence of sensor rotations is examined.

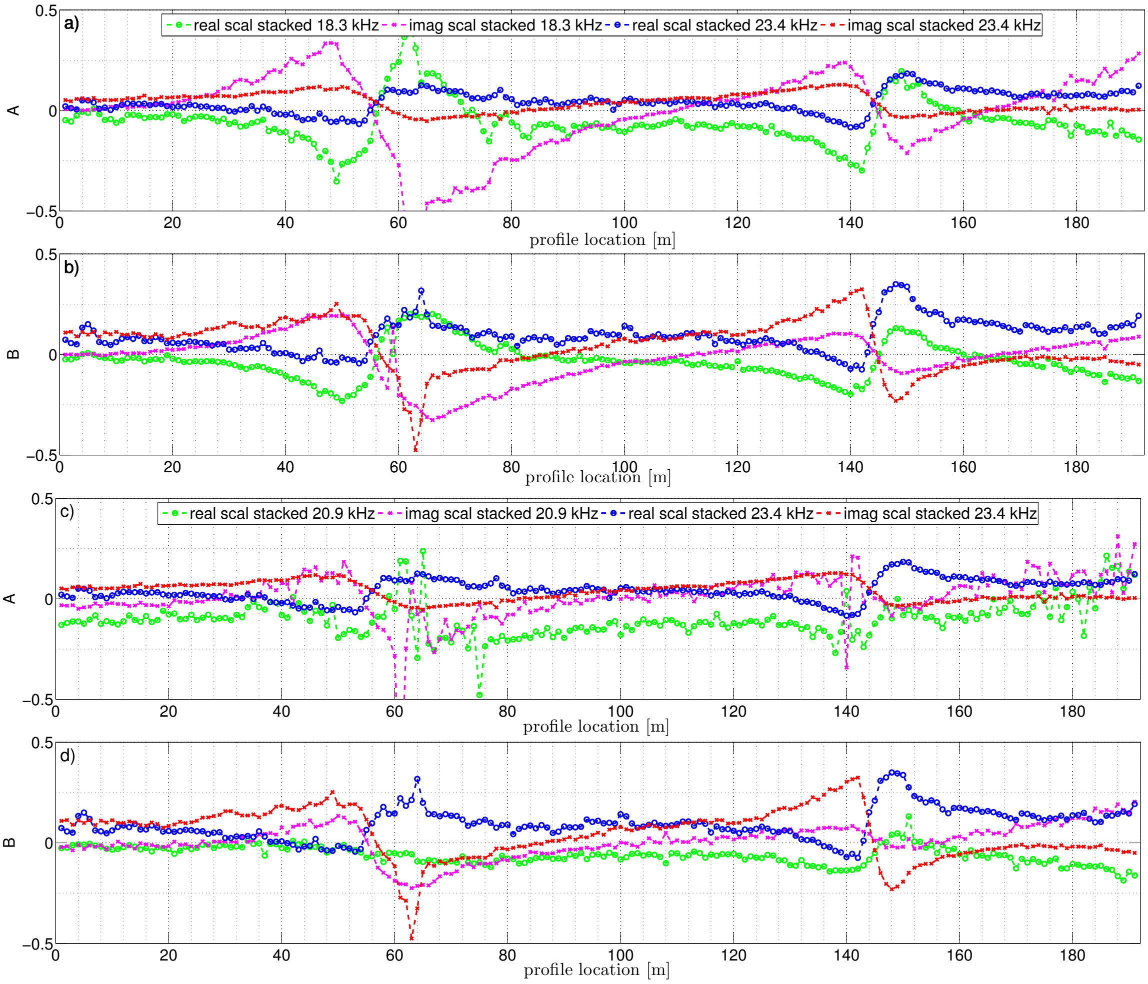

Figure 15: Amplitude of magnetic transfer function (Tipper) against profile location. Blue/green is the real part and red/purple the imaginary part of the Tipper. Scalar approach, stacked over frequency range. a) and b) comparison of the transfer functions calculated with the 23.4 kHz and 18.3 kHz frequency. c) and d) comparison of the transfer functions calculated with the 23.4 kHz and 20.9 kHz frequency.

Bivariate with one Frequency

In order to further increase the quality of the transfer functions, the approach of Pedersen et al. [1994] is applied. With this bivariate approach, the Tipper is determined out of all available transmitters at once. This approach determines the transfer functions using the least squares method (cf. Section 2.2.2).

The first and basic approach – as for the scalar method – is to calculate the Tipper for two transmitters using solely the exact transmitter frequencies. Figure 16 shows the derived transfer functions using the 18.3 kHz and 23.4 kHz frequencies. As a result, even if the Tipper is considerably rough, in the majority the anomalies are clearly visible.

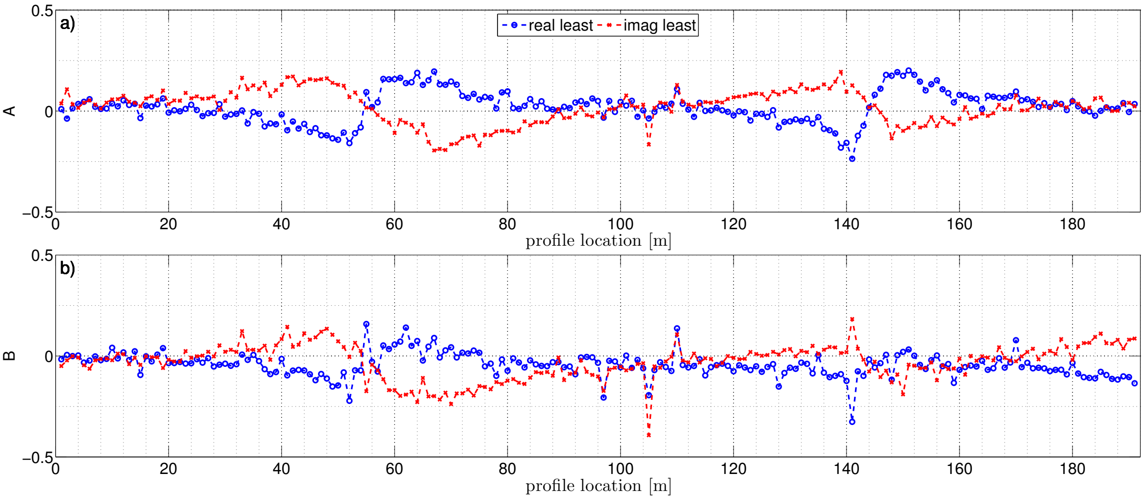

Figure 16: Magnetic transfer functions displayed against profile location. Top panel Tipper component A, bottom panel Tipper component B. Real part (blue) and imaginary part (red) of the Tipper. The transfer functions are calculated with the least squares method using the 18.3 kHz and 23.4 kHz frequencies.

The comparison of the scalar to the least squares approach – both not stacked over a frequency range – is show in Figure 17. It is noticeable that the transfer functions determined with the bivariate approach are not smoother than with the scalar approach. This result may surprise. Since the information of two transmitters is used, transfer functions of higher quality could be expected. The reason why the quality does not increase is that only the two exact transmitter frequencies are used. The method that is used to determine the smooth transfer functions in Figure 14 uses 40 frequencies. If with the same method two frequencies are used the resulting transfer function would not be smooth either. Thus, the result that the transfer functions do not become smoother using two frequencies (each of a different transmitter), is consistent.

Another effect is that the shift of the Tipper along the y-axis is smaller compared to the scalar approach. This is important to note. The shift of the Tipper is investigated in Section 4.7 in more detail. Furthermore, the first anomaly is clearly detected in A (larger amplitudes of the real part), whereas the second anomaly is practically not detected in B.

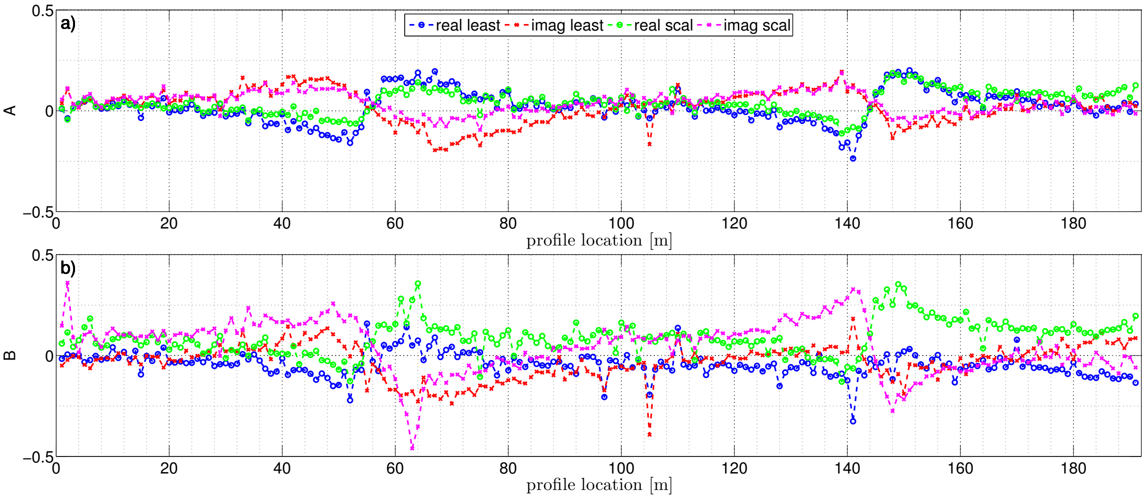

Figure 17: Magnetic transfer functions displayed against profile location. Top panel Tipper component A, bottom panel Tipper component B. Blue/green is the real part and red/purple the imaginary part of the Tipper. The transfer functions are calculated with the scalar method for 23.4 kHz and the least squares method using the 18.3 kHz and 23.4 kHz frequencies.

Bivariate over a Frequency Band

If the Tipper is calculated over frequency intervals and subsequently stacked (as for the scalar approach but now for two different transmitters that is two different frequency ranges), it is distinctly smoother. The comparison to the unstacked Tipper is shown in Figure 18. This major improvement of the Tipper determined over frequency ranges is in the same order as the improvement is in the scalar analysis (cf. Figure 14).

The comparison of the scalar with the least squares approach – both stacked over a frequency range – is shown in Figure 19. For the A part of the Tipper, the major difference is that the amplitudes of the first anomaly are larger for the least squares method – emphasizing it slightly. The course of the remaining parts of the transfer functions is almost similar. The B part shows more differences. The Tipper is moved towards zero on the y-axis, reducing the shift of the Tipper derived with the scalar method. Additionally, the transfer functions of the least squares method are smoother, but the amplitudes of the transfer functions of the second anomaly are smaller.

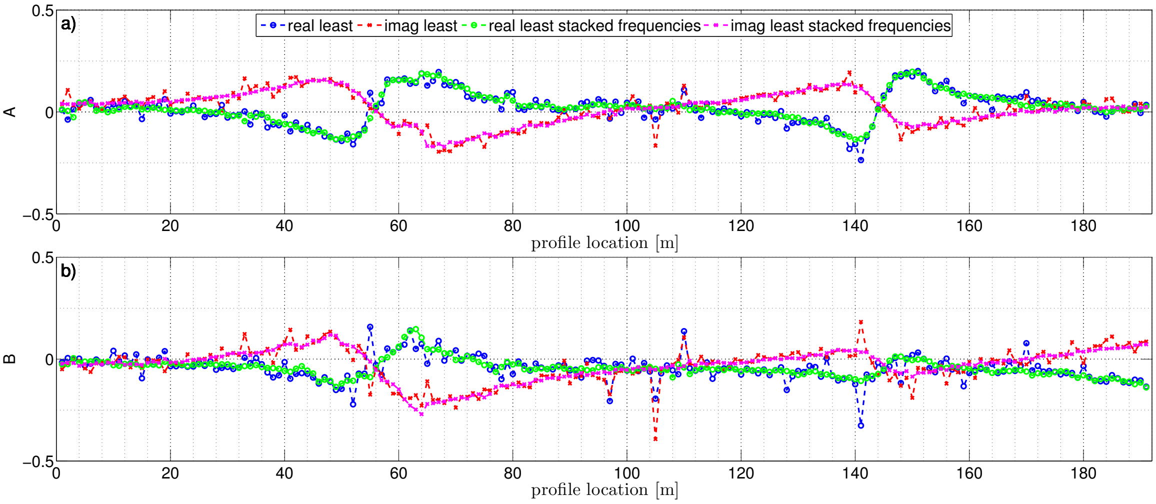

Figure 18: Magnetic transfer functions displayed against profile location. Top panel Tipper component A, bottom panel Tipper component B. Blue/green is the real part and red/purple the imaginary part of the Tipper. The transfer functions are calculated with the least squares method using the 18.3 kHz and 23.4 kHz frequencies. The comparison between calculating the Tipper out of one frequency per transmitter solely and the one of stacked over a frequency range.

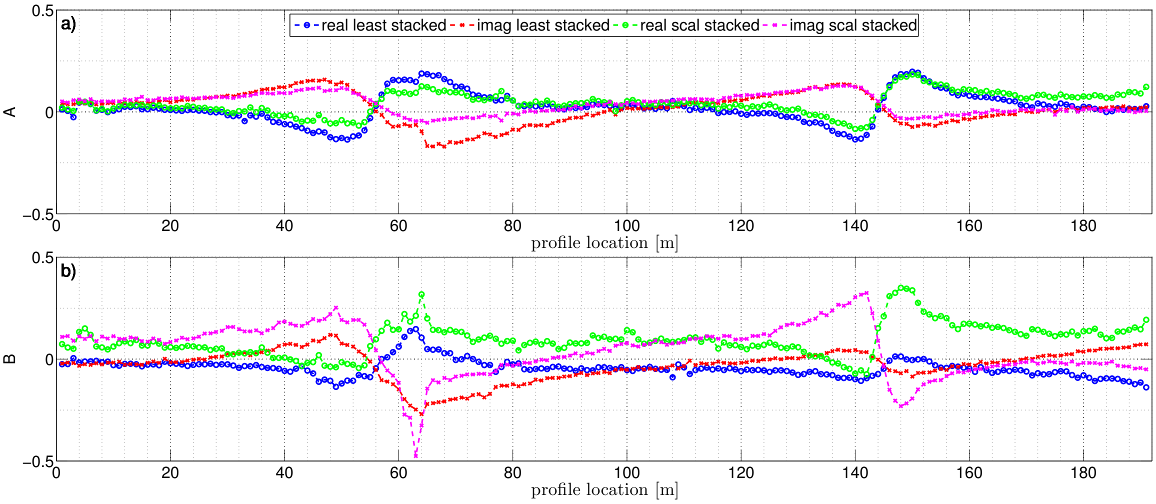

Figure 19: Magnetic transfer functions displayed against profile location. Top panel Tipper component A, bottom panel Tipper component B. Blue/green is the real part and red/purple the imaginary part of the Tipper. The transfer functions are calculated with the scalar method for 23.4 kHz and the least squares method using the 18.3 kHz and 23.4 kHz frequencies – both stacked over a frequency range.

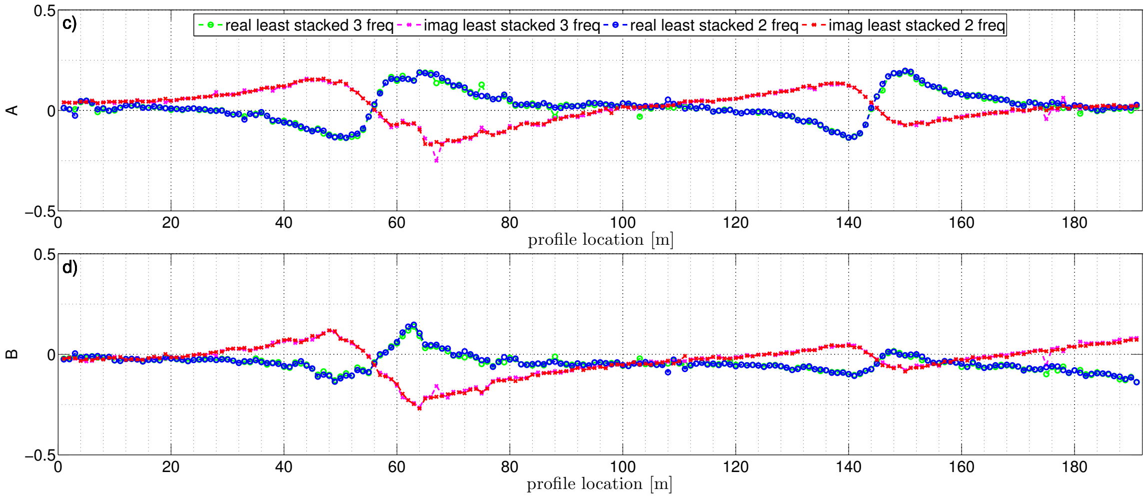

Figure 20: Magnetic transfer functions displayed against profile location. Top panel Tipper component A, bottom panel Tipper component B. Blue/green is the real part and red/purple the imaginary part of the Tipper. The transfer functions are calculated with the least squares method once using the 18.3 kHz, 20.9 kHz and 23.4 kHz frequencies and once only the 18.3 kHz and 23.4 kHz frequencies.

The final step is to include as many frequencies in the least squares method as possible. An overview of the available frequencies of the presented profile is shown in Figure 11. In Figure 20, the transfer functions derived using the 18.3 kHz, 20.9 kHz, and 23.4 kHz frequencies are shown. In comparison to each other, the transfer functions using only two frequencies are smoother. Thus, a quality improvement using three frequencies is not achieved. Nevertheless, in both cases (two and three used transmitters), the transfer functions calculated with the least squares approach are much more stable in amplitude and course in comparison to the scalar approach (cf. Figure 15 and 20).

The reason that a Tipper calculated from two frequencies shows a higher quality than from three frequencies is the different quality of the used transmitters. Figure 11 shows that the 20.9 kHz transmitter frequency is not well resolved for most profile locations and Figures 15 c) and d) show that the quality of the transfer functions derived from the 20.9 kHz frequency is much worse the the one of the 18.3 kHz and 23.4 kHz frequencies. Still, it is remarkable that, although the 20.9 kHz frequency has a negative influence in terms of smoothness of the transfer function, the transfer functions remain considerably stable.

In summary, independent of the approach (scalar/bivariate), the method found to be most convenient to compute the Tipper is to integrate over a frequency band around the used VLF transmitter frequency. This method leads to the most stable and smooth results. In comparison, stacking the time series and or spectra and subsequently calculating the Tipper of the exact but solely used VLF transmitter frequency, has no remarkable positive effect on the transfer functions. Furthermore, in terms of smoothness, the bivariate approach does not lead to improved results. However, both amplitude and course of the transfer functions seem to be more stable in the bivariate approach than in the scalar one.

4.5 Validation of the Processing

In this section, the results of the final processing step of Section 4.4 are compared with the robust processing approach of Becken [2013], which is based on Egbert and Booker [1986]. In Figure 21, the Tipper results of the least squares method are compared to Becken [2013]. The compared Tipper is a time section of a UAS-VLF measurement. The transfer functions generally show a good agreement. As a quantitative measure of difference of the results, the RMS (cf. Section 2.4.6) compared to the Tipper result of Becken [2013] of each transfer function is specified. The RMS in the real parts of the Tipper are higher than the imaginary one in both components A and B.

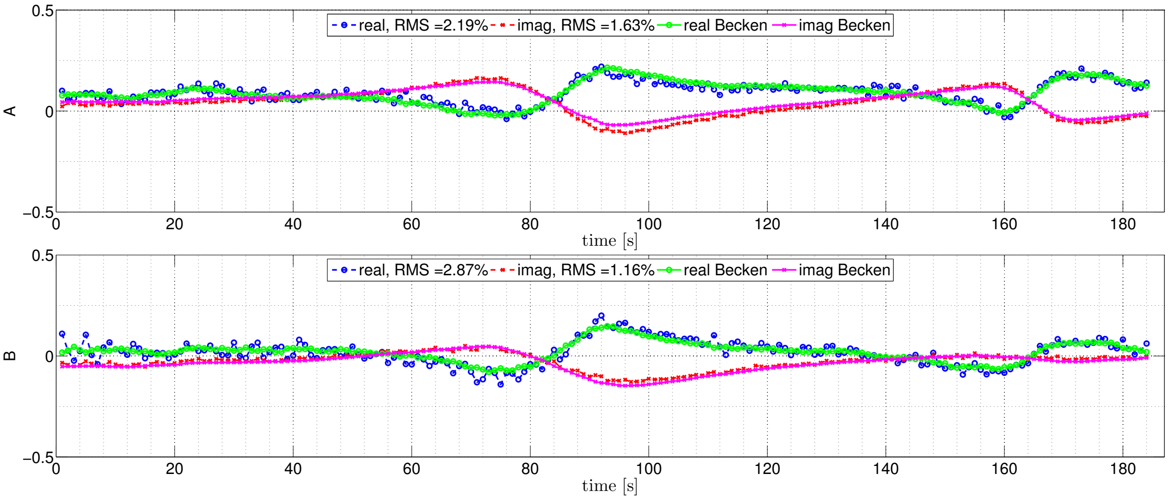

Figure 21: Magnetic transfer functions displayed against time. Top panel Tipper component A, bottom panel Tipper component B. Blue/green is the real part and red/purple the imaginary part of the Tipper. In green and purple results of the processing of Becken [2013]. The transfer functions in blue and red are calculated with the least squares method using the 18.3 kHz and 23.4 kHz frequencies.

The reason for the higher RMS, especially in the real parts of the Tipper, could be oscillations of the transfer functions which continue over the whole time section. These oscillations are possibly caused by sensor rotations during flight. In Figure 22, a moving median filter is applied to the results of Figure 21. As a result, the RMS decreases considerably for all transfer functions except the imaginary part of A, where it remains approximately constant. This shows that an applied filter can reduce such distortions if the transfer functions contain discontinuities or oscillations.

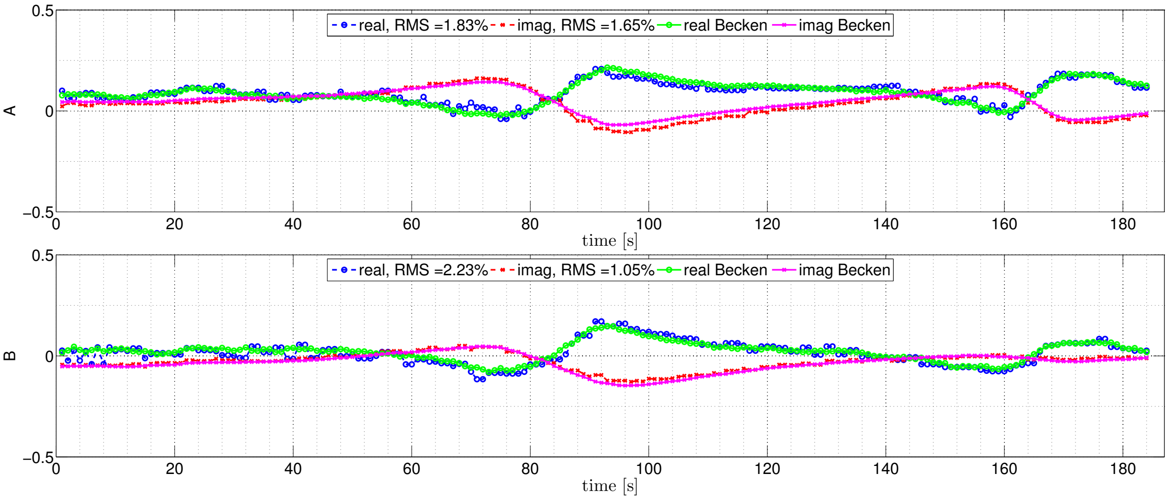

Figure 22: Magnetic transfer functions displayed against time. Top panel Tipper component A, bottom panel Tipper component B. Blue/green is the real part and red/purple the imaginary part of the Tipper. In green and purple results of the processing of Becken [2013]. The transfer functions in blue and red are calculated with the least squares method using the 18.3 kHz and 23.4 kHz frequencies and a moving median filter is applied.

The next plot (cf. Figure 23) examines the resulting transfer functions when three frequencies are used instead of two. The additionally used 20.9 kHz frequency transmitter is not as constant (in the sense of available transmitters, compare for example Figure 11) as the other two transmitters. The result is a small decrease in RMS for the real parts and a small increase in RMS in the imaginary parts. This provides evidence to two things: Firstly, calculating the transfer functions by using available but not ideal frequencies does not have a large impact on the quality of the transfer functions. The impact of a filter is larger, at least if the transfer functions show an oscillating behaviour. Secondly, a third frequency – if not of good quality – can even worsen the result, as seen in the imaginary part. Both conclusions are drawn compared to the processing result of Becken [2013].

These RMS trends are confirmed by applying a moving median filter on the three frequency results (cf. Figure 24). An overview of each single and the total RMS values is given in Table 3. It is noticeable that the total RMS, which is calculated out of all transfer functions, shows a minimal decrease if a median filter is applied. However the absolute RMS value remains approximately constant and does not depend on the amount of applied frequencies.

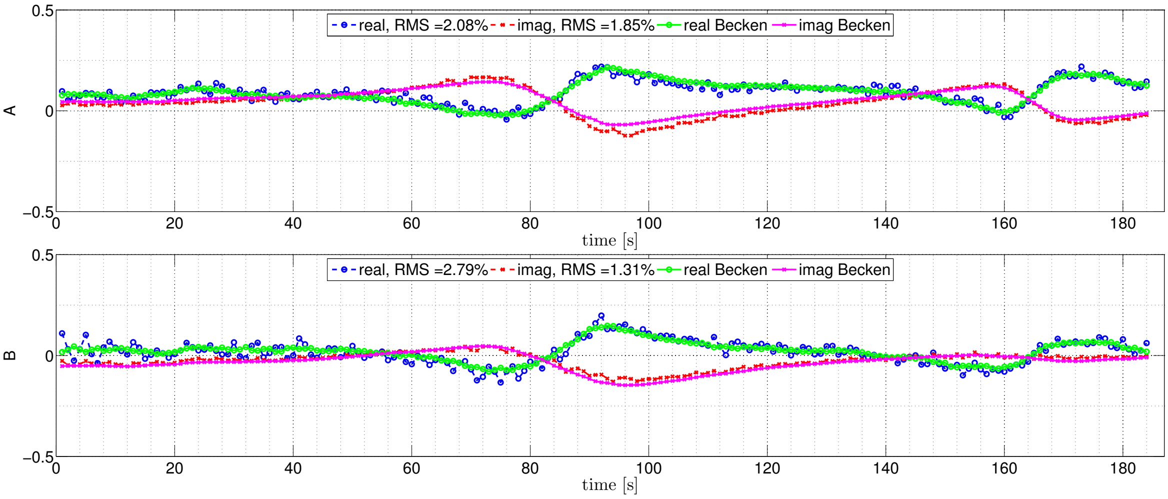

Figure 23: Magnetic transfer functions displayed against time. Top panel Tipper component A, bottom panel Tipper component B. Blue/green is the real part and red/purple the imaginary part of the Tipper. In green and purple results of the processing of Becken [2013]. The transfer functions in blue and red are calculated with the least squares method using the 18.3 kHz, 20.9 kHz and 23.4 kHz frequencies.

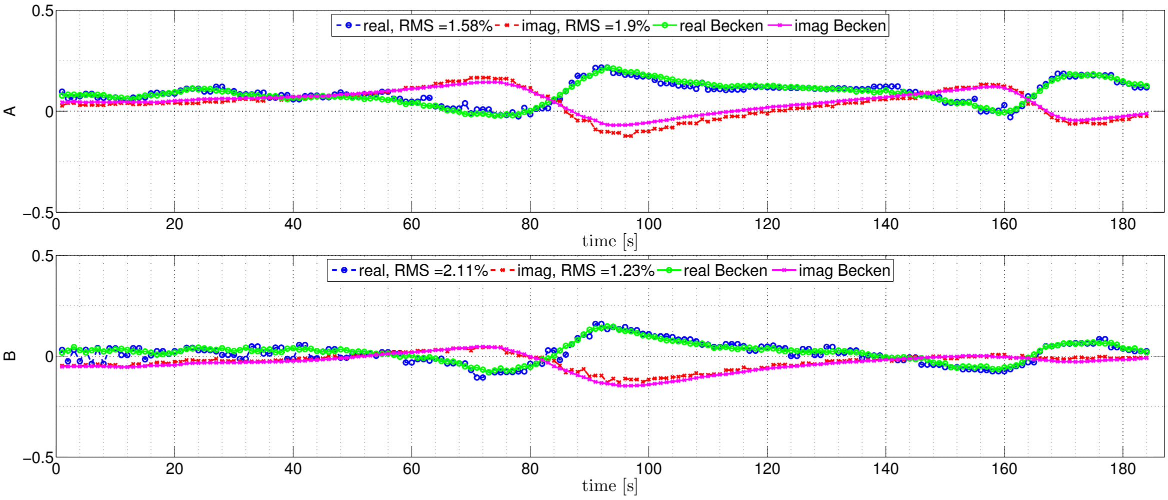

Figure 24: Magnetic transfer functions displayed against time. Top panel Tipper component A, bottom panel Tipper component B. Blue/green is the real part and red/purple the imaginary part of the Tipper. In green and purple results of the processing of Becken [2013]. The transfer functions in blue and red are calculated with the least squares method using the 18.3 kHz, 20.9 kHz and 23.4 kHz frequencies. The comparison between the differently calculated Tipper shows a good accordance.

Table 3: RMS values of different transfer functions determined with the algorithm developed in the present thesis compared to transfer functions determined by Becken [2013].

	two freq.	two freq. median	three freq.	three freq. median
real A	2.19	1.83	2.08	1.58
imag A	1.63	1.65	1.85	1.90
real B	2.87	2.23	2.79	2.11
imag A	1.16	1.05	1.31	1.21
total	2.06	1.74	2.08	1.73

To conclude the validation, the two independently developed processing algorithms – the one of Becken [2013] and the one presented in the present thesis – agree well in terms of RMS. Nevertheless, considering the smoothness of the calculated transfer functions as a quality criterion, the processing steps developed in the present thesis could be further improved. Especially the applied filter approach promise smoother results since this is the main differences to Becken's approach.

4.6 Rotation of the Transfer Functions

The VLF results shown in Chapter 6 are based on a 2D algorithm. As explained in Section 2.2.1, one part of the Tipper is zero in the ideal 2D case. If the profile is not orthogonal to the strike of an anomaly, both parts of the Tipper contain information, that is both components are unequal zero. In order to exploit all gathered information for the 2D modelling, it is necessary to rotate the transfer functions. After rotating the Tipper, the information of an anomaly is reduced mainly to one Tipper component and completely if it is a 100 % 2D anomaly – which in the field is hardly true. If exact strike and profile direction are known, the Tipper can simply be rotated by the angle ϕ. In this case, ϕ is the angle between strike direction and the semi-parallel axis of the measuring coordinate system. The angle is zero if strike and one axis of the coordinate system are exact parallel. The rotated transfer functions are then given by equation (72) [Gharibi and Pedersen, 1999].

$$\begin{pmatrix} A \\ B \end{pmatrix} = \begin{pmatrix} \cos\phi & \sin\phi \\ -\sin\phi & \cos\phi \end{pmatrix} \begin{pmatrix} A' \\ B' \end{pmatrix} \tag{72}$$

A' and B' are the unrotated Tipper. However, if the exact strike direction of the anomaly is not known or if several anomalies with different strike directions cross a given profile, it is possible to calculate a rotation angle by minimizing the Tipper component corresponding to the parallel strike direction. For the measurements presented in the present thesis, the H_x component of the magnetic field is parallel to the profile direction, that is the B component of the Tipper is minimized over the profile:

$$B_{min} = min(-A'\sin\phi_i + B'\cos\phi_i) \qquad \phi_i = 0, 1, 2, ..., 360 \tag{73}$$

An example is given in Figure 25. The transfer functions are rotated by 40 °. The amplitude of the A component of the Tipper is increased at the first anomaly and stable around the second anomaly. Additionally, the transfer functions neighbouring the first anomaly (profile meters 0 – 30 and 80 – 120) are shifted (in comparison to the unshifted) towards the zero axis, whereas for profile meters 170 to 190, the transfer functions are shifted away from the zero axis. The B component of the Tipper is minimized. That is the amplitude of the real and the imaginary part of the Tipper is decreased for B. Minimizing B in this way does not take possible different strike directions into account if more than one anomaly is detected. The anomaly with the larger amplitudes in the B part of the Tipper has (since B is minimized) a greater impact on the angle than the other anomaly with smaller amplitudes.

However, the Tipper does not become zero between profile meters 55 to 143. Thus, it would not be reasonable to calculate the rotation angels separately, because of the superposition of neighbouring anomalies. Nevertheless, a possible way to improve the processing of UAS-VLF for 2D anomalies is to find a way to circumvent this weakness.

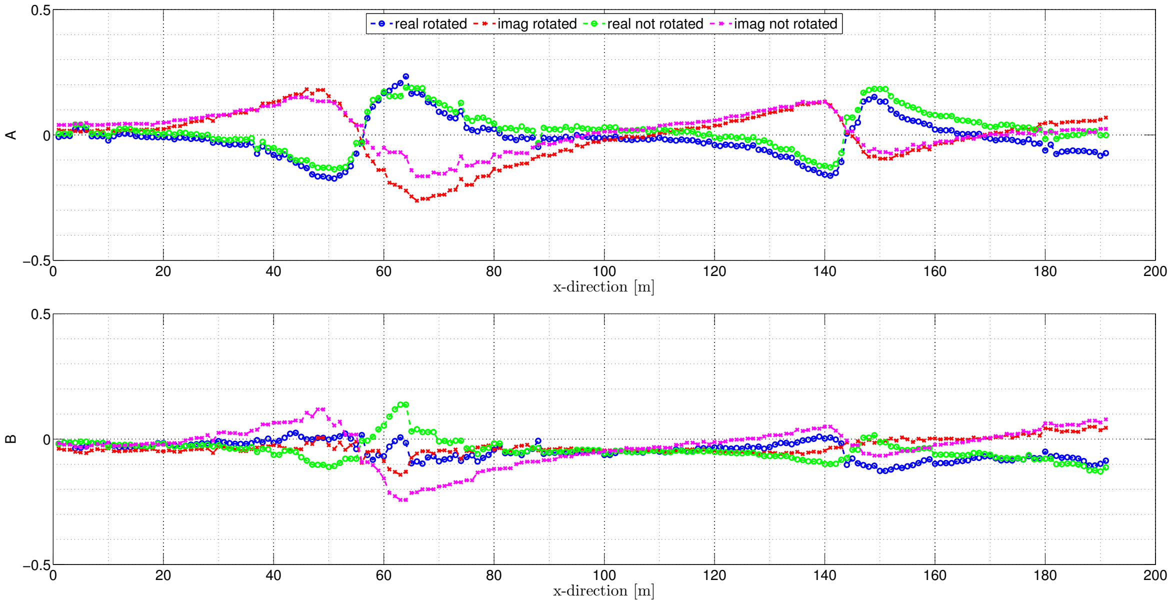

Figure 25: Magnetic transfer functions displayed against profile location. Top panel Tipper component A, bottom panel Tipper component B. Blue/green is the real part and red/purple the imaginary part of the Tipper. In blue and red are shown the results the rotated transfer functions. The transfer functions in green and purple are the not rotated ones.

4.7 Shift of the Transfer Functions

As shown above, the derived transfer functions are occasionally shifted along the y-axis. This effect can have several reasons, such as systematic errors, for example sensor rotations (cf. Section 5.2), natural/geological reasons, or the used processing approach.

The present section is dedicated to the influence of a scalar processing approach on the derived transfer functions. A shift in the transfer functions can have a big impact to the model fitting for mid-sized measurement areas (cf. Section 6.2.3). For example, inversion models for those areas may have difficulties to incorporate large scale geological features because the applied grids are dimensioned to adapt to the mid-sized measurement areas. A shift in the transfer functions may not be well fitted through the mid-sized subsurface model features. However, if the targets of an investigation are mid-sized features, a shift could be justified and reasonable regarding the inversion results.

In Figure 26, the transfer functions calculated with the least squares method are compared with an unshifted and a shifted version of the transfer functions calculated with the scalar method. The grey area is not used to calculate the RMS because the 19.6 kHz transmitter frequency is not resolved after profile meters 140 (cf. Figure 27). The magnitude of the shift of the scalar transfer functions in Figure 26 b) is their averaged value over the whole profile length. The transfer functions are shifted by this value toward the zero axis. This method to shift the transfer functions is purely technical. Nevertheless, the results presented in Figure 26 show one way to justify a shift of the scalar transfer functions.

For this, it is assumed that the transfer functions determined by the least squares method are better suited to investigate a survey area because information of more than one VLF transmitter is used. Figures 26 c) and d) show the differences of the respective transfer functions. It is clearly visible that the real part of the unshifted scalar transfer function has the largest deviation to the least squares solution with an RMS of 9.57 %. The real part also has the largest deviation from the x-axis. In comparison to this, the RMS of the shifted transfer function only has an RMS of 4.96 %. Thus, the RMS of the imaginary part of the transfer functions is almost similar for both the unshifted (6.91 %) and the shifted one (7.09 %). In total, the shifted transfer functions have an RMS of 8.65 % and the unshifted of 11.8 % compared to the transfer functions derived with least squares approach. As a result, it can be stated that the shifted transfer functions show a better accordance with the transfer functions obtained with the least squares solution.

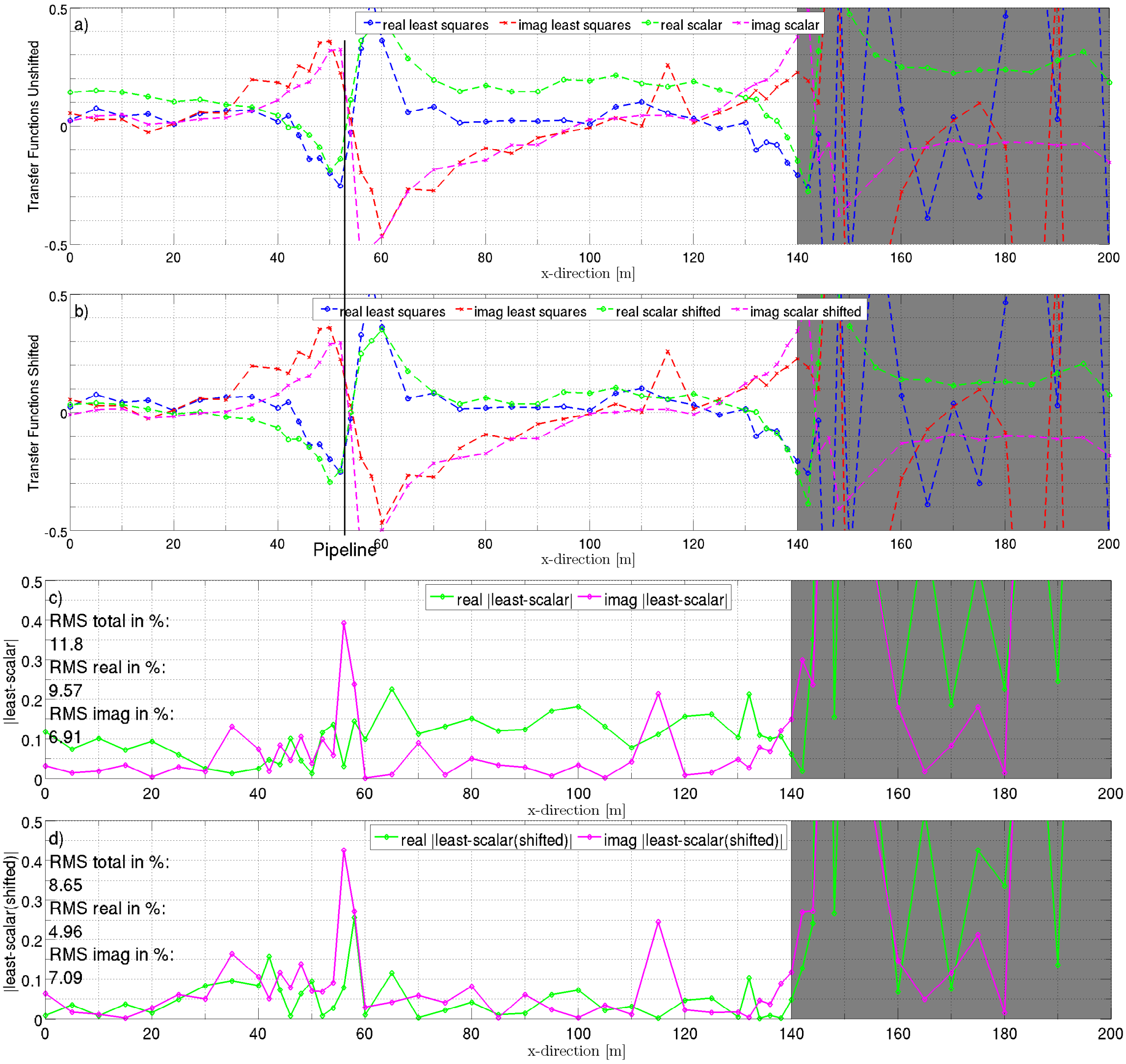

Figure 26: **a)** and **b)**: real and imaginary part of the transfer functions (Tipper) for the scalar (green and purple) and least square (blue and red) analysis. The transmitter frequency is 19.6 kHz and 23.4 kHz for the least squares and 23.4 kHz for the scalar analysis. **c)** and **d)**: absolute differences of the scalar Tipper compared to the least square one. The shifted Tipper (**b)** and **d)**) is in better agreement with the least squares solution than the unshifted. The RMS values indicate the differences between the scalar and the least squares solutions. For the shifted transfer functions the total RMS is lower and especially the real part shows a significantly lower RMS. The grey area indicates an unused frequency range for the RMS analysis.

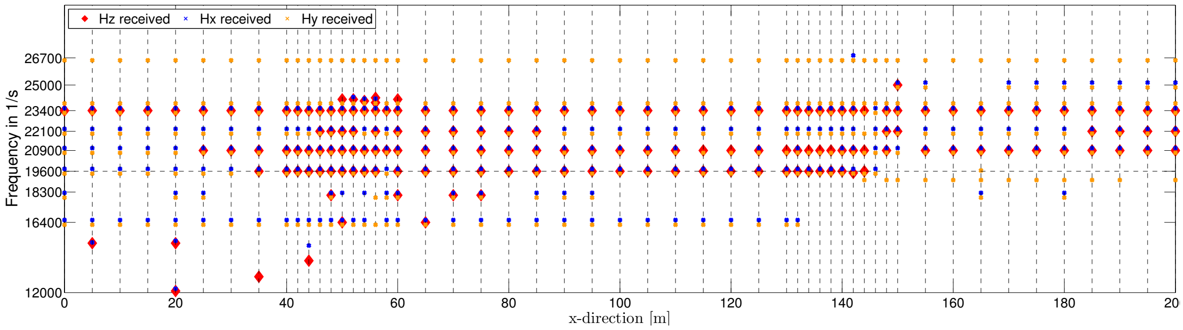

Figure 27: The y-axis shows common VLF frequencies. The x-axis shows the position along the profile. Resolved transmitters receive colour marks. Red dots mark H_z, blue dots H_x, and yellow dots H_y component of the magnetic field. Note that for the 19.6 kHz frequency the transmitter is not resolved after profile meters 140 meter.

5 Pre Flight Investigations

This chapter covers the preparative measurements before the first UAS flight. These measurements are necessary to construct a suitable suspension (cf. Section 3.3). The following sections describe and present the results of noise measurements and the effect of sensor rotation to the Tipper.

5.1 Noise Measurements

For the noise measurements, the helicopter is placed on top of an 80 cm high table. The wodden table board has a length of 2 m and a width of 1 m. The helicopter is tied with a rope to the table to keep it on the table top. The legs of the table are made of metal with rolls on their ends (cf. Figure 28).

Figure 28: Helicopter on top of the table during the noise measurements at a test side.

Four different noise measurements with different setups are carried out. During two of them, the sensor is moved while the logger is fixed outside of the helicopter's electromagnetic noise range. For the other two measurements, the location of logger and sensor is switched. Each device is moved once orthogonal and once parallel to the helicopter axis. Through this the influence of the helicopter noise on the devices is investigated separately. Additionally, the devices should ideally be placed in different distances to the helicopter and directly under the helicopter (z-direction). Since this was logistically not possible, the effect of the helicopter on the devices is investigated in two different directions as seen from the helicopter. This way, a possible direction-dependency of the helicopter noise is investigated and the conclusions for device positions directly under the helicopter are more robust.

In total, eleven measuring locations are defined for each noise measurement setup. The eleven measuring locations (respectively distances) of the devices are – with exception of the helicopter axis – the same for all four measurements (cf. Figure 29). The first measurement location is always between the skids of the helicopter (on top of the table), the second one on the ground directly under the helicopter (80 cm below). Followed by measurements three to ten increasing the distance to the point under the table horizontally by 50 cm each step (in meter: 0.5, 1.0, 1.5, 2.0, 2.5, 3.0, 3.5, 4.0) ending with 4 m distance. The last, eleventh, measurement is in 5 m horizontal distance to the helicopter. The highest possible sample frequency of 524,288 Hz is chosen for all measurements.

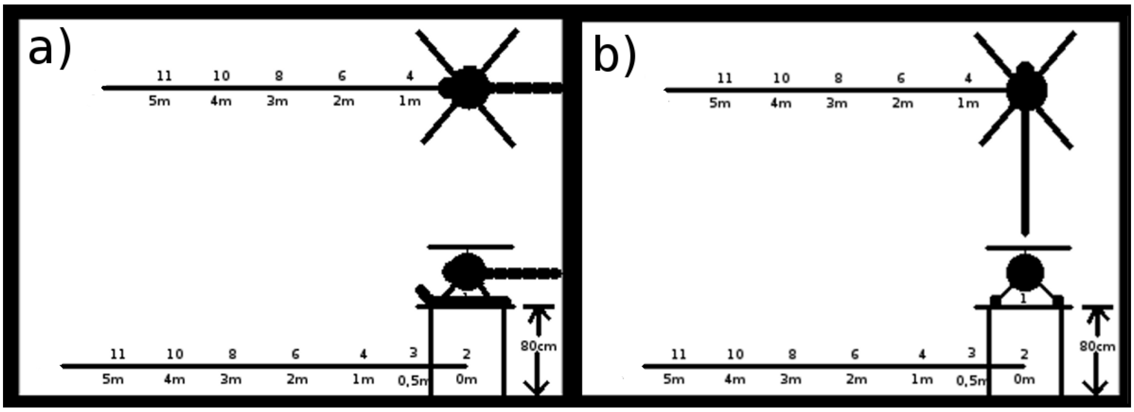

Figure 29: **a)** Measurement locations parallel to helicopter axis. **b)** Measurement locations orthogonal to helicopter axis. The first and second location is equivalent for a) and b). The sensor is on the top of the table between the skids of the helicopter (1) and under the table exactly under the helicopter (2), respectively.

The following figures show time series and power spectra of sensor and logger during the experiments. The presented time series and spectra give an overview of the electromagnetic noise of the helicopter at different locations.

Sensor outside Noise Range

Figure 30 exhibits the time series and resulting power spectra where the sensor is outside the noise range (at 15 m distance) and the logger is directly between the skids of the helicopter (for time series processing see Section 4.2). In order to see more details, a zoomed section of 16,384 samples is shown for all three magnetic components H_x, H_y, and H_z. The noise is clearly visible as spikes in the time series, most probably caused by the ignition circuit of the helicopter motor. These prominent noise features mask VLF transmitter signals in all magnetic field components (cf. Section 4.3).

Similar plots are presented in Figure 31, with a logger on the ground directly under the helicopter (80 cm below). The noise spikes in the time series are still persistent, but smaller than in the case above. In the power spectrum of the H_x component, the transmitter frequency of 23.4 kHz is resolved.

If the logger is at a horizontal distance of 2 m (orthogonal to the helicopter axis, case b) in Figure 29), no noise is visible in the time series. The spectra shows numerous transmitters in all three magnetic components (cf. Figure 32). Thus, 2 m distance between the helicopter and the logger is estimated to be sufficient.

Logger outside Noise Range

The experiment above, with the sensor outside of noise range (at 15 m distance), showed that at distances of around 2 m from the helicopter, noise is not critically influencing the logger (cf. Figure 32). This does not apply for the sensor as shown in the next figures.

Figure 33 shows the noise of the helicopter affecting the sensor. The logger is out of noise range of the helicopter and the sensor is moved parallel to the helicopter axis (cf. Figure 29, case a)). Although the times series are strongly influenced by the helicopter, they show no distinct spikes as they are seen in the reversed case for the logger. This may be the reason why the 23.4 kHz transmitter is resolved at least in the H_x component.

In the 2 m case (cf. Figure 34), where the influence of the helicopter on the logger is considerably smaller, this is not true for the sensor. Although an influence of the times series is hardly noticeable, resolved transmitters are only visible in the spectrum of H_x.

In Figure 35, at a distance to the helicopter of 4 m (along the helicopter axis), the noise influence of the helicopter is further decreased. The amplitudes of the time series are smaller than at 2 m distance (indicating noise as a source of larger amplitudes) and in the resulting power spectra, several transmitters are resolved for all three magnetic field components. Thus, 4 m helicopter to sensor distance is estimated to be sufficient.

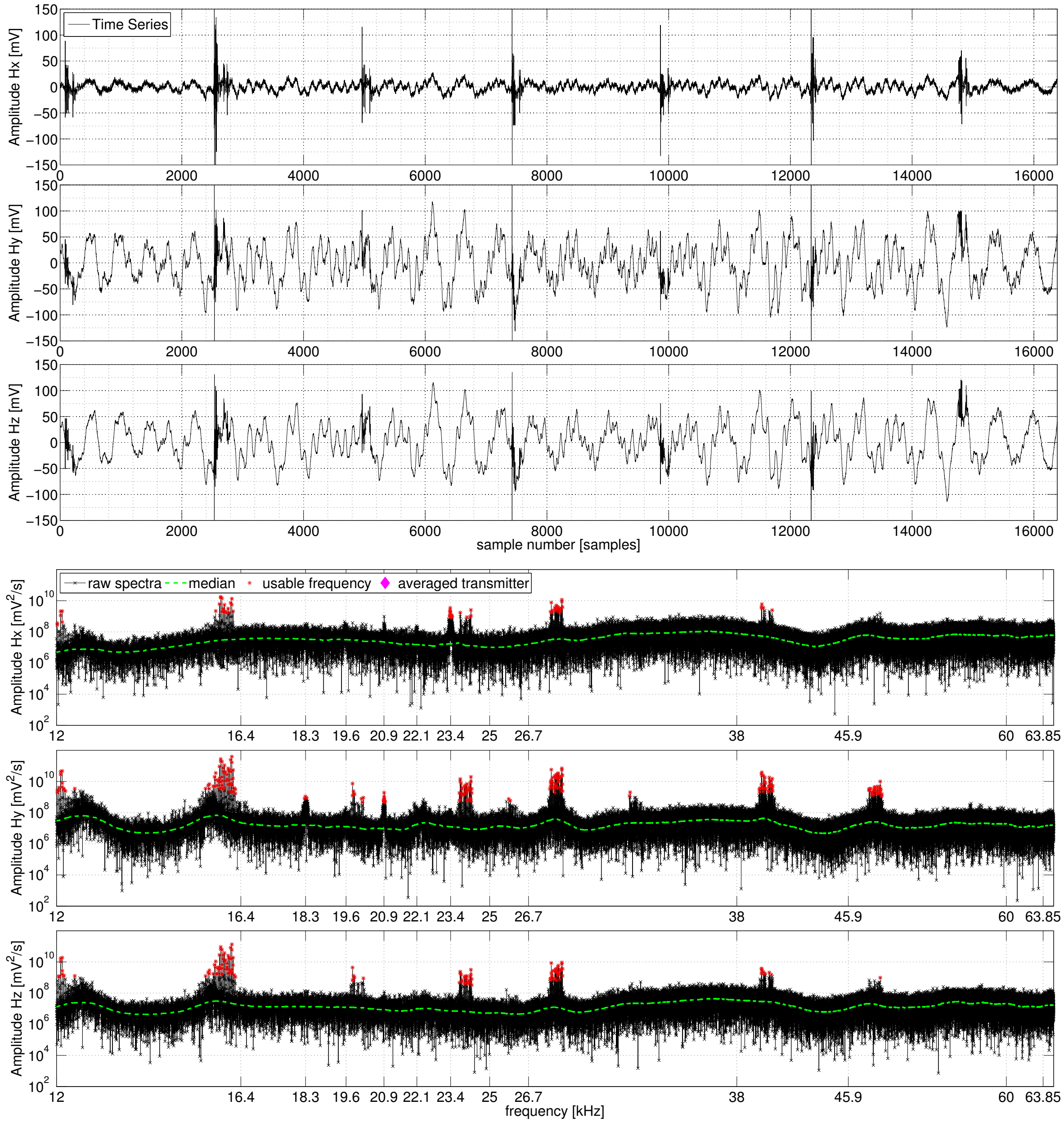

Figure 30: Logger between the skids. **Top:** Times series of the three magnetic field components. **Bottom:** In black the spectra of the three magnetic field components derived of the time series. The median is plotted in dashed green. Points over a predefined noise level of 30 dB over the median are marked red as potentially usable. Purple points indicate resolved transmitters.

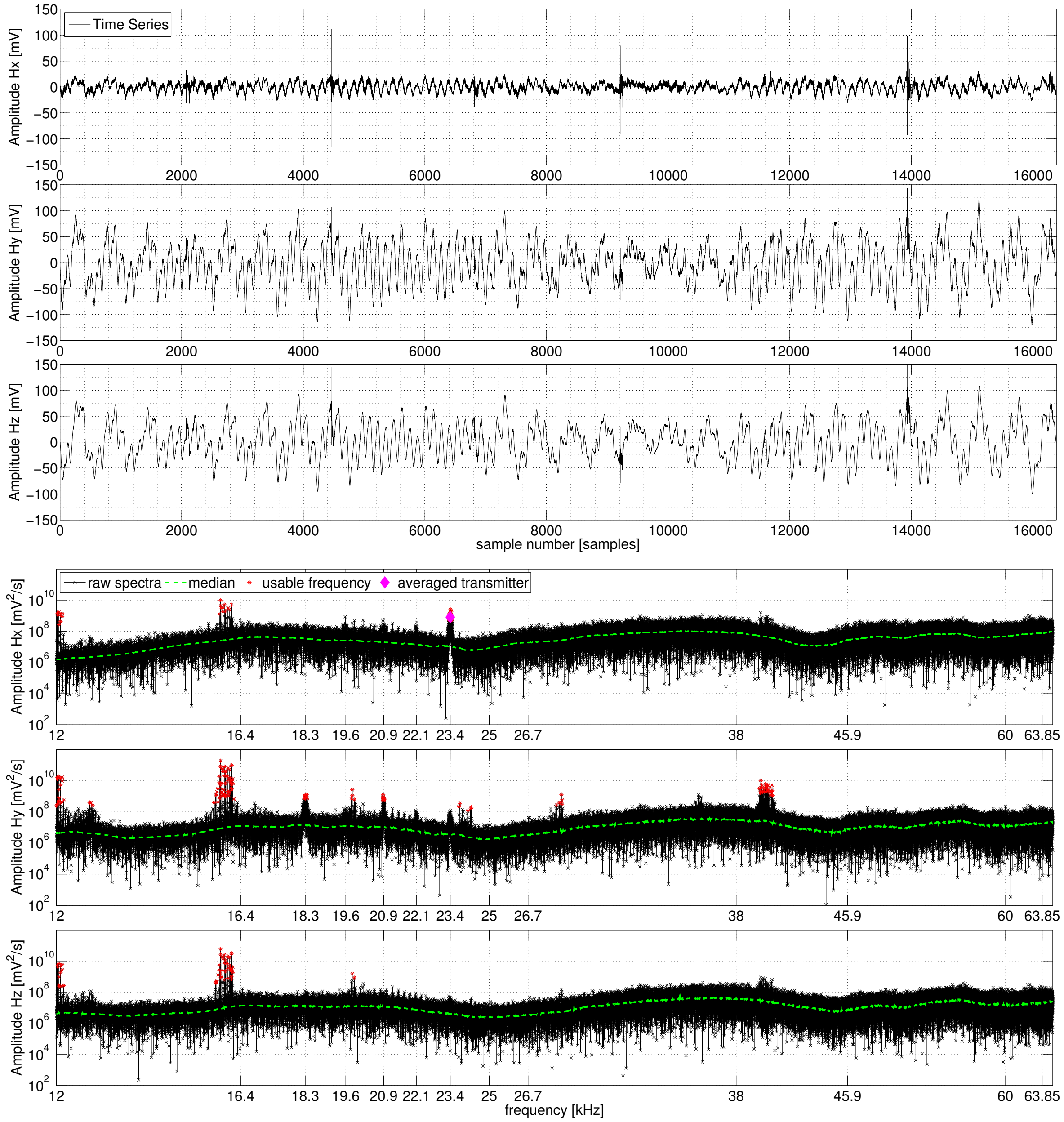

Figure 31: Logger on the ground directly under the table. **Top:** Times series of the three magnetic field components. **Bottom:** In black the spectra of the three magnetic field components derived of the time series. The median is plotted in dashed green. Points over a predefined noise level of 30 dB over the median are marked red as potentially usable. Purple points indicate resolved transmitters.

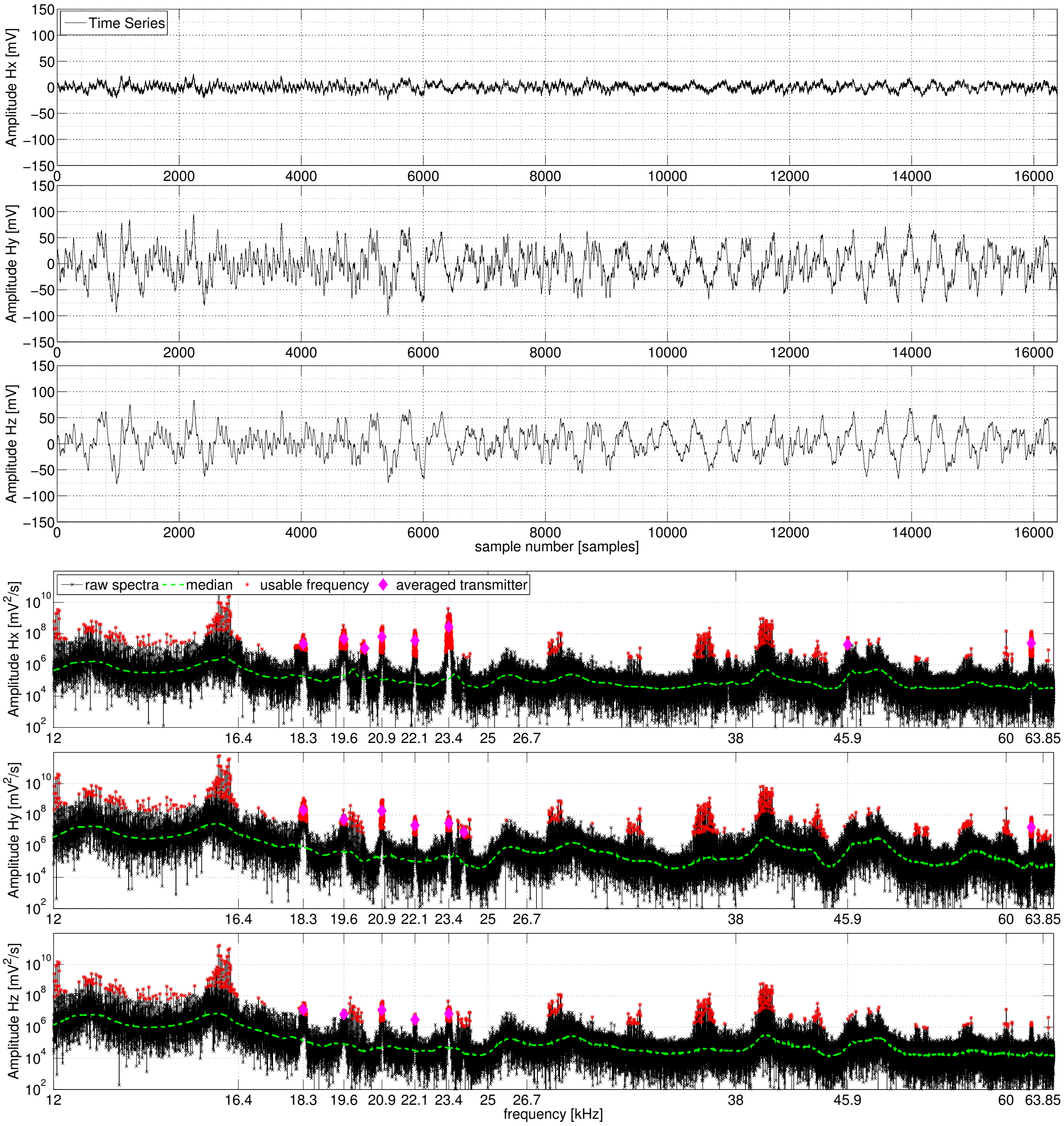

Figure 32: Logger in two meters distance, orthogonal to the helicopter axis. **Top:** Times series of the three magnetic field components. **Bottom:** In black the spectra of the three magnetic field components derived of the time series. The median is plotted in dashed green. Points over a predefined noise level of 30 dB over the median are marked red as potentially usable. Purple points indicate resolved transmitters.

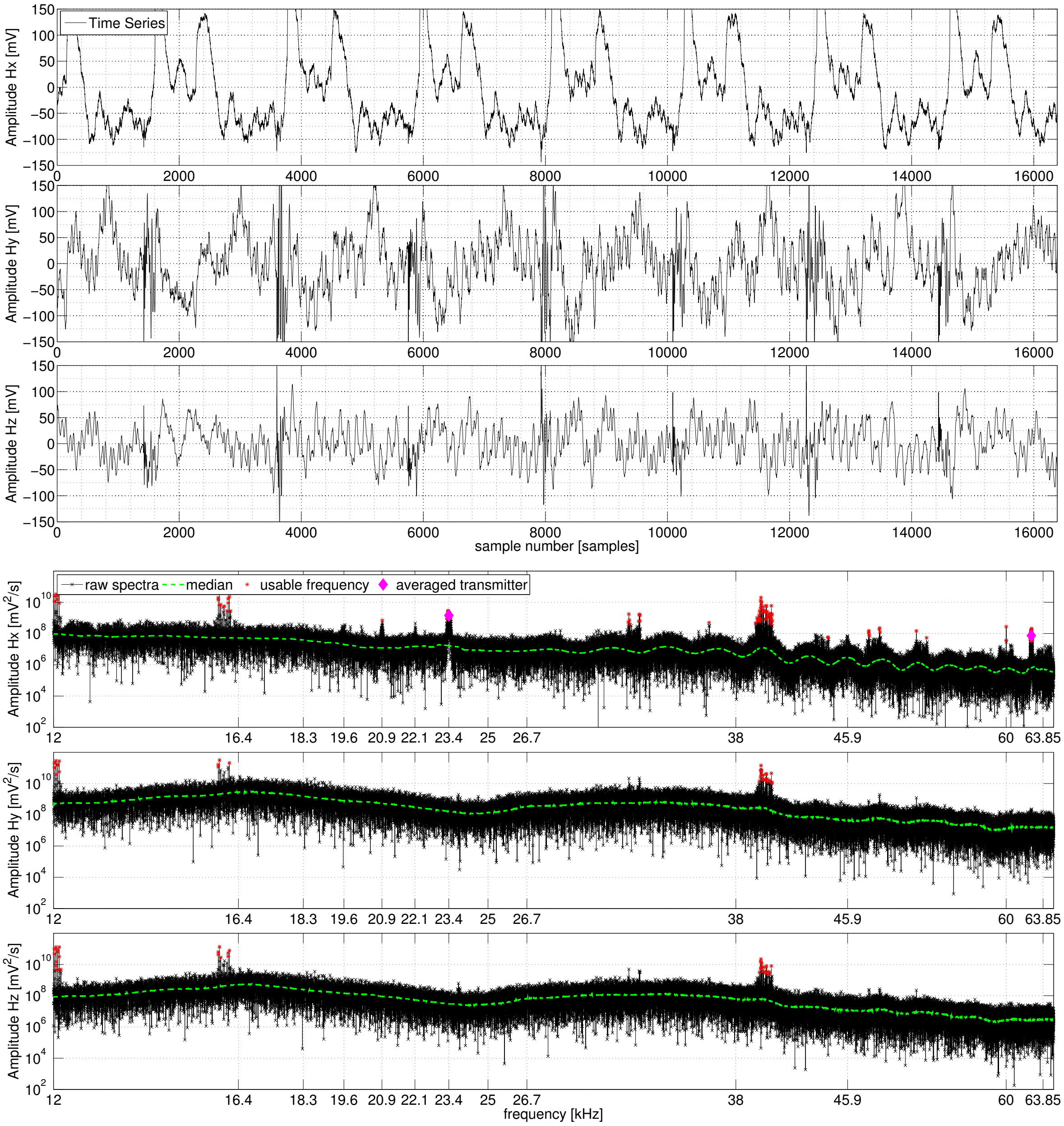

Figure 33: Sensor located between skids. **Top:** Times series of the three magnetic field components. **Bottom:** In black the spectra of the three magnetic field components derived of the time series. The median is plotted in dashed green. Points over a predefined noise level of 30 dB over the median are marked red as potentially usable. Purple points indicate resolved transmitters.

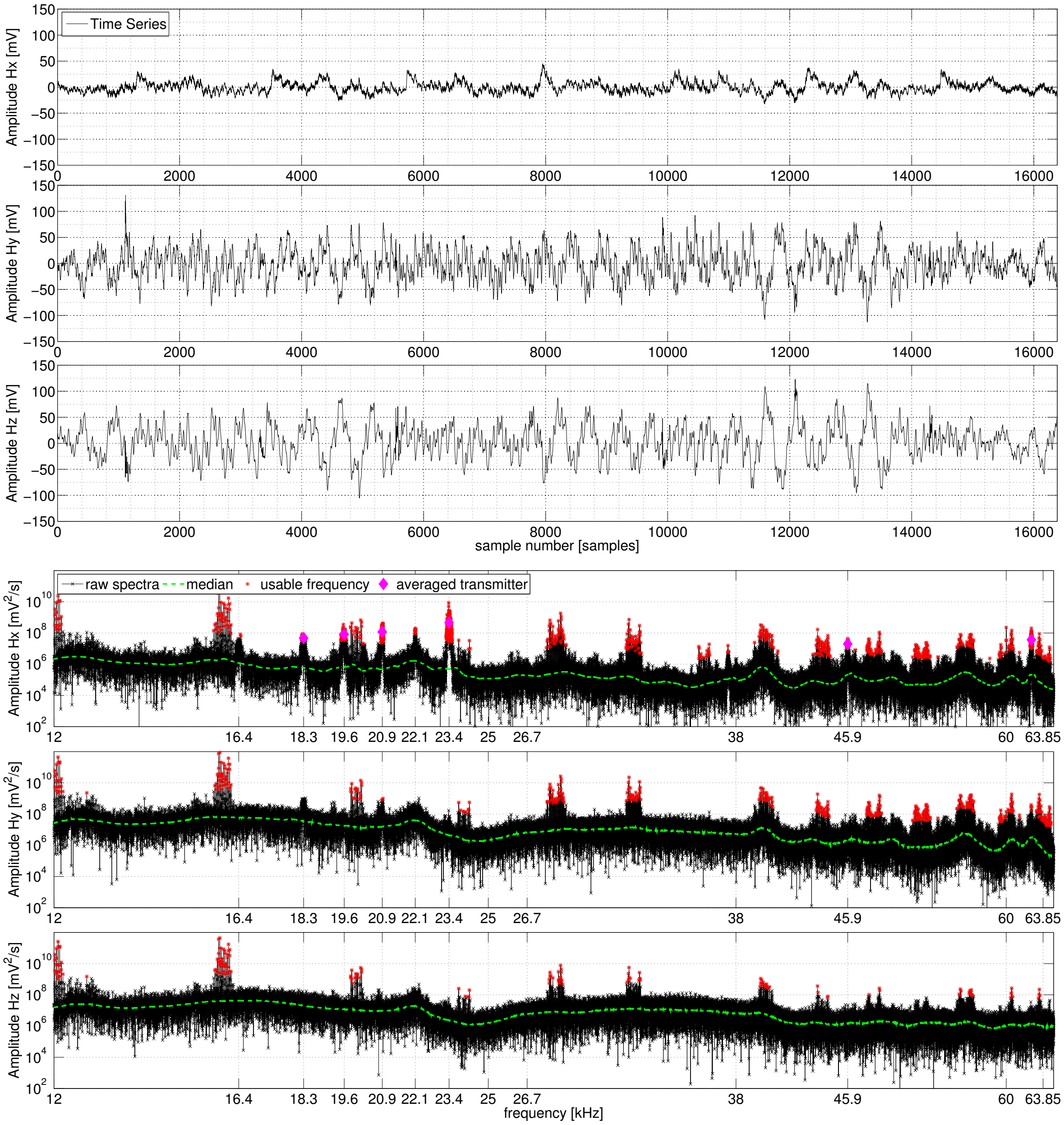

Figure 34: Sensor in two meters distance, parallel to helicopter axis. **Top:** Times series of the three magnetic field components. **Bottom:** In black the spectra of the three magnetic field components derived of the time series. The median is plotted in dashed green. Points over a predefined noise level of 30 dB over the median are marked red as potentially usable. Purple points indicate resolved transmitters.

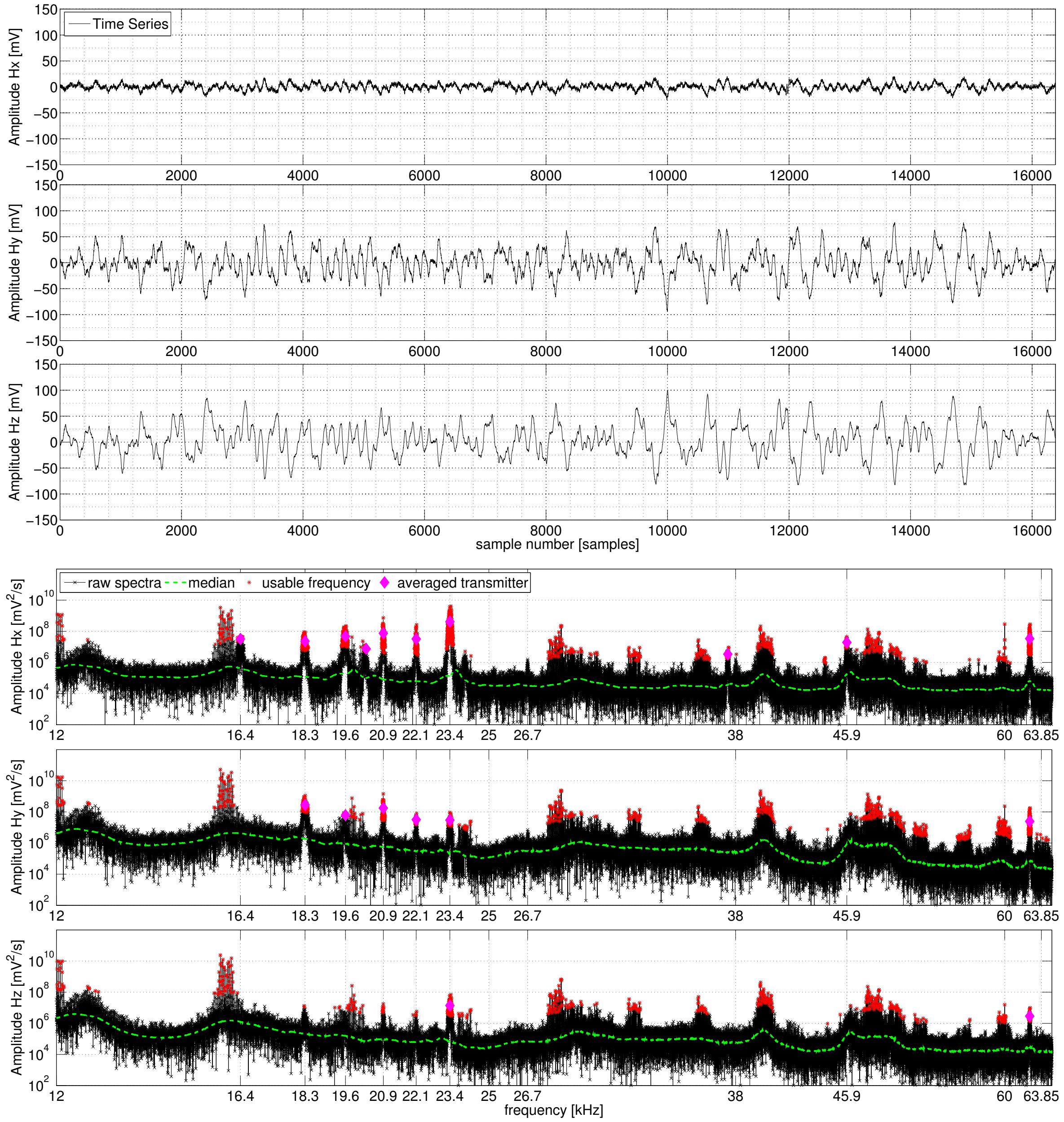

Figure 35: Sensor in four meters distance, parallel to helicopter axis. **Top:** Times series of the three magnetic field components. **Bottom:** In black the spectra of the three magnetic field components derived of the time series. The median is plotted in dashed green. Points over a predefined noise level of 30 dB over the median are marked red as potentially usable. Purple points indicate resolved transmitters.

Helicopter Noise, Summary

The next figures summarize the results. These enable to receive important information regarding the composition of the suspension.

In Figures 36 – 39, the top panels show the resolved transmitters at the device locations. The bottom panels show the level of the background amplitude in the spectra as a function of distance to the helicopter in dB, at selected frequencies. If the difference between raw spectra and the applied moving median (dashed green in Figures 30 – 35) exceeds 30 dB, the transmitter is classified as resolved. Experience gathered during the present thesis shows that interpretable transfer functions are only retrieved if a resolvable transmitter is available in the H_z component (red points). Calculating transfer functions from transmitters with a signal to noise ratio smaller than 30 dB is possible, but it results in increasingly unstable transfer functions. In most cases, the Tipper shows random noise behaviour, making transfer functions hard to interpret or uninterpretable (e. g. Section 4.4, Figures 15 c) and d)).

The outcome of the experiment with fixed sensor and varying logger position orthogonal to the helicopter is shown in Figure 36. The first transmitters are resolved in a distance of 1 – 1.5 m. In this range, most of the receivable VLF frequencies part from the background level.

The results with fixed sensor and parallel to the helicopter moved logger (cf. Figure 37) do not give such a clear picture. This implicates that the noise characteristic of the helicopter is direction dependent.

For the 23.4 kHz frequency, the background noise level first decreases at the position under the helicopter, then increases until 1 m and finally decreases until the transmitter signal stays relatively stable from 2.5 m to 5 m. Transmitters other than the 23.4 kHz transmitter are received at 4 – 5 m distance.

During a real flight, the logger is directly under the helicopter. This means that a noise measurement ideally covers the z-direction. Since no data for more than 80 cm under the helicopter is available (considering the worst case scenario of large noise even at higher z-distances), the conclusion of this part of the experiment is that it should have a minimum distance of 1.5 meter to the helicopter.

The results shown in Figure 38 are for the fixed logger and the orthogonally to the helicopter axis moved sensor. Although the median noise level decreases with distance, it is not possible to resolve any transmitter in the H_z component.

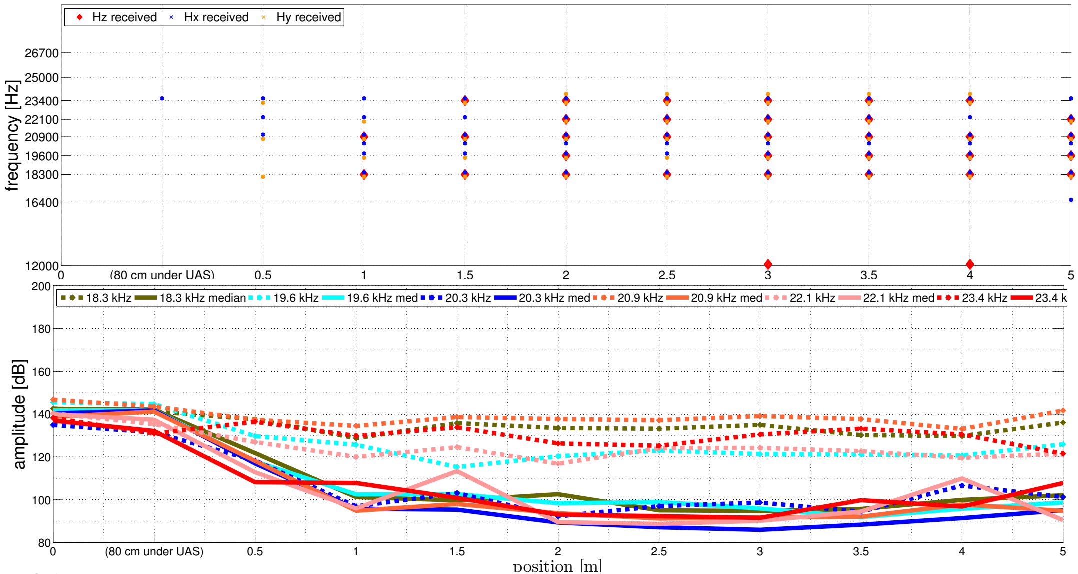

Figure 36: Fixed sensor and orthogonal to the helicopter axis moved logger. 0 on the y-axis indicates that the sensor is between the helicopter skids, horizontal distances to the helicopter begin at 0.5 m. **Top:** Transmitter 30 dB over noise level. Blue indicates H_x, yellow H_y, and red H_z components. The red H_z component is the most important one for an adequate data analysis. **Bottom:** Level of background amplitude (median) of the H_z spectra in dB (plotted as solid lines) and level of the amplitude of the VLF transmitter dB (plotted as dashed lines).

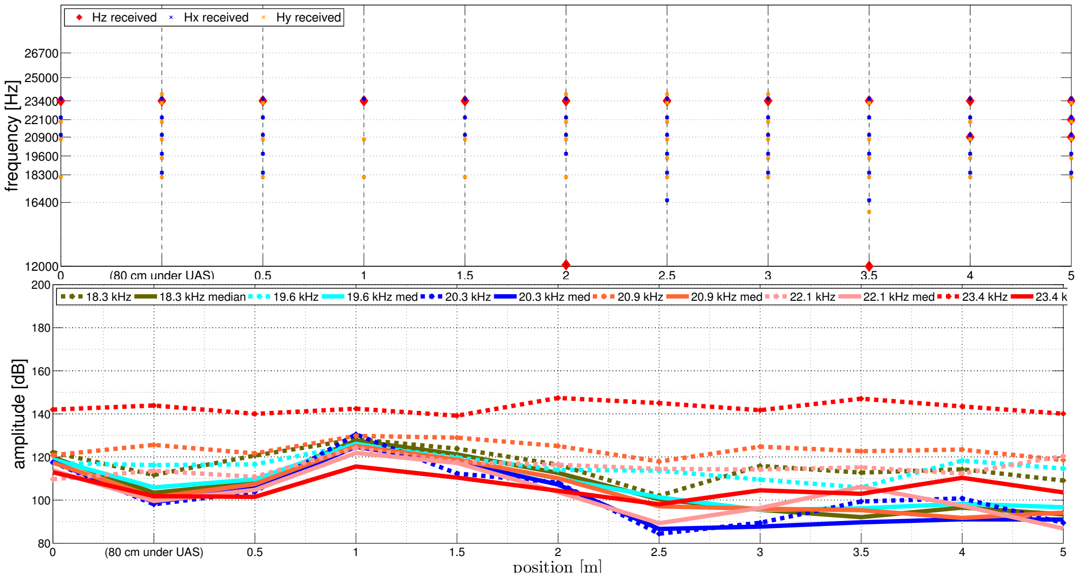

Figure 37: Fixed sensor and parallel to the helicopter axis moved logger. 0 on the y-axis indicates that the sensor is between the helicopter skids, horizontal distances to the helicopter begin at 0.5 m. **Top:** Transmitter 30 dB over noise level. Blue indicates H_x, yellow H_y, and red H_z components. The red H_z component is the most important one for an adequate data analysis. **Bottom:** Level of background amplitude (median) of the H_z spectra in dB (plotted as solid lines) and level of the amplitude of the VLF transmitter dB (plotted as dashed lines).

In Figure 39, the logger is fixed and the sensor is moved parallel to the helicopter axis. With the exception of the first location, the median noise level also decreases constantly with distance, in this experiment. However, transmitters are not resolved until distances of 4 – 5 m. Since the measurement for first measuring point should be redundant (the data is recorded between helicopter skids), the same data as in Figure 38 is used in Figure 39. However, the noise of the helicopter is not constant. One reason that could cause these noise fluctuations is that the gas supply was not constant during the measurements (i. e. in irregular intervals he changed the idle state of the helicopter). This may also be the reason for the fluctuating noise behaviour visible in Figure 37. To clarify this, further investigations need to be made, in which the gas supply of the helicopter is changed in a controlled way. Nevertheless, the outcome of this part of the noise test is that the required distance of the sensor to the helicopter is minimum 4 – 5 m, better more.

Reference Measurement

Finally, to be able to compare data influenced by helicopter to noise free data, the following plots show a reference measurement. The reference measurement is located 100 m apart from the previous helicopter position and conducted 1 day later. Four measurements are carried out during 3 m.

Figure 40 shows the time series and spectra of a reference measurement. The amplitudes and appearances of the times series, as well as those of the spectra, are comparable with the ones of Figures 35 and 32, where the noise of the helicopter is not clearly identifiable. This indicates that helicopter noise barely influences the logger at distances greater than 2 m and the sensor at distances greater than 4 m.

Figure 41 contains three important pieces of information: Firstly, only the 23.4 kHz transmitter is resolved in the H_z component of all four measurements. Secondly, amplitudes of the median and the transmitter frequency are constant in the spectra. Finally, the median noise level agrees well (at a level from 85 to 100 dB) with the median noise level of Figures 36 to 39 at large distances to the helicopter. However, the dB value of the VLF transmitter frequencies is in general lower compared to Figures 36 to 39. This is most obvious for the 23.4 kHz frequency, which is at a level of 120 dB in the reference measurements but at around 140 dB for most noise measurements. This means that the background noise level remains relatively constant, but the amplitude of the VLF transmitters does not. This result leads to the conclusion that other noise sources possibly also influence the quality of the spectra, not only the helicopter noise. Other sources may be atmospheric disturbances, discontinuities in transmitter radiations, or local anthropogenic influences (e. g. trains). To clarify this, further investigations are required to analyse different noise sources.

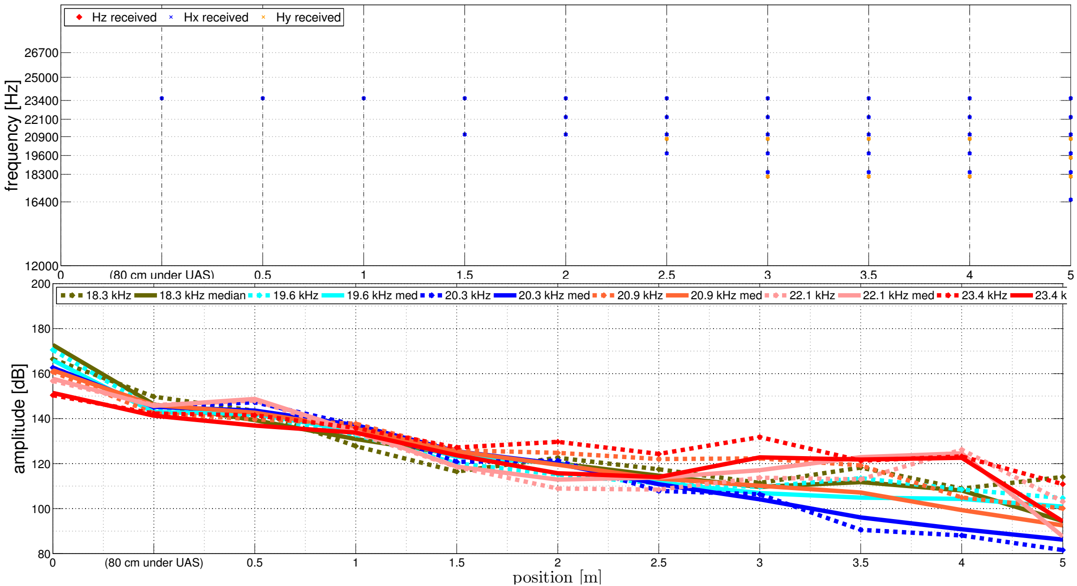

Figure 38: Fixed logger and orthogonal to the helicopter axis moved sensor. 0 on the y-axis indicates that the sensor is between the helicopter skids, horizontal distances to the helicopter begin at 0.5 m. **Top:** Transmitter 30 dB over noise level. Blue indicates H_x, yellow H_y, and red H_z components. The red H_z component is the most important one for an adequate data analysis. **Bottom:** Level of background amplitude (median) of the H_z spectra in dB (plotted as solid lines) and level of the amplitude of the VLF transmitter dB (plotted as dashed lines).

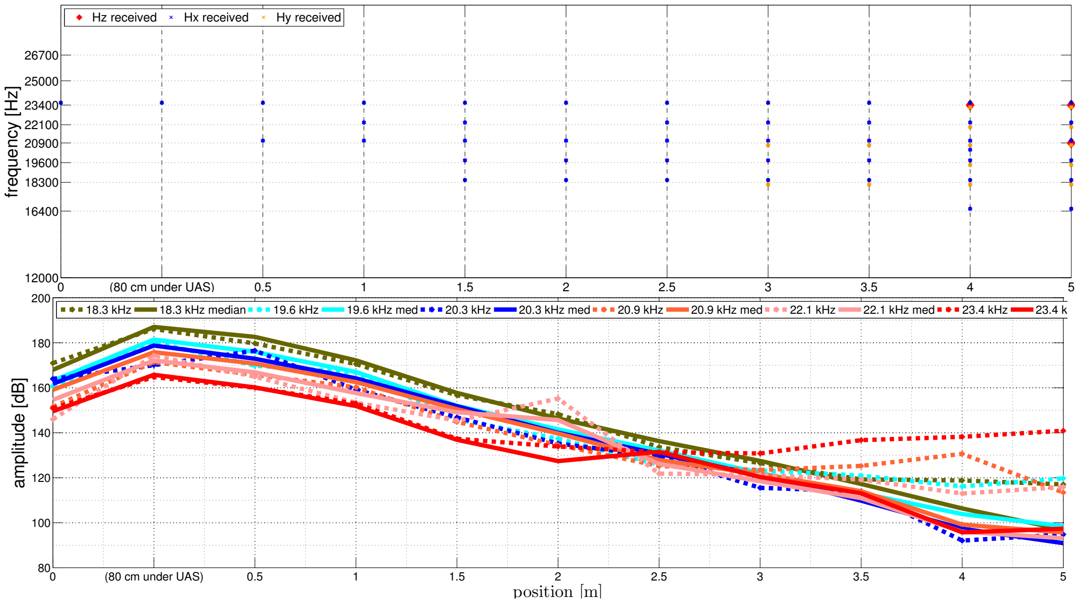

Figure 39: Fixed logger and parallel to the helicopter axis moved sensor. 0 on the y-axis indicates that the sensor is between the helicopter skids, horizontal distances to the helicopter begin at 0.5 m. **Top:** Transmitter 30 dB over noise level. Blue indicates H_x, yellow H_y, and red H_z components. The red H_z component is the most important one for an adequate data analysis. **Bottom:** Level of background amplitude (median) of the H_z spectra in dB (plotted as solid lines) and level of the amplitude of the VLF transmitter dB (plotted as dashed lines).

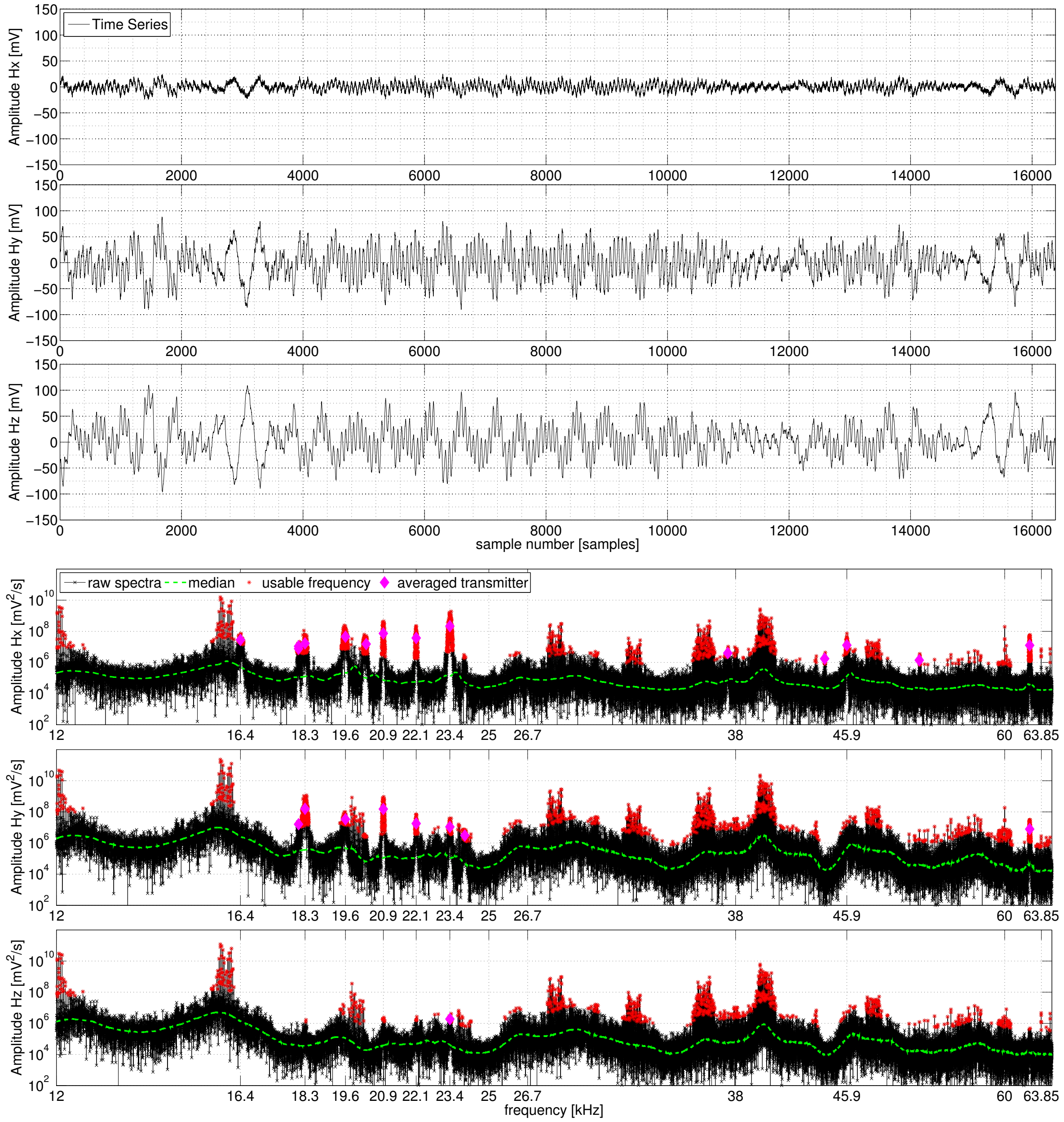

Figure 40: Reference measurement: **Top:** Times series of the three magnetic field components. **Bottom:** In black the spectra of the three magnetic field components derived of the time series. The median is plotted in dashed green. Points over a predefined noise level of 30 dB over the median are marked red as potentially usable. Purple points indicate resolved transmitters.

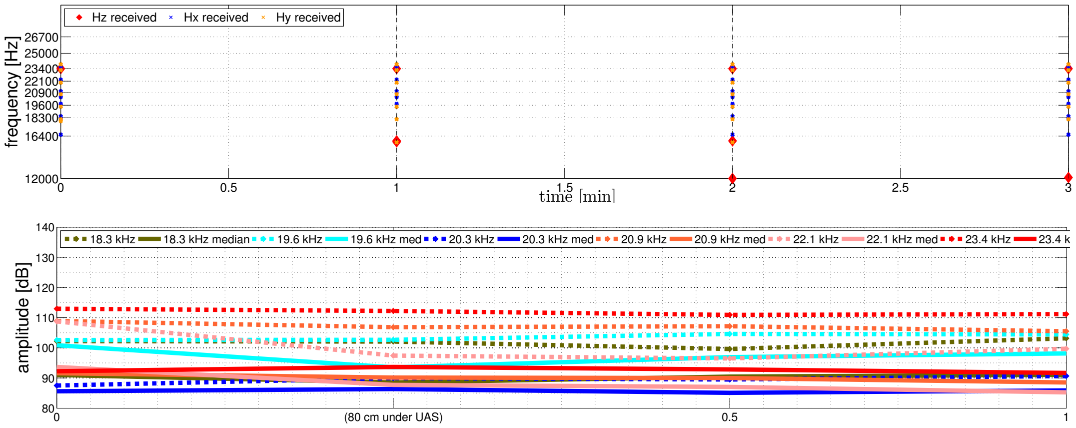

Figure 41: Four reference measurements. **Top:** Transmitter 30 dB over noise level. Blue indicates H$_x$, yellow H$_y$, and red H$_z$ components. The red H_z component is the most important one for an adequate data analysis. **Bottom:** Level of background amplitude (median) of the H_z spectra in dB (plotted as solid lines) and level of the amplitude of the VLF transmitter dB (plotted as dashed lines).

5.2 Rotation of the Sensor

To be able to construct an adequate suspension, it is necessary to know how sensor rotations affect the transfer functions. Furthermore, it is important to know to what extent a rotation can be neglected.

To answer these questions, an experiment is carried out. In a first step, the sensor is fixed but rotated in steps of 5° (from -90° to +90°) around the y-axis (cf. Figure 42). 0° represents the ideal case of an unrotated sensor – as it should be for groundbased measurements with an appropriate frame. The second step is to repeat this experiment but rotate the setting by 5° around the z-axis (changing the x- and y-direction of the sensor by 5°). This results in a different x-axis orientation.

Figures 43 – 45 show the real and imaginary part of the transfer functions as a function of sensor rotation and the absolute differences of the rotated transfer functions to the 0° position. The figures are displayed in three zoom steps and the 0° position equals the orientation of the sensor during field measurements. The Tipper calculation is scalar (approximated transmitter direction, 110° N). The frequency 23.4 kHz is used. The blue and red lines indicate the real and imaginary parts of the transfer functions during the first part of the experiment (sensor fixed but rotated in 5° steps – from -90° to + 90° – around the y-axis), with the direction of the x-axis of the sensor approximately oriented to 50° N. The green and purple lines indicate the real and imaginary parts of the transfer functions of the second part of the experiment where the setting was rotated by 5° around the z-axis, but otherwise the first experiment repeated (x-axis is approximately oriented to 55° N).

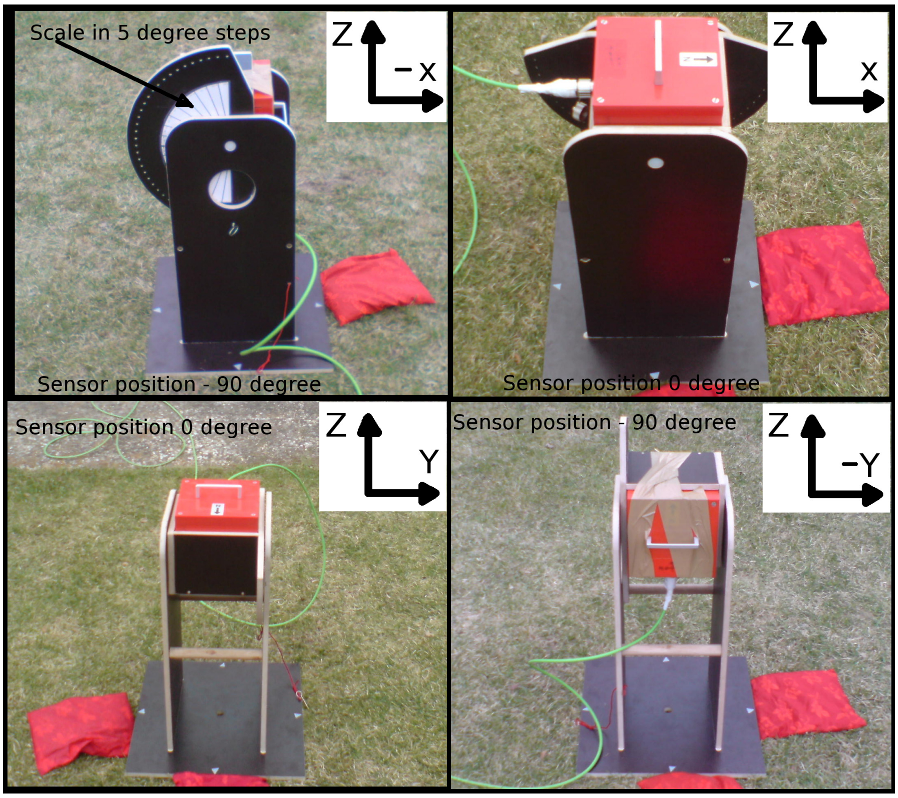

Figure 42: Rotation of the sensor in steps of 5°. The starting position is -90° (upper left and lower right). The sensor orientation of the 0° position in this experiment matches the ideal one during measurements (upper right and lower left). The setting is adjusted into a horizontal position with red pillows.

Sensor Rotation Analysis

The first zoom step is shown in Figure 43. The large influence of rotation on the absolute amplitudes of the transfer functions is demonstrated. Even if the y-axis scale – depicting the amplitude of the transfer function – is set to values of ± 5, the A component is out of scale in the range from -75 to -85° (for comparison the usual y-axis scale for Tipper components is ± 0.5 in the present thesis).

Generally, the real part of the transfer function reacts instantaneously and much stronger to rotation in comparison to the imaginary part. Also, the influence of rotation is larger for the A component of the Tipper than for the B component. This is confirmed by the trend of the absolute differences. The results of the second part of the experiment, with the setting rotated by 5° around the z-axis, agree with the results of the first part of the experiment. The largest difference in the results is a shift of the transfer functions. The real part of the A component shifts away from the zero axis, resulting in an even larger effect of rotation. The real part the

B component shifts toward the zero axis, decreasing the effect of rotation.

The second zoom step is shown in Figure 44, with an y-axis scale of ± 2. The features described for the first zoom step are more distinct. Thus, better comparison between the two experiments of different x-axis orientations is possible. The z-axis rotation has almost no effect on the A component of the transfer functions. Only a slight shift away from the zero axis in the range from 45 – 90° is visible for both the real and the imaginary part. An effect on the B component of the transfer functions is only visible in the real part. The transfer function is shifted towards the zero axis, implying a smaller effect of y-axis rotation on the real part of the transfer function component B.

In the third zoom step (cf. Figure 45), the scale for the A and B part of the Tipper is chosen more realistically. Transfer functions of typical anomalies in the present thesis are usually plotted with a y-axis scale of ± 0.5 and the anomalies have an amplitude of ± 0.1 to ± 0.25. In order to be able to identify anomalies, errors in the transfer functions should not exceed ± 0.01 to ± 0.02 (dashed and solid line in the absolute differences plot in Figures 43 – 45). This is approximately 10 % of the determined anomaly values in the present thesis. However, this is an arbitrary value that serves as a general orientation since it matches with experiences made for the transfer functions in the present thesis, but also with other works. For example, Pedersen et al. [2009] use a y-axis scale of -0.4 – 0.3 to plot the Tipper and the presented anomalies have an amplitude of ± 0.05 to ± 0.3. Thus, according to the magnitude of a measured anomaly, this range of ± 0.01 to ± 0.02 should be adapted.

This implies that rotation of less than 2°, result in absolute differences of the real part of the Tipper of more than 0.02, which is above the prior defined limit. For the imaginary part, again taking the 0.02 limit as reference, y-rotation from 10° up to 35° do not have large influence on the Tipper. However, the influence depends on the Tipper component and slightly on the x-orientation. Concluding, to be able to record interpretable data, the suspension must possibly prohibit every rotation of the sensor larger than 2°, because the real part of the transfer function is the limiting factor.

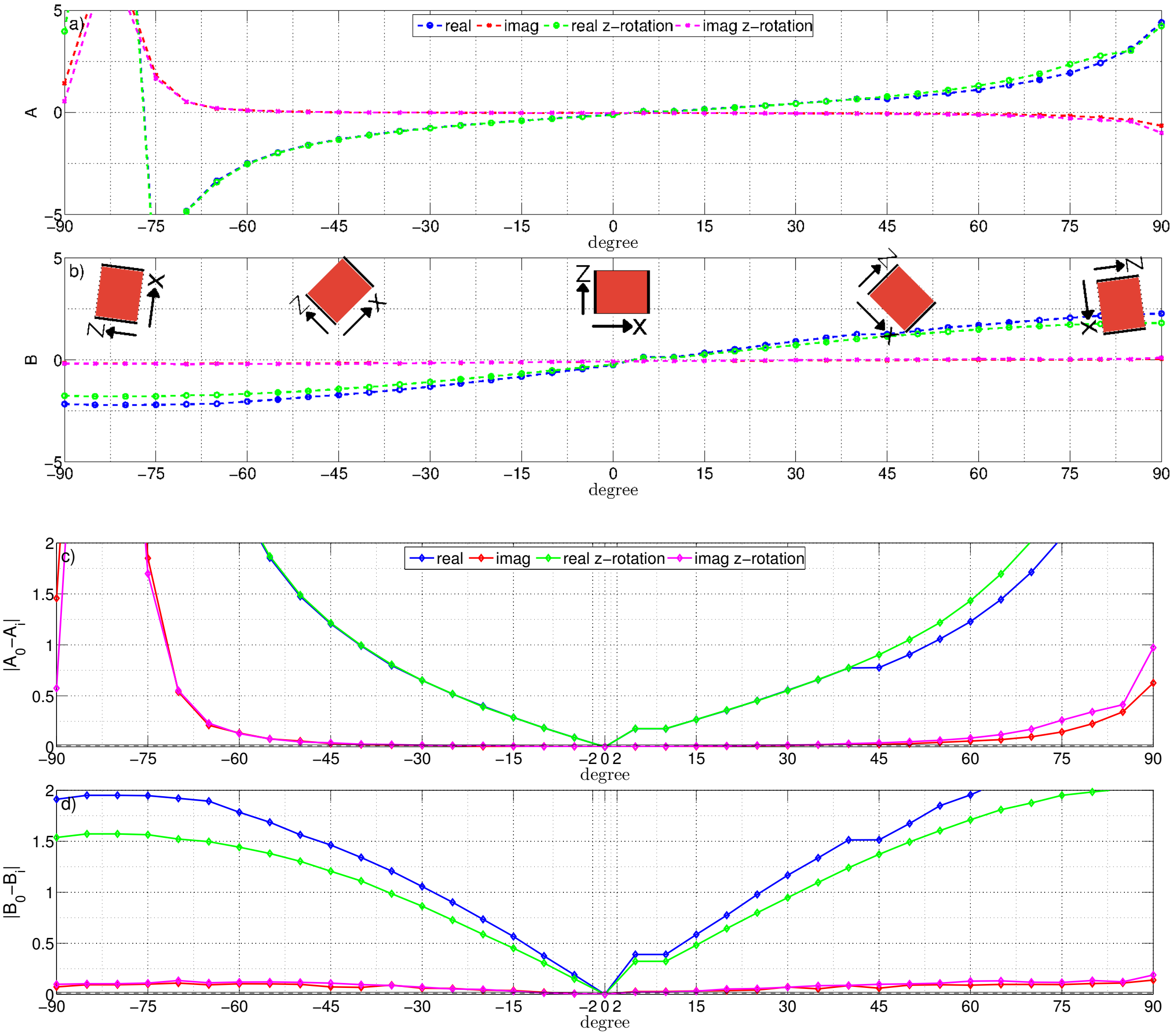

Figure 43: a) and b): Real and imaginary part of the transfer functions (tipper) A and B for two different x-directions of the sensor against the rotation of the sensor around its y-axis. Transmitter frequency: 23.4 kHz, scalar analysis. In the case plotted in green and purple, the x-axis direction of the sensor differs by 5° compared to the red and blue one. In b), the sensor rotation is indicated with red boxes. **c) and d):** Absolute differences of the Tipper compared to the zero rotation value. The y-axes of the plots cover a broad range to provide an overview.

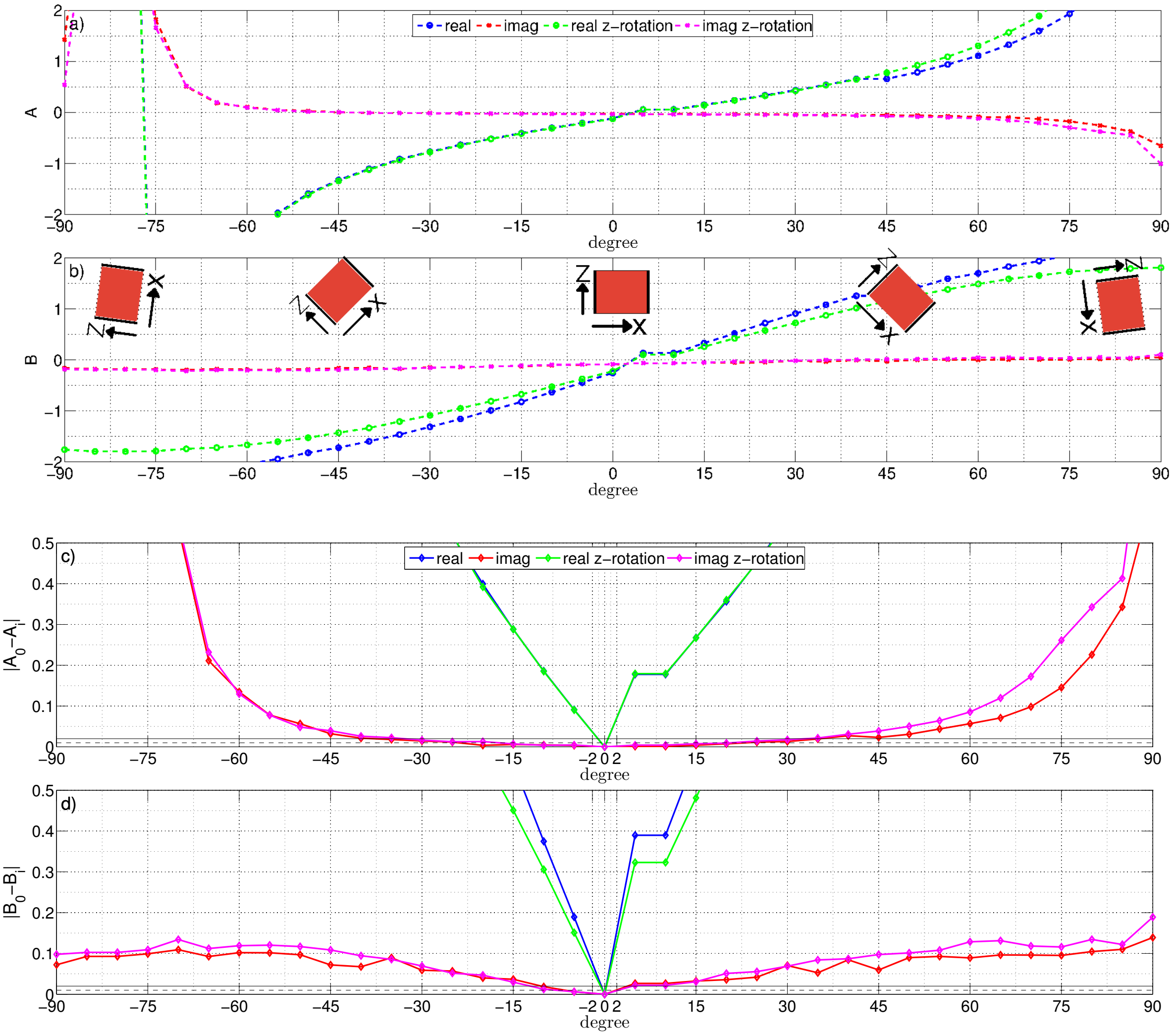

Figure 44: a) and b): Real and imaginary part of the transfer functions (tipper) A and B for two different x-directions of the sensor against the rotation of the sensor around its y-axis. Transmitter frequency: 23.4 kHz, scalar analysis. In the case plotted in green and purple, the x-axis direction of the sensor differs by 5° compared to the red and blue one. In b), the sensor rotation is indicated with red boxes. **c) and d):** Absolute differences of the Tipper compared to the zero rotation value. The variation of the Tipper functions in comparison to values after rotation should be less than 0.01 – 0.02 (dash and solid line) to achieve interpretable data for UAS-VLF problems. The y-axes of the plots cover a medium range for more details.

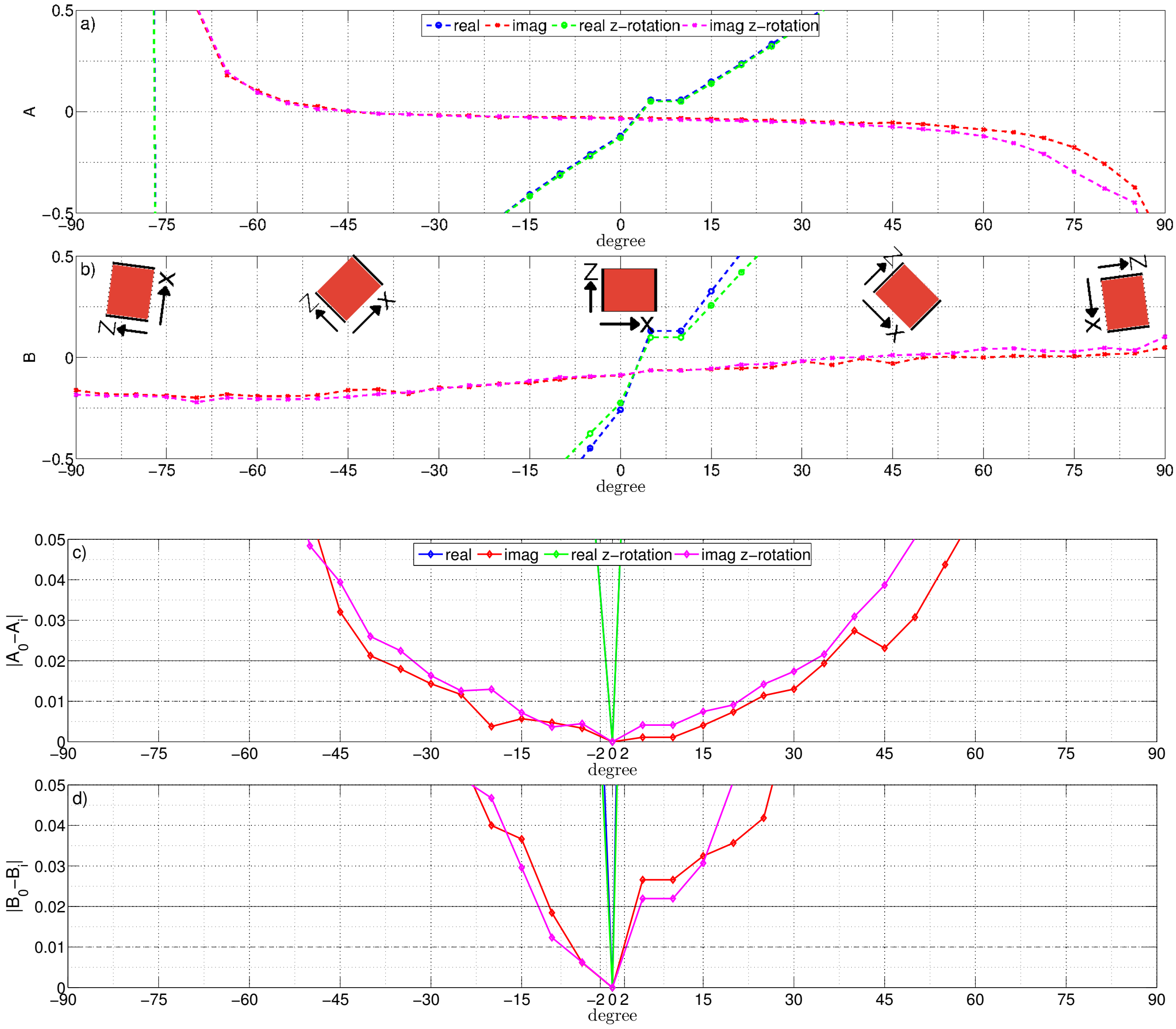

Figure 45: a) and b): Real and imaginary part of the transfer functions (tipper) A and B for two different x-directions of the sensor against the rotation of the sensor around its y-axis. Transmitter frequency: 23.4 kHz, scalar analysis. In the case plotted in green and purple, the x-axis direction of the sensor differs by 5° compared to the red and blue one. In b), the sensor rotation is indicated with red boxes. **c) and d):** Absolute differences of the Tipper compared to the zero rotation value. In the present thesis transfer functions variations due to rotation of less than 0.01 to 0.02 (dash and solid line) count as tolerable to achieve interpretable data for UAS-VLF problems. The y-axes of the plots cover a realistic range for comparison with field data.

Different Transmitter Frequency

Since the transmitter direction may influence the results of the experiment, two transmitters with different directions are compared in Figure 46. The important directions are:

- Direction of the x-axis of the sensor, approximately 50° N.
- Transmitter direction of the 20.3 kHz frequency, approximately 52° N.
- Transmitter direction of the 23.4 kHz frequency, approximately 110° N.

Note that the 20.3 kHz transmitter exhibits small amplitude fluctuations during the measurements. This influences the quality of the calculated transfer function. As a result, the transfer functions obtained with the 23.4 kHz frequency are smoother than the ones obtained with the 20.3 kHz transmitter.

The most prominent difference in Figure 46 is visible in the transfer functions of the real part of B, with a sign reversal for positive and negative y-rotation and a sign reversal for the imaginary part of A for positive y-rotation (compared to the transfer functions of the 23.4 kHz frequency, respectively). Furthermore, the real parts of the Tipper of the 20.3 kHz frequency appear to be influenced less by rotation than the real parts of the Tipper of the 23.4 kHz frequency. This becomes especially prominent for B, if the absolute differences are regarded. Nevertheless, the conclusion remains that a suspension must possibly prohibit rotation of the sensor to be able to record interpretable data.

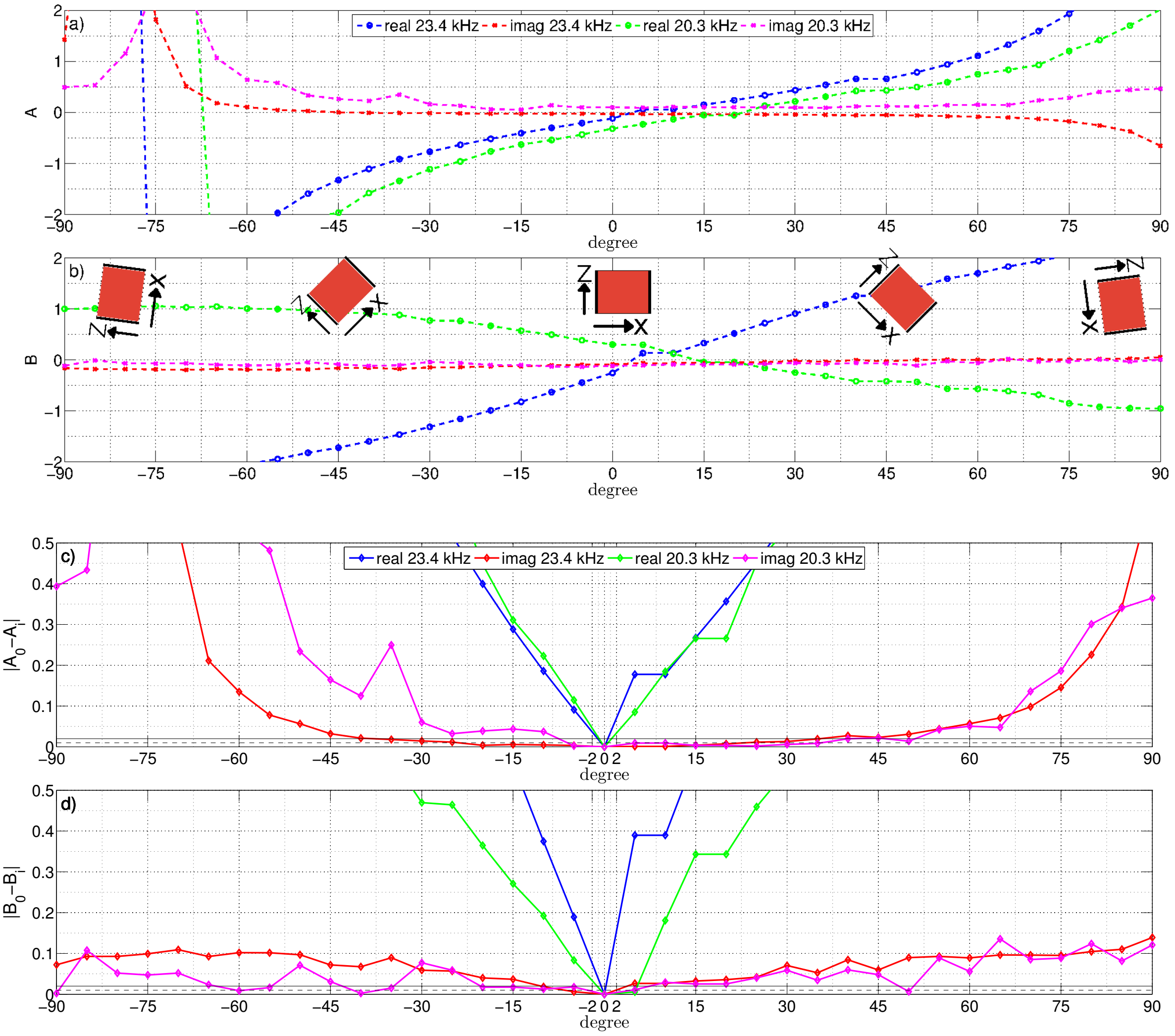

Figure 46: a) and b): Real and imaginary part of the transfer functions (tipper) A and B for two different x-directions of the sensor against the rotation of the sensor around its y-axis. Transmitter frequency: 23.4 kHz, scalar analysis. In the case plotted in green and purple, the x-axis direction of the sensor differs by 5° compared to the red and blue one. In b), the sensor rotation is indicated with red boxes. **c) and d):** Absolute differences of the Tipper compared to the zero rotation value. The variation of the Tipper functions in comparison to values after rotation should be less than 0.01 – 0.02 (dash and solid line) to achieve interpretable data for UAS-VLF problems. The y-axes of the plots covers a medium range to have an overview but also be able to see details.

Bivariate Approach

The final step of this experiment is to look at transfer functions obtained with the bivariate approach, that is calculated with the least squares solution. In Figure 47, the results of this approach are compared to the scalar transfer functions. The real and imaginary parts of A are almost similar to the scalar results for negative rotation. However, for positive rotation, the transfer function of the imaginary part is more robust to rotation, as shown by the absolute differences. For B, the transfer functions obtained with the bivariate method are generally less sensitive to rotation. This is clearly visible in the absolute differences plot. It is also visible that the real part is under the limit of 0.01 for a wide y-rotation range.

Summarizing, the chosen approach has a distinct influence on the data quality. This final experiment shows that sensor rotation have less influence on the transfer functions if determined with the bivariate approach, that is the transfer functions are stabilized against deviations originated from sensor rotation. The cause of this effect and the question whether this is a general feature, has yet to be investigated in detail.

However, it is not always possible to calculate the transfer functions using the bivariate approach. Sometimes, only one transmitter frequency is received. In these cases, the stabilizing effect of the least squares approach can not be applied. Having in mind that the goal is to construct an appropriate suspension that is applicable in all cases, the conclusion is that it should prohibit rotation of the sensor as much as possible.

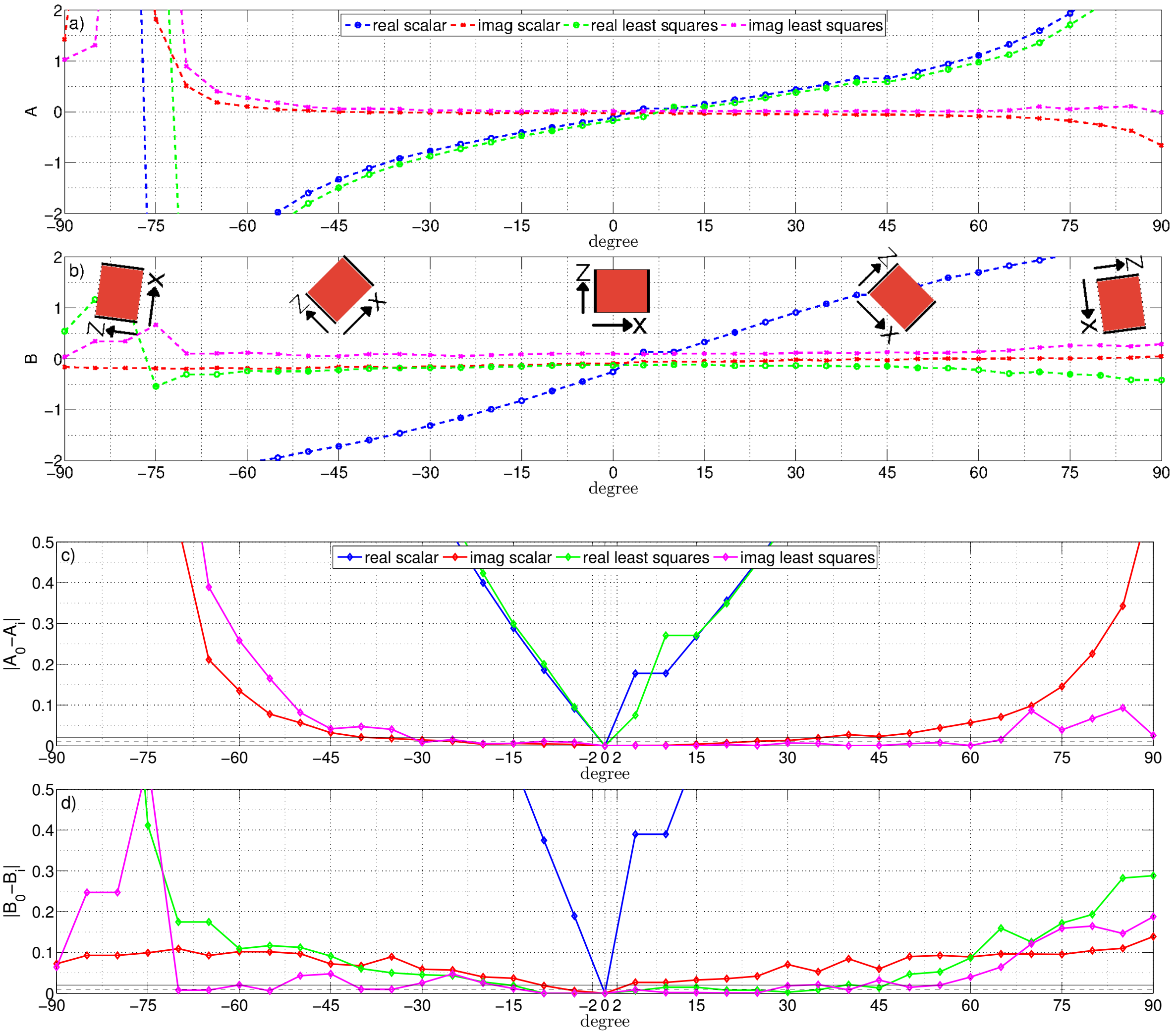

Figure 47: a) and b): Real and imaginary part of the transfer functions (tipper) A and B for two different x-directions of the sensor against the rotation of the sensor around its y-axis. Transmitter frequency: 23.4 kHz, scalar analysis. In the case plotted in green and purple, the x-axis direction of the sensor differs by 5° compared to the red and blue one. In b), the sensor rotation is indicated with red boxes. **c) and d):** Absolute differences of the Tipper compared to the zero rotation value. The variation of the Tipper functions in comparison to values after rotation should be less than 0.01 – 0.02 (dash and solid line) to achieve interpretable data for UAS-VLF problems. The sensor rotation is indicated with red boxes. The y-axes of the plots covers a medium range to have an overview but also be able to see details.

6 Field Campaigns

This chapter is divided into the two sites of the field campaigns. Each section starts with an introduction of the survey area. The first site in Wavre features two anthropogenic anomalies and the second site in Cuxhaven a salt- to freshwater transition zone.

After the survey areas are described, RMT inversion and modelling results are presented, giving an impression of the subsurface resistivity distribution. However, the present thesis concentrates on the UAS-VLF results. Finally, subsurface resistivity models obtained through the inversion of ground-based VLF data and UAS-VLF data are presented. For the RMT modelling and inversion, the code of Rodi and Mackie [2001], and for the VLF modelling and inversion, the code of Key et al. [2012] is used.

In order to understand the modelling and inversion settings, it is necessary to shortly describe the realization of the UAS-VLF measurements. The height of the sensor for the presented UAS-VLF measurements is approximately 3 m and 1 m for VLF ground measurements, respectively. Since the altitude is not controlled automatically during flight (the pilot adjusts the height remotely), deviations (especially to higher altitudes of up to 4 m) from the assumed 3 m occur. After the pilot positions the UAS at the start of a profile, the UAS flies automatically with a constant speed of 1 m/s to a checkpoint along the profile. Additional information on how the UAS-VLF measurements are realized are given in Section 4.1.

6.1 Wavre

In the following sections, the survey area in Wavre is introduced and the results of the first UAS-VLF measurements, are presented. The survey area for these measurements is Wavre, near Neuchâtel, Switzerland (cf. Section 6.1.1). The aim of the field campaign is to investigate if and how well two anthropogenic anomalies are detected by the UAS-VLF method.

As part of the study in Wavre, the obtained RMT data is shown, inverted and modelled. The background resistivity information of the RMT data is used as a basis for the VLF modelling and inversion. Finally, the results of RMT and VLF are compared.

6.1.1 Survey Area

The first UAS-VLF measurements were carried out in April 2012 in Wavre, near Neuchâtel, Switzerland (cf. Figure 48). The area was previously investigated by Bosch and Müller [2005] revealing two prominent anthropogenic anomalies, a buried power cable and a pipeline at a distance of approximately 90 m to each other. Based on the expected strong VLF signals of the anomalies, this site is chosen for the first UAS-VLF measurements with an unmanned helicopter, in order to investigate the feasibility of the method.

The power cable is oriented at approximately 57° N and the pipeline at 71° N (both plotted in blue, cf. Figure 48). The course of the pipeline is determined by surface markers and the location of the power cable is described by Bosch and Müller [2005]. In total, five parallel profiles with a spacing of 10 m are investigated with the RMT method. Subsequently, three of them are additionally measured using UAS-VLF and one with ground-based fixed-frame VLF. Security concerns prohibited measurements using UAS-VLF on profile 1 and 2: A 2.5 m high obstacle and a road are located between profiles 1 and 2, prevent a measurement with the UAS.

Ground-based VLF measurements by foot – the sensor hand-held – are also carried out. However, they provide no additional information compared to the ground-based fixed frame VLF measurement regarding transfer function characteristics of ground-based VLF measurements. Additionally, the determination of positions of the data points is not unique as it is not possible to keep the movement speed constant along an entire profile. Therefore, this VLF data is not well suited for a comparison with the UAS-VLF data and thus not part of the present thesis.

The profile length is 200 m and the profile direction 128° N. The profiles are numbered from 1 to 5. The profiles of interest (UAS-VLF and RMT data) are the profiles 3 to 5, plotted in purple. The directions of two important (strong signal and good availability) transmitters of 18.3 kHz and 23.4 kHz are indicated in red (270° N and 3° N, respectively). Finally, the forecasted intersection points of the profiles and the anomalies are marked at 60 and 145 m of profile 3 and at 72 and 150 m of profile 5 in Figure 48.

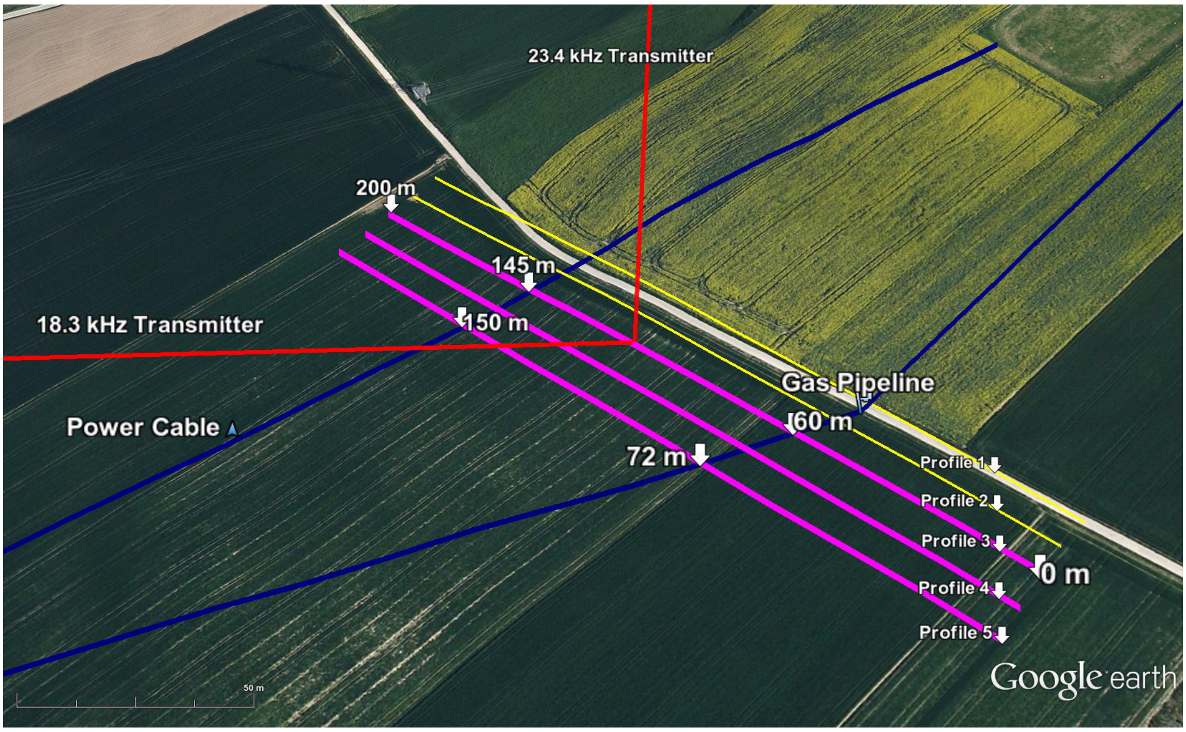

Figure 48: Survey area at Wavre, Switzerland. The profiles investigated in the present thesis are plotted in purple. Anomalies are plotted in blue and indicated transmitter directions in red. The pipeline is crossed at profile meter ∼60 of profile 3 and profile meter ∼72 of profile 5. The power cable is crossed at profile meter ∼145 of profile 3 and profile meter ∼150 of profile 5 [Google-earth, 2012].

6.1.2 RMT

This section discusses the results of the RMT measurements in Wavre. Prior to the inversion of the RMT data, an appropriate value for the regularization parameter λ is obtained (cf. Section 2.4.4). For this, a sample L-Curve is shown in Figure 49. The location of the corner of the L-curve indicates a reasonable choice for the trade-off between data norm and model norm [Hansen and O'Leary, 1993]. The value of the regularization parameter λ used for the subsurface inversion models is 5. The starting models for the RMT inversions are a homogeneous half space with a resistivity of 20 Ohm-m. This value is an estimation motivated by RMT resistivity data (cf. Figure 51) .

Figure 50 shows the inversion results of profile 3. In the result of the TE inversion (electric field in strike direktion), the two conductive anomalies at 56 m (pipeline) and 144 m (power cable) are clearly detectable. In contrast, the conductive anomalies derived from the TM inversion (electric field orthogonal to strike direktion) are much smaller in terms of conductivity. The joint inversion result clearly resolves both conductive anomalies. Additionally, the horizontal width of the conductive anomalies is smaller compared to the TE-mode, resulting in a slightly higher resolution of the position of the anomalies. The background resistivities lie between 10 Ohm-m and 50 Ohm-m. With an RMS of about 2 % (cf. equation (59)) for all three models, the measured data is explained well by the inversion models.

In total, the RMT measurements cover frequencies from 38 kHz – 603 kHz. Figure 51 shows a comparison between measured data and the calculated data of the TE inversion for three exemplary frequencies. This gives an insight into the quality of the RMT inversion for single frequencies which contain information on subsurface depth ranges that are comparable to VLF frequencies. The 153 kHz frequency data is fitted with an RMS of 2.11 %, the 77 kHz frequency data with an RMS of 0.96 %, and the 44 kHz frequency data with an RMS of 1.34 %. The background resistivities of 30 Ohm-m as well as the resistivities of the anomalies at profile meters 56 and 144 are well fitted by the presented frequencies. The same is true for the fit of the phases. However, the quality of the data fit is frequency-dependent: It is better for the 77 kHz frequency and worse for the 153 kHz frequency. In contrast to the single frequency RMS, where measured phases and resistivities of only one frequency are used, the total RMS value of a model uses the phase and resistivity of all measured frequencies. This is the reason for the slightly different values.

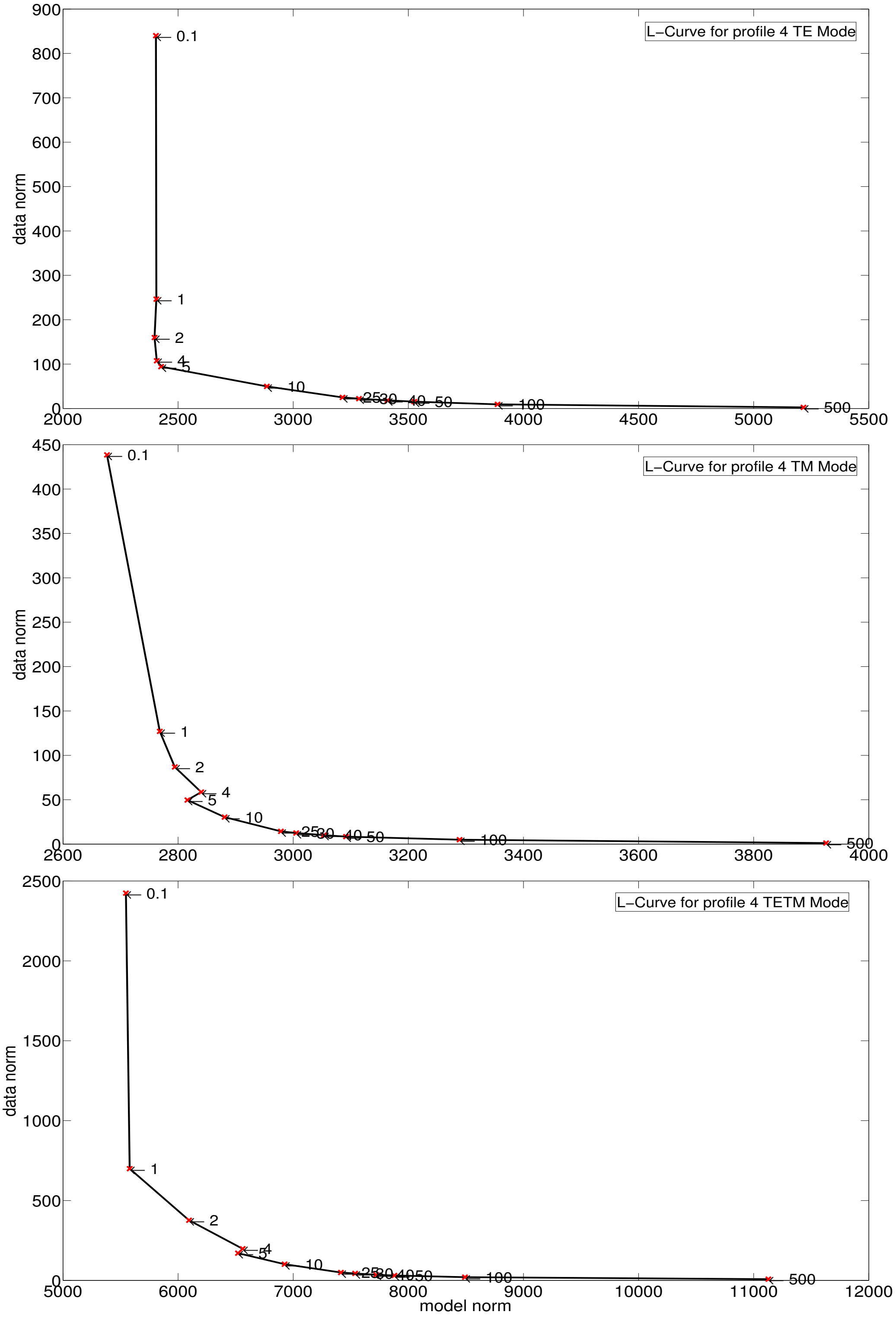

Figure 49: L-Curve profile 4: Data norm versus the model norm for the TE-mode, TM-mode, and joint inversion. A corner in the L-curve indicates an appropriate regularization parameter λ.

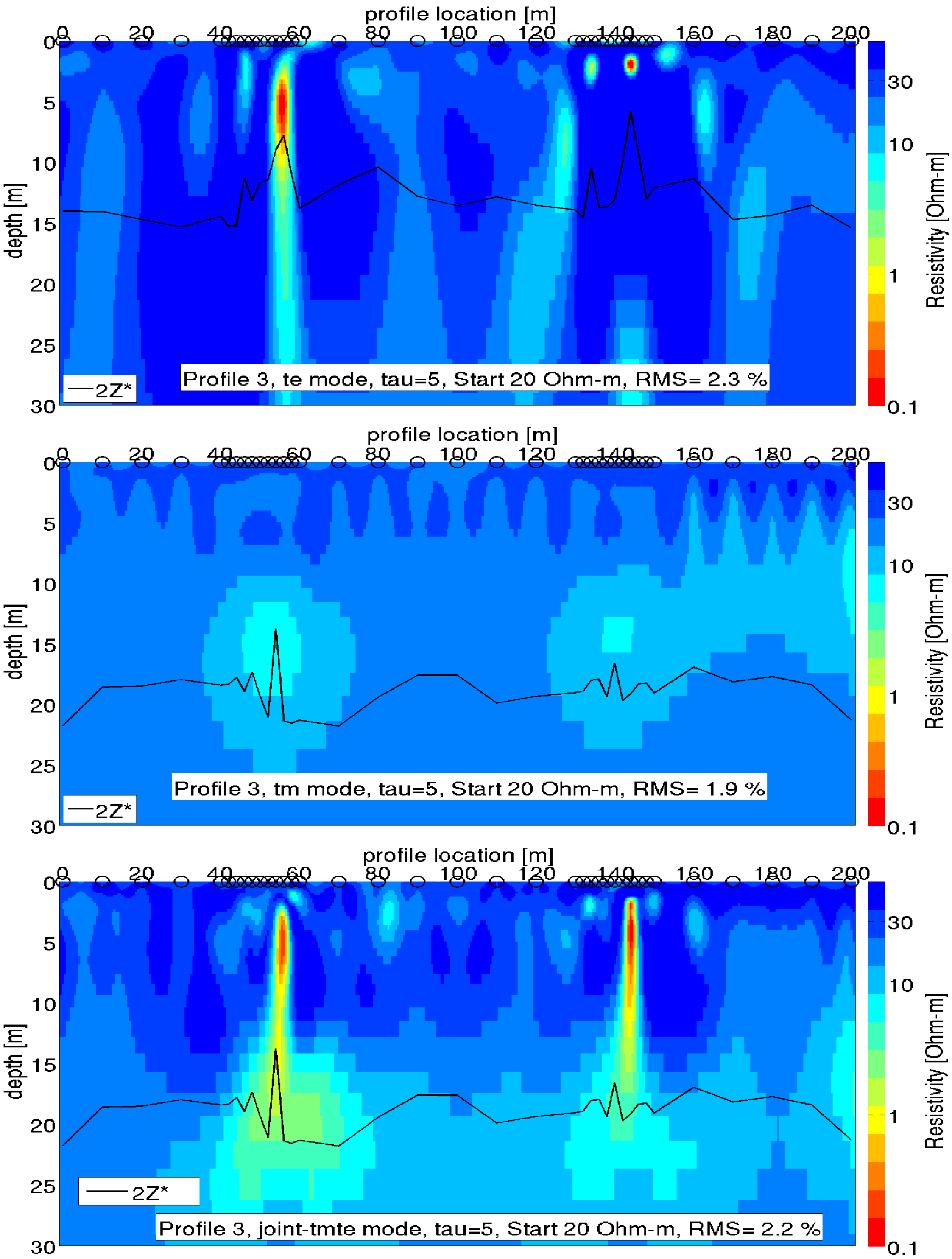

Figure 50: RMT inversion profile 3: TE (top panel), TM (middle panel), and joint inversion (bottom panel) of RMT data. The black circles indicate the sensor positions. Resistivities are given in a logarithmic Ohm-m scale. The penetration depth is indicated with a black line. The RMS values are 2.3 % for the TE-mode, 1.9 % for the TM-mode and 2.2 % for the joint inversion.

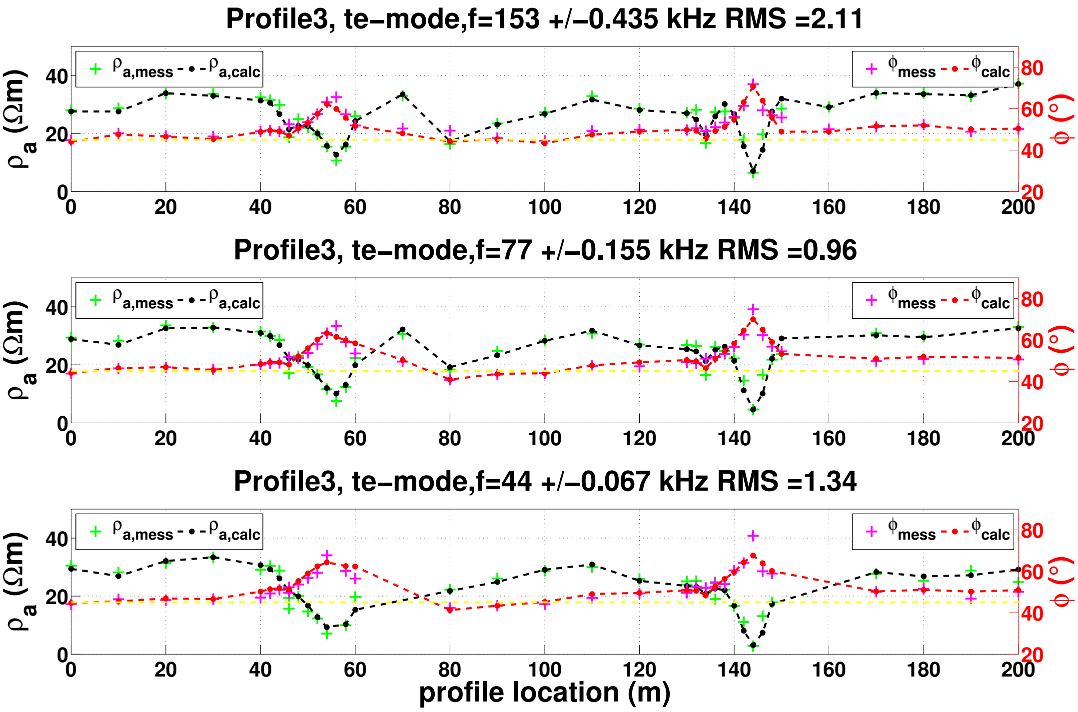

Figure 51: Data fit for profile 3: TE-mode, frequencies 153 kHz (top panel), 77 kHz (middle panel) and 44 kHz (bottom panel). Measured resistivities are shown in green, calculated resistivities in black. Measured phases are shown in magenta, calculated phases in red; the 45 ° line is indicated in yellow.

Figure 52 shows the sensitivity densities of profile 3. The sensitivity densities are calculated after equation (74) [Recher, 2002].

$$S_j = -log_{10}\left[\frac{1}{N}\sum_{i=1}^{N}\left(\frac{A_{ij}}{\Delta\sigma_i}\right)^2\right]^{-\frac{1}{2}} \tag{74}$$

With A the Jacobian (cf. equation(47)) and $\Delta\sigma_i$ the data error. The lower the sensitivity density, the better the resolution of the model parameter. In the TE-mode, the model shows the best resolution at the locations of the anthropogenic anomalies (56 m and 144 m). However, from profile meters 60 – 70 and 140 – 160, the resolution of the model below the anomalies is very low for the TE-mode.

The sensitivity density distribution for the TM-mode and the joint inversion show no unusual features. The resolution decreases with increasing depth and is highest directly below the sensor positions (cf. Figure 52).

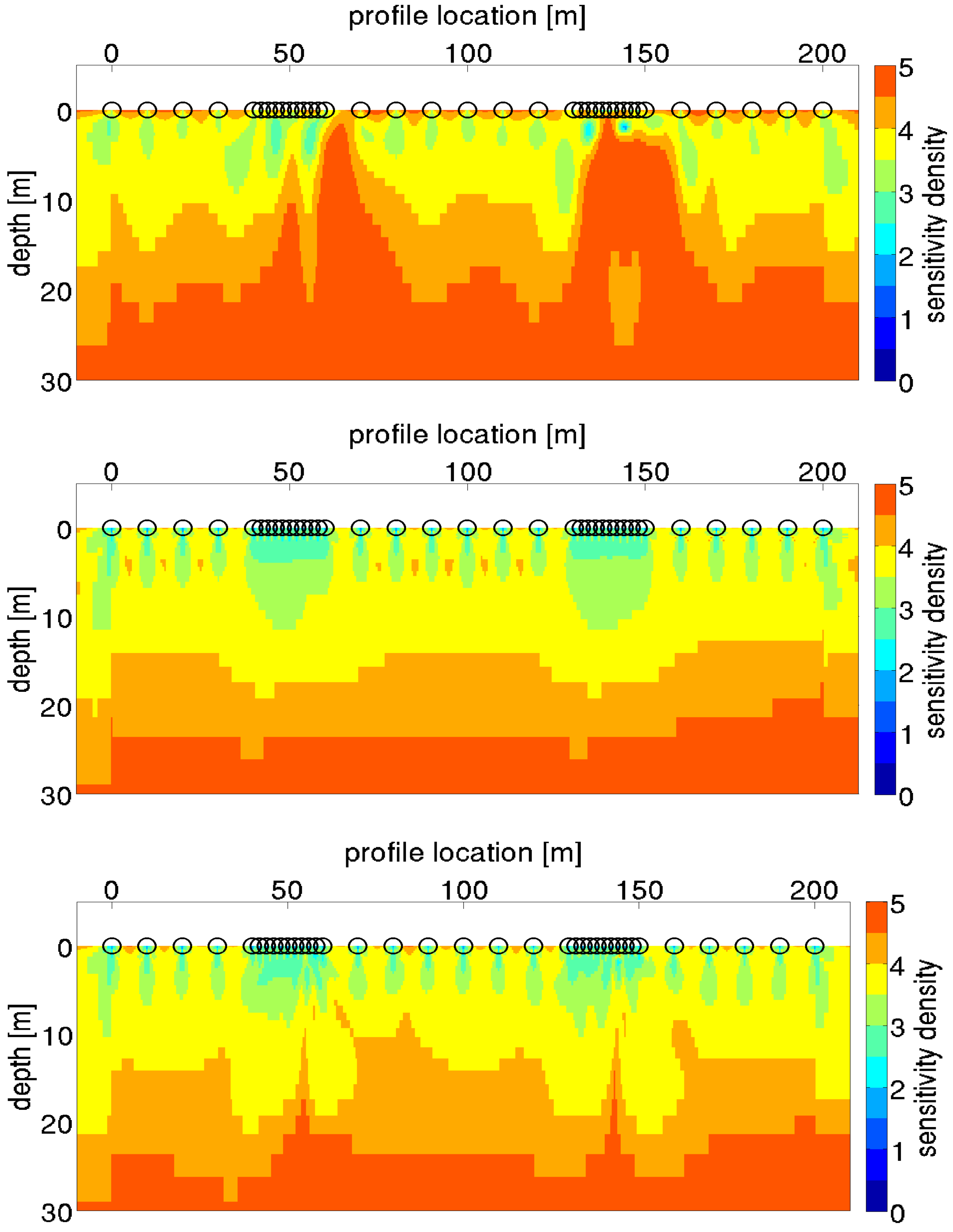

Figure 52: RMT inversion profile 3: Sensitivity densities of TE (top), TM (middle), and joint inversion (bottom) of RMT data. The black circles indicate the sensor positions.

In order to investigate the quality and stability of the inversion results, a forward modelling – obtained via trial and error – is carried out. The a priori information used for the forward modelling is as follows: Firstly, the estimated locations of the conductive anomalies are 60 m and 145 m (cf. Figure 48). Secondly, the cable anomaly is likely to have a very small diameter, maybe just a few cm. Thirdly, the diameter of a gas pipeline is approximately 1 m. Finally, both anomalies are buried in the subsurface. Their exact depth is not known, but since the area is used agriculturally, it is assumed that the anomalies lie more than 1 m deep in the subsurface. These a priori information base on assumptions, but they are reasonable.

The forward model, obtained through variations of the a priory model, with the lowest RMS of 3.96 % is shown in Figure 53. The forward model has a background resistivity of 30 Ohm-m and the modelled anomalies have resistivities of 0.1 Ohm-m, respectively. The pipeline anomaly is located at profile meter 55 in a depth of 2.5 m and has a size of 1 × 1 m^2. The power cable anomaly is located at profile meter 144 in a depth of 3 m and has a size of 2 × 2 m^2.

Figure 54 shows a comparison between measured data and the calculated data of the forward modelling for the same three frequencies as shown in Figure 51. The background resistivities as well as the resistivities at the conductive anomalies are explained well by the data obtained from forward model. The same is true for the phases. The shown frequencies have RMS values from 1.8 % to 2.6 %. The higher RMS value of the whole model stems from higher RMS values of other – not presented – frequencies. However, as expected, the RMS of the forward model is higher than the one of the inversion models. Nevertheless, a forward model that includes a priory information and explains the measured data is found. The horizontal locations of the anomalies obtained by the forward model agree well with the locations of the inversion result. However, the horizontal location of the pipeline deviates from its estimated location of 60 m by approximately 5 m (cf. Figure 48).

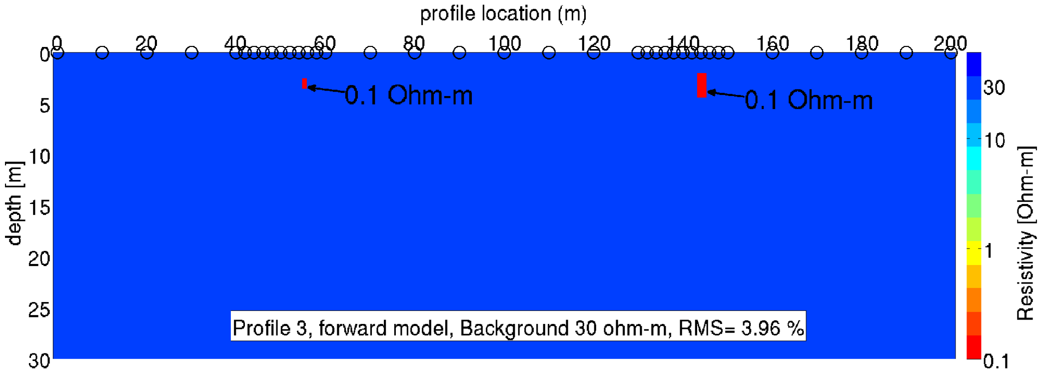

Figure 53: RMT Forward model of profile 3: Resistivities as a function of depth and profile location in a logarithmic Ohm-m scale. High conductive anomalies are located at profile meters 55 and 144. Compared to the measured data the forward model shows an RMS value of 3.96 %.

In order to investigate the stability of the forward solution and to determine how reliable the parameters of the anomalies are, a parameter study is conducted. The results of the study are shown in Table 4. The investigated parameters are background resistivity, anomaly resistivities, anomaly sizes, and horizontal and vertical anomaly positions – compared to the best fit model shown in Figure 53. The table lists the absolute RMS values and for better comparison the relative values in percent. For a better overview, RMS values that differ less than 5 % are marked green, indicating small impact on the data, and values that differ more than 10 % are marked in red, indicating a large impact on the resulting data.

Table 4 shows that a change in the background resistivity of 10 Ohm-m has the largest negative impact in terms of RMS (forward model with 5.76 % RMS). Parameters, which have large impact on the RMS, indicate good resolution of that particular parameter. Other sources of enhanced RMS are: Increasing the resistivity of the anomalies to 1 Ohm-m, reducing the size of the pipeline anomaly to $0.5 \times 0.5\,\mathrm{m}^2$, changing the size of the power cable anomaly by ± 1 m and changing the position of the power cable anomaly by ± 1 m (with the exception of -1 m in horizontal direction). Other changes as, for example, changing the shape of the anomalies to a rectangle or the position of the pipeline anomaly, have small to medium impact on the RMS (forward models with 4 % – 5 % RMS).

Summarizing, the results of the RMT forward modelling parameter study indicate:

- A good resolution of the background resistivity.
- The anomalies are highly conductive.
- The size and shape of the anomalies is not resolved well.
- The position of the pipeline anomaly is less well resolved than the position of the power cable.

Altogether, a subsurface forward model is found in the present study by including a priori information. The found forward model simplifies but explains the subsurface structures well enough and appears to be realistic.

In general, the RMT inversion models of profile 4 and 5 agree with the results of profile 3, only the location of the anomalies along the profile varies. However, in order to be able to compare the results of profile 4 and 5 with the UAS-VLF results of profile 4 and 5, the RMT inversion results are shown in Figure 55 and 56.

The pipeline anomaly is found at 60 m at profile 4 and 70 m at profile 5. The power cable anomaly is found at 147 m at profile 4 and at 148 m at profile 5, respectively. An overview of the anomaly locations is given at the end of Section 6.1 in Table 6. These results agree well (i. e. 1 – 2 m deviation) with the predicted positions of the power cable anomaly and less well (i. e. 2 m – 5 m) with the predicted positions of the pipeline anomaly shown in Section 6.1.1. Reasons for the deviations of the anomaly locations in the map view (cf. Figure 48) and the modelling and inversion results are given at the end of the next section.

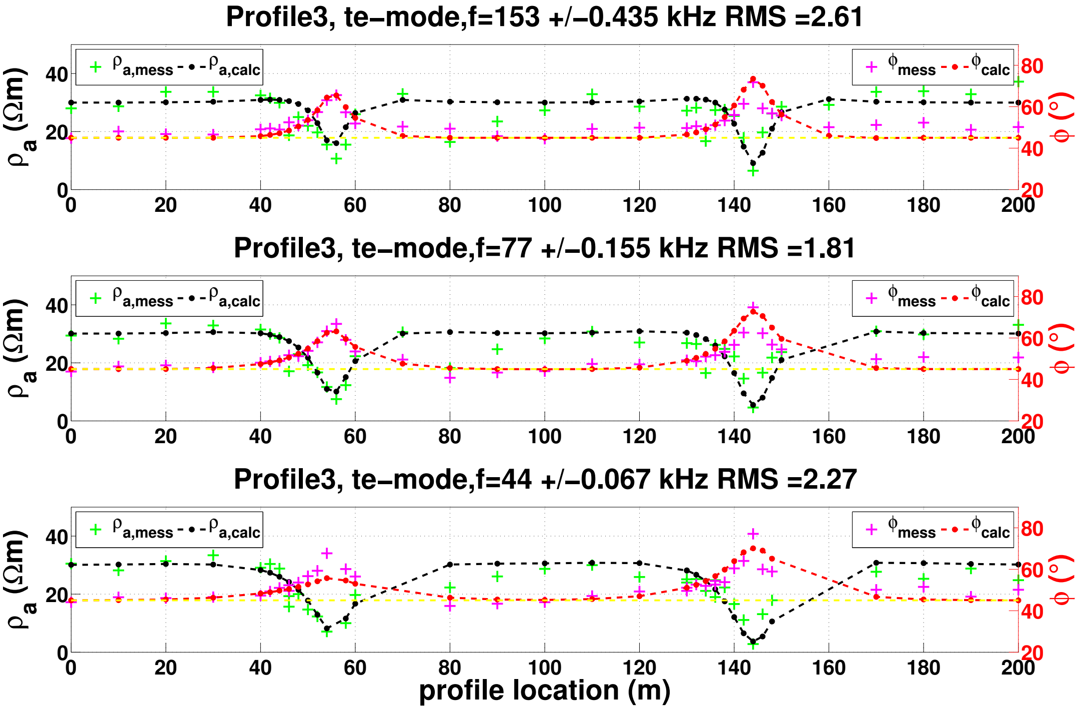

Figure 54: Forward modelled data fit for profile 3: Frequencies 153 kHz, 77 kHz, and 44 kHz. Measured resistivities are shown in green, calculated resistivities in black. Measured phases are shown in magenta, calculated phases in red; the 45° line is indicated in yellow. The background resistivities of 30 Ohm-m as well as the resistivities of the anomalies at profile meters 55 and 144 are well fitted. The same is true for the fit of the phases.

Table 4: RMT forward modelling parameters: Absolute and relative RMS values in %. RMS values that differ by less than 5 % from the reference model are marked green, indicating small data impact and thus bad resolution. RMS values that differ by more than 10 % are marked in red, indicating a high impact and good resolution of the parameter.

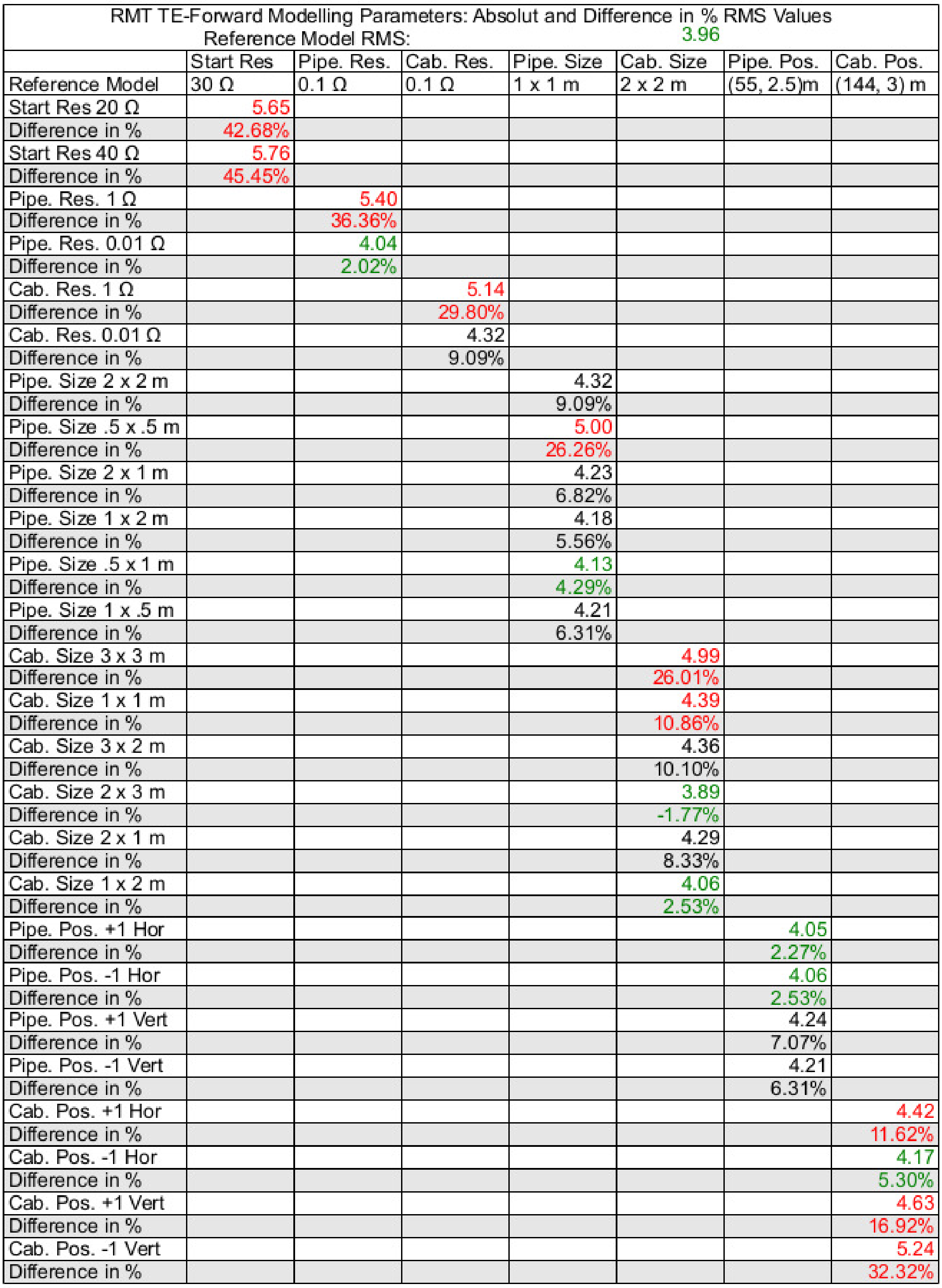

RMT TE-Forward Modelling Parameters: Absolut and Difference in % RMS Values
Reference Model RMS: 3.96

	Start Res	Pipe. Res.	Cab. Res.	Pipe. Size	Cab. Size	Pipe. Pos.	Cab. Pos.
Reference Model	30 Ω	0.1 Ω	0.1 Ω	1 x 1 m	2 x 2 m	(55, 2.5)m	(144, 3) m
Start Res 20 Ω	5.65						
Difference in %	42.68%						
Start Res 40 Ω	5.76						
Difference in %	45.45%						
Pipe. Res. 1 Ω		5.40					
Difference in %		36.36%					
Pipe. Res. 0.01 Ω		4.04					
Difference in %		2.02%					
Cab. Res. 1 Ω			5.14				
Difference in %			29.80%				
Cab. Res. 0.01 Ω			4.32				
Difference in %			9.09%				
Pipe. Size 2 x 2 m				4.32			
Difference in %				9.09%			
Pipe. Size .5 x .5 m				5.00			
Difference in %				26.26%			
Pipe. Size 2 x 1 m				4.23			
Difference in %				6.82%			
Pipe. Size 1 x 2 m				4.18			
Difference in %				5.56%			
Pipe. Size .5 x 1 m				4.13			
Difference in %				4.29%			
Pipe. Size 1 x .5 m				4.21			
Difference in %				6.31%			
Cab. Size 3 x 3 m					4.99		
Difference in %					26.01%		
Cab. Size 1 x 1 m					4.39		
Difference in %					10.86%		
Cab. Size 3 x 2 m					4.36		
Difference in %					10.10%		
Cab. Size 2 x 3 m					3.89		
Difference in %					-1.77%		
Cab. Size 2 x 1 m					4.29		
Difference in %					8.33%		
Cab. Size 1 x 2 m					4.06		
Difference in %					2.53%		
Pipe. Pos. +1 Hor						4.05	
Difference in %						2.27%	
Pipe. Pos. -1 Hor						4.06	
Difference in %						2.53%	
Pipe. Pos. +1 Vert						4.24	
Difference in %						7.07%	
Pipe. Pos. -1 Vert						4.21	
Difference in %						6.31%	
Cab. Pos. +1 Hor							4.42
Difference in %							11.62%
Cab. Pos. -1 Hor							4.17
Difference in %							5.30%
Cab. Pos. +1 Vert							4.63
Difference in %							16.92%
Cab. Pos. -1 Vert							5.24
Difference in %							32.32%

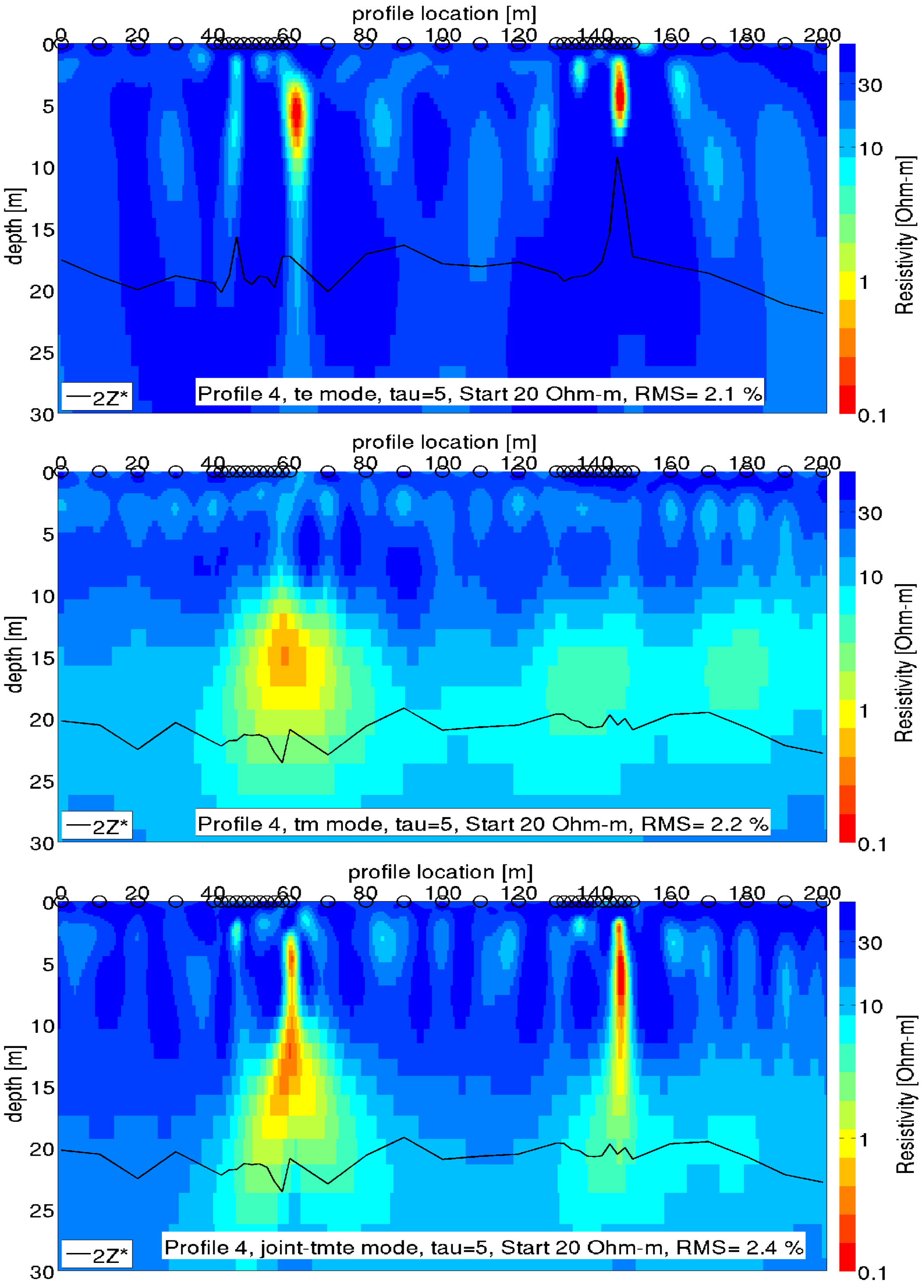

Figure 55: RMT inversion profile 4: TE (top panel), TM (middle panel), and joint inversion (bottom panel) of RMT data. The black circles indicate the sensor positions. Resistivities are given in a logarithmic Ohm-m scale. The penetration depth is indicated with a black line. The RMS values are 2.1 % for the TE-mode, 2.2 % for the TM-mode and 2.4 % for the joint inversion.

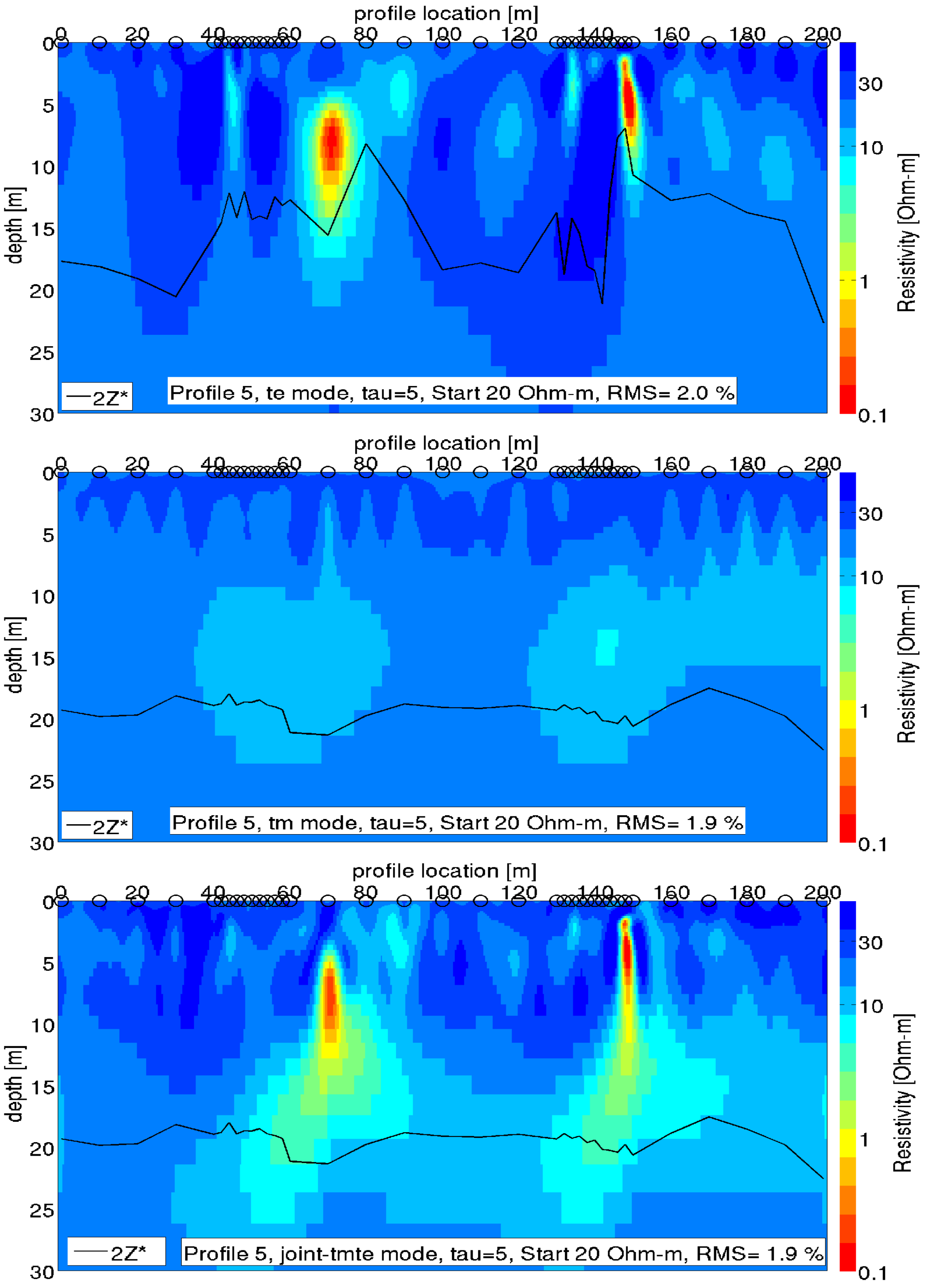

Figure 56: RMT inversion profile 5: TE (top panel), TM (middle panel), and joint inversion (bottom panel) of RMT data. The black circles indicate the sensor positions. Resistivities are given in a logarithmic Ohm-m scale. The penetration depth is indicated with a black line. The RMS values are 2.0 % for the TE-mode, 1.9 % for the TM-mode and 1.9 % for the joint inversion.

6.1.3 VLF

This section discusses the results of UAS-VLF measurements. At first, the UAS-VLF inversion result of profile 3 is shown. Afterwards, the ground-based VLF inversion results of profile 3 are shown and compared. Subsequently, the influence of the height of the sensor and displacement currents in the UAS-VLF inversions is investigated. Finally, a forward modelling and the UAS-VLF results of profile 4 and 5 are presented. The Tipper is determined as described in Section 4.

UAS-VLF Profile 3

The transfer functions and the obtained inversion model of the first UAS-VLF measurement is shown in Figure 57. Depicted is the A part of the transfer function after the described processing described in Section 4. The pipeline is located at profile meter 55 and the power cable at 143 m visible as a zero crossing in the tipper. The pipeline anomaly has minimum/maximum amplitudes of 0.15 and 0.25, while the minimum/maximum amplitudes of the power cable anomaly are smaller, namely 0.1 and 0.15. The course of the transfer function is not completely symmetric around the anomalies, indicating that the Tipper is influenced by other sources than only the cable or pipeline. Bosch and Müller [2005] propose that the effect of one anomaly has not completely decayed at the other anomaly. However, in general, the two anthropogenic anomalies are distinctly visible.

The starting model of the inversion is a homogeneous half space with 30 Ohm-m based on the RMT results. The average height of the sensor during the measurements was 3 m. The resulting model shows two highly conductive anomalies in the order of 0.05 and 0.3 Ohm-m embedded in a 35 Ohm-m half space. To determine the transfer functions, the 18.3 kHz and 23.4 kHz frequencies are used (cf. Figure 80 in the appendix). Other transmitter frequencies are not available or their quality is insufficient (cf. Section 4.3). The used frequencies have a skin depth of approximately 20 m for the resulting inversion model with 35 Ohm-m background resistivity. The air layer has a resistivity of 1×10^{13} Ohm-m in all models. The continuous line in the top panel of Figure 57 shows the calculated model response. With an RMS of 1.39 % (cf. equation (60)), the model shows a good fit (the influence of displacement currents will be investigated on page 97).

Note that, although the transfer functions are determined with more than one frequency (if possible), the VLF modelling and inversion is performed with one frequency only. For all presented results the 23.4 kHz transmitter frequency is used for the inversions. This frequency is chosen because in many cases only the 23.4 kHz frequency is available. Thus, the received models represent a two layer case and especially the depth information of the resistivities needs to be interpreted with caution.

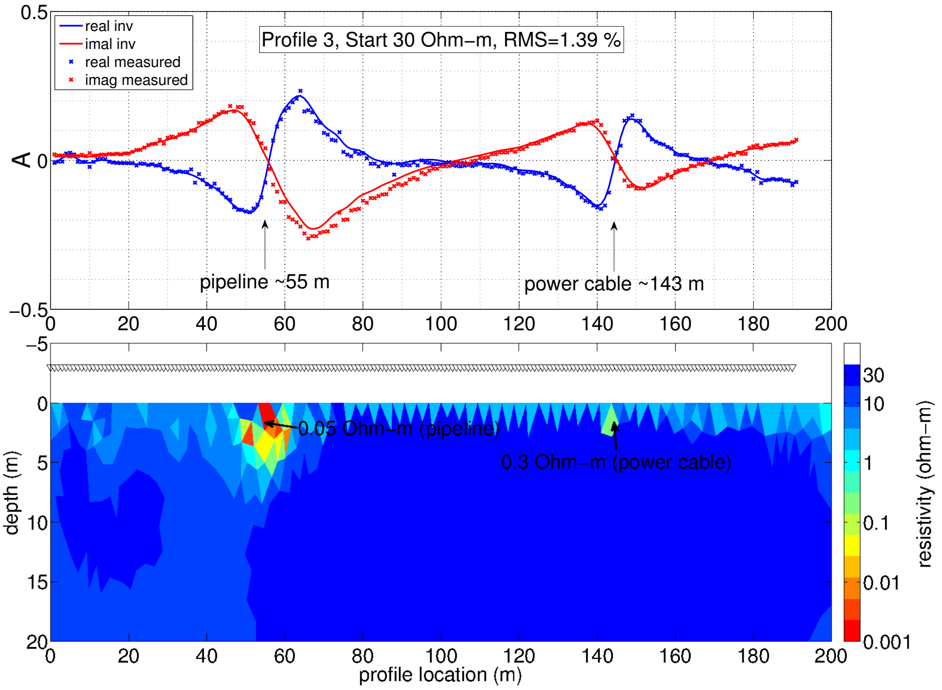

Figure 57: UAS-VLF of profile 3. **Top panel:** Tipper component A, real part in blue and imaginary part in red as a function of profile location. **Bottom panel:** Inversion model. Triangles denote sensor location and height above ground. Resistivities as a function of depth and profile location in a logarithmic Ohm-m scale.

Ground-Based VLF

For comparison to the UAS-VLF data, the ground-based measurement results of the VLF method are presented in Figure 58. In contrast to the UAS-VLF measurements, the transfer functions here are determined with the scalar approach. However, their course is similar to that of the UAS-VLF measurements. As a result, the positions of the anomalies agree well. The pipeline anomaly has a minimum (maximum) amplitude of 0.2 (0.45), while the minimum (maximum) amplitude of the power cable anomaly is larger 0.4 (0.6). The Tipper amplitudes of the ground-based data are larger compared to the UAS-VLF data. This is not surprising since for the ground-based measurements the height of the sensor is 1 m, and thus one would expect a stronger signal from the anomalies. Additionally, the sensor is stationary during the ground-based measurements and is not disturbed by electromagnetic noise of the helicopter. This enables to record less disturbed time series. The resulting model shows two highly conductive anomalies in the order of 3×10^{-4} and 3×10^{-6} Ohm-m embedded in a 35 Ohm-m half space. Again, the lower apparent resistivity values of the anomalies are not surprising, since larger contrasts in the apparent resistivities are necessary to reproduce the larger minima/maxima in the transfer functions. The continuous line shows the model response. However, with an RMS of 10.86 %, the model shows a bad fit.

A better fit with an RMS of 6.13 % is achieved with shifted data – the real part is distinctly shifted (cf. Figure 59). See Section 4.7 for a description of how the shift is realized. In this model, the anomalies are moved 2 m in z-direction. This anomaly position is more realistic than in the inversion results obtained from the unshifted Tipper (cf. Figure 58), because neither the pipeline nor the power cable is connected directly to the surface. That is, the inversion model obtained with the shifted transfer function data seems to match the real conditions better than the inversion model obtained with the unshifted transfer function data. The resistivity value of the anomalies of the shifted model does not change significantly compared to the unshifted model.

UAS-VLF 1 m Sensor Height

In Figure 60 the same transfer function data is used as in Figure 57, but the inversion is carried out with an assumed height of the sensor of 1 m. The influence of the height of the sensor on the obtained inversion model is investigated and a comparison with the model obtained with ground-based VLF is made, since the height of the sensor of the ground-based measurements is 1 m, too. The apparent resistivity values of the anomalies are of the same magnitude, as for the inversion with 3 m height of the sensor (0.05 and 0.3 Ohm-m), but higher (0.05 and 0.5 Ohm-m). The reason is that the transfer functions of an anomaly with a low resistivity contrast, but measured close to the ground, are similar to the transfer functions of an anomaly with high resistivity contrast, but measured from a large altitude. If only the height of the sensor is changed but the amplitudes of the transfer functions remain the same, a smaller resistivity contrast is sufficient to reproduce the measured transfer functions.

Compared to the inversion model obtained with the ground-based VLF measurement (4×10^{-5} and 1×10^{-5} Ohm-m), the resistivity values are not of the same magnitude; they are much higher (0.05 and 0.5 Ohm-m). This is because, only the height of the sensor is changed but the amplitudes of the transfer functions remain the same. Thus, a smaller resistivity contrast is sufficient to reproduce the measured transfer functions. Additionally, the vertical position, structure, and composition of the anomalies differ slightly. In general, the differences in the obtained inversion model with 1 m height of the sensor are small compared to the inversion model with 3 m sensor height. Concluding, the height of the sensor in the inversion of UAS-VLF data appears to have a small influence on the obtained inversion model.

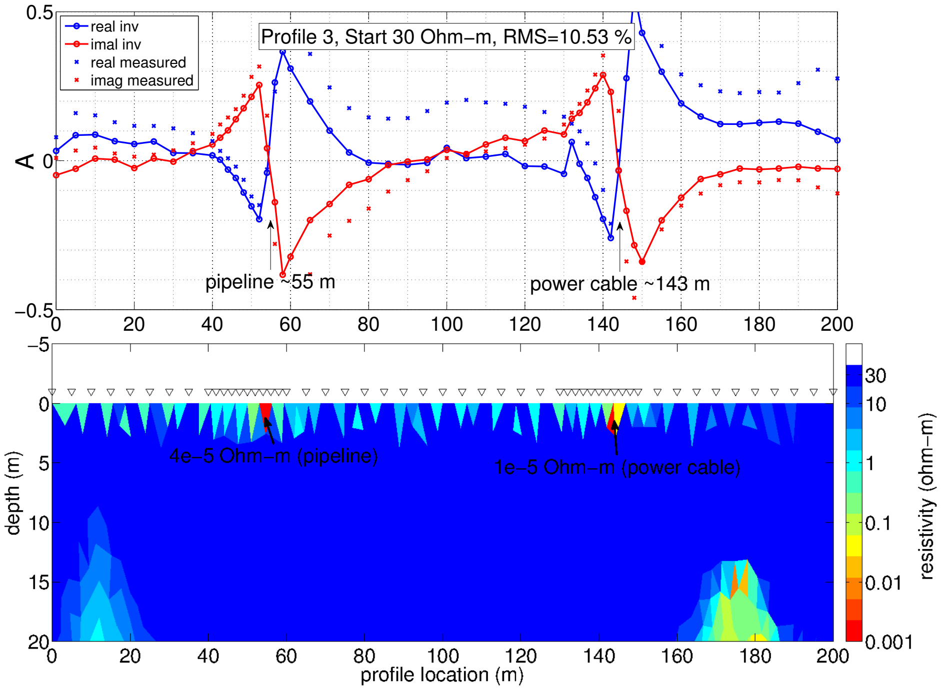

Figure 58: Ground-based VLF of profile 3. **Top panel:** Tipper component A, real part in blue and imaginary part in red as a function of profile location. **Bottom panel:** Inversion model. Triangles denote sensor location and height above ground. Resistivities as a function of depth and profile location in a logarithmic Ohm-m scale.

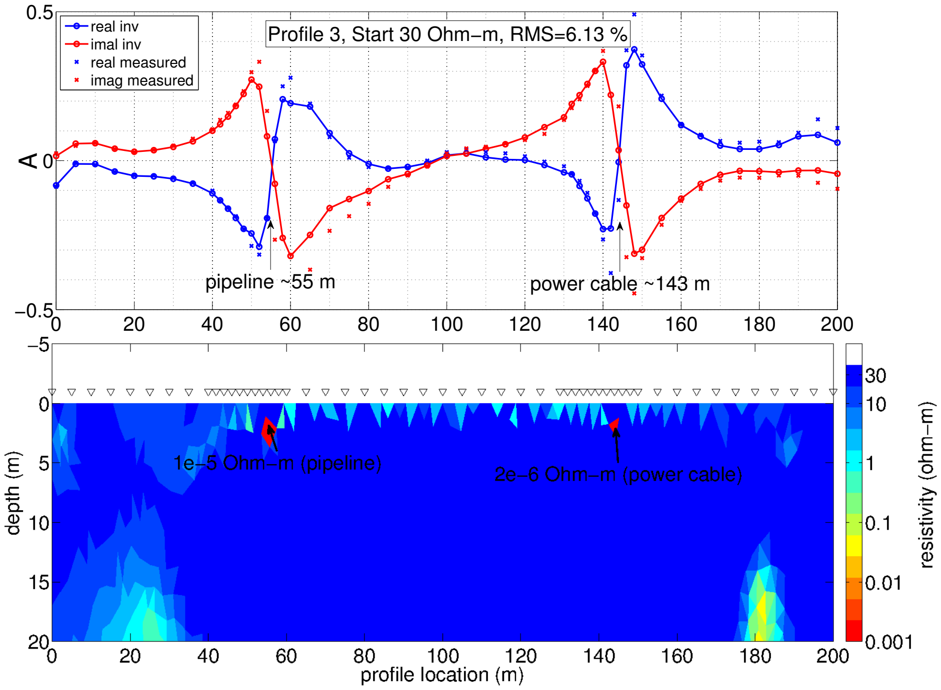

Figure 59: Ground-based VLF of profile 3, Tipper shifted. **Top panel:** Tipper component A, real part in blue and imaginary part in red as a function of profile location. **Bottom panel:** Inversion model. Triangles denote sensor location and height above ground. Resistivities as a function of depth and profile location in a logarithmic Ohm-m scale.

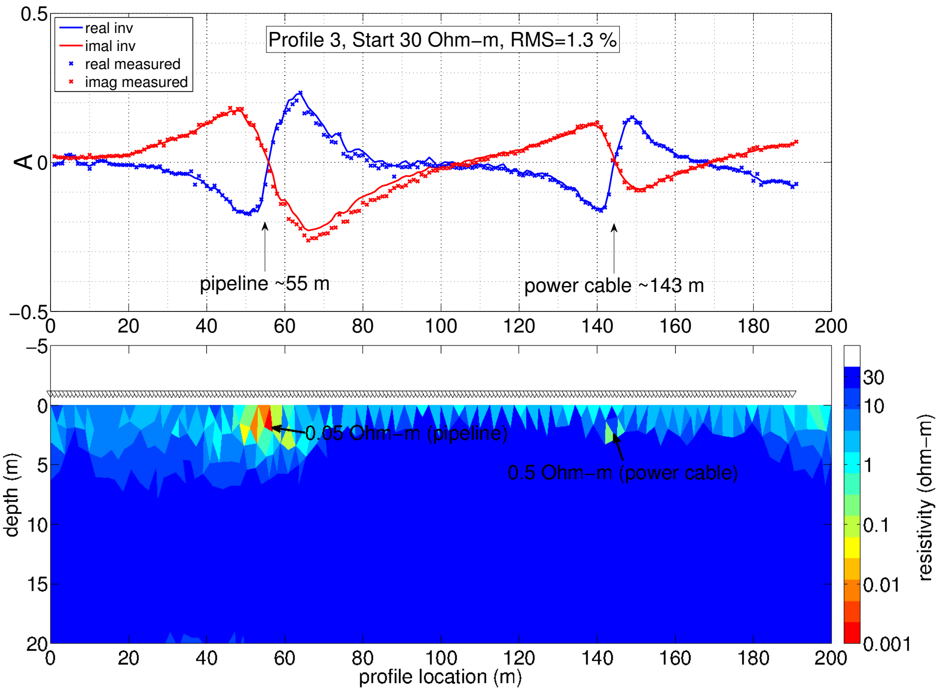

Figure 60: UAS-VLF of profile 3, sensor height 1 m. **Top panel:** Tipper component A, real part in blue and imaginary part in red as a function of profile location. **Bottom panel:** Inversion model. Triangles denote sensor location and height above ground. Resistivities as a function of depth and profile location in a logarithmic Ohm-m scale.

UAS-VLF Displacement Currents Neglected

Another study is presented in Figure 61. Again, the same transfer function data is used as in Figure 57, but to investigate the influence of displacement currents, they are neglected for this inversion. The resistivity values of the pipeline anomaly are of the same order of magnitude (0.15 Ohm-m) as in the model in Figure 57 (0.3 Ohm-m), whereas the resistivity values of the power cable anomaly are not of the same order of magnitude (0.001 Ohm-m) as in the model in Figure 57 (0.05 Ohm-m). The form and composition of the anomalies differ slightly. Altogether, the differences between model with or without displacement currents included, are small. Thus, it is not crucial to involve or neglect displacement currents in the inversions for a 3 m thick air layer. In the present thesis, displacement currents are included in the inversion nevertheless, because of the bad conducting (resistivity 1×10^{13} Ohm-m) and 3 m thick air layer. However, no significant computation time difference or other negative effects result, from the inclusion of displacement currents.

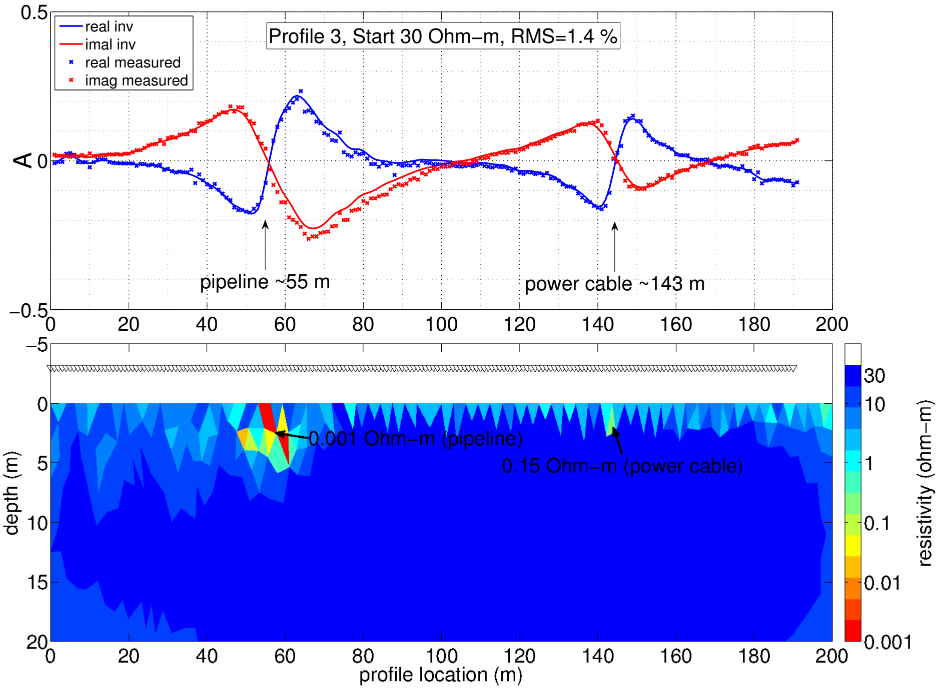

Figure 61: UAS-VLF of profile 3, displacement currents are neglected. **Top panel:** Tipper component A, real part in blue and imaginary part in red as a function of profile location. **Bottom panel:** Inversion model. Triangles denote sensor location and height above ground. Resistivities as a function of depth and profile location in a logarithmic Ohm-m scale.

UAS-VLF Forward Model

Figure 62 shows the result of a forward model obtained via trial and error. The used a priory information is identical to the RMT forward model study in the section above. The RMS of the obtained model is 3.69 %. The position of the pipeline with a resistivity value of 1×10^{-5} Ohm-m is at 55 m in 3 m depth. The position of the power cable with a resistivity value of 0.1 Ohm-m is at 143 m in 5 m depth. The dimension of both anomalies is 2×2 m. As for RMT in the previous section, the stability of the obtained model is investigated and the results are presented in table 5. The investigated parameters are background resistivity, anomaly resistivities, anomaly sizes, and horizontal and vertical anomaly positions – compared to the best fit model shown in Figure 62. The table lists the absolute RMS values and for better comparison the relative values in percent. Table 5 shows that a change in background resistivity of 10 Ohm-m has a large negative impact on the RMS of the forward model (forward models with 4.09 % and 4.11 % RMS). Other sources of enhanced RMS are: (a) Increasing the power cable resistivity to 1 Ohm-m and (b) reducing the vertical position of the pipeline anomaly by 1 m. Other changes have a small to medium impact on the RMS. If a parameters has a large impact on the RMS this indicates that this parameter is well resolved. Compared to RMT, the VLF results indicate a worse resolution of the investigated parameters. However, for both methods the background resistivity values are crucial to obtain a low RMS. Note that the position along the profile is identical for the obtained inversion models as well as for the forward model with the lowest RMS.

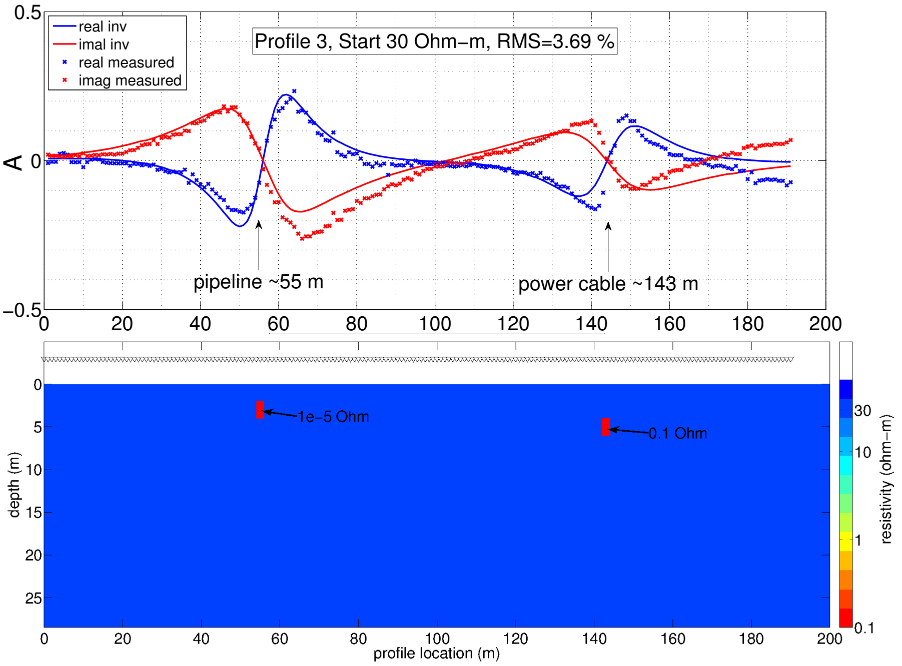

Figure 62: UAS-VLF forward model of profile 3. **Top panel:** Tipper component A, real part in blue and imaginary part in red as a function of profile location. **Bottom panel:** Forward model: Triangles denote sensor location and height above ground. Resistivities as a function of depth and profile location in a logarithmic Ohm-m scale.

Table 5: VLF forward modelling parameters: Absolute and relative RMS values in %. RMS values that differ by less than 5 % from the comparison model are marked green, indicating small data impact and thus bad resolution. RMS values that differ by more than 10 % are marked in red, indicating a high impact and good resolution on the resulting data.

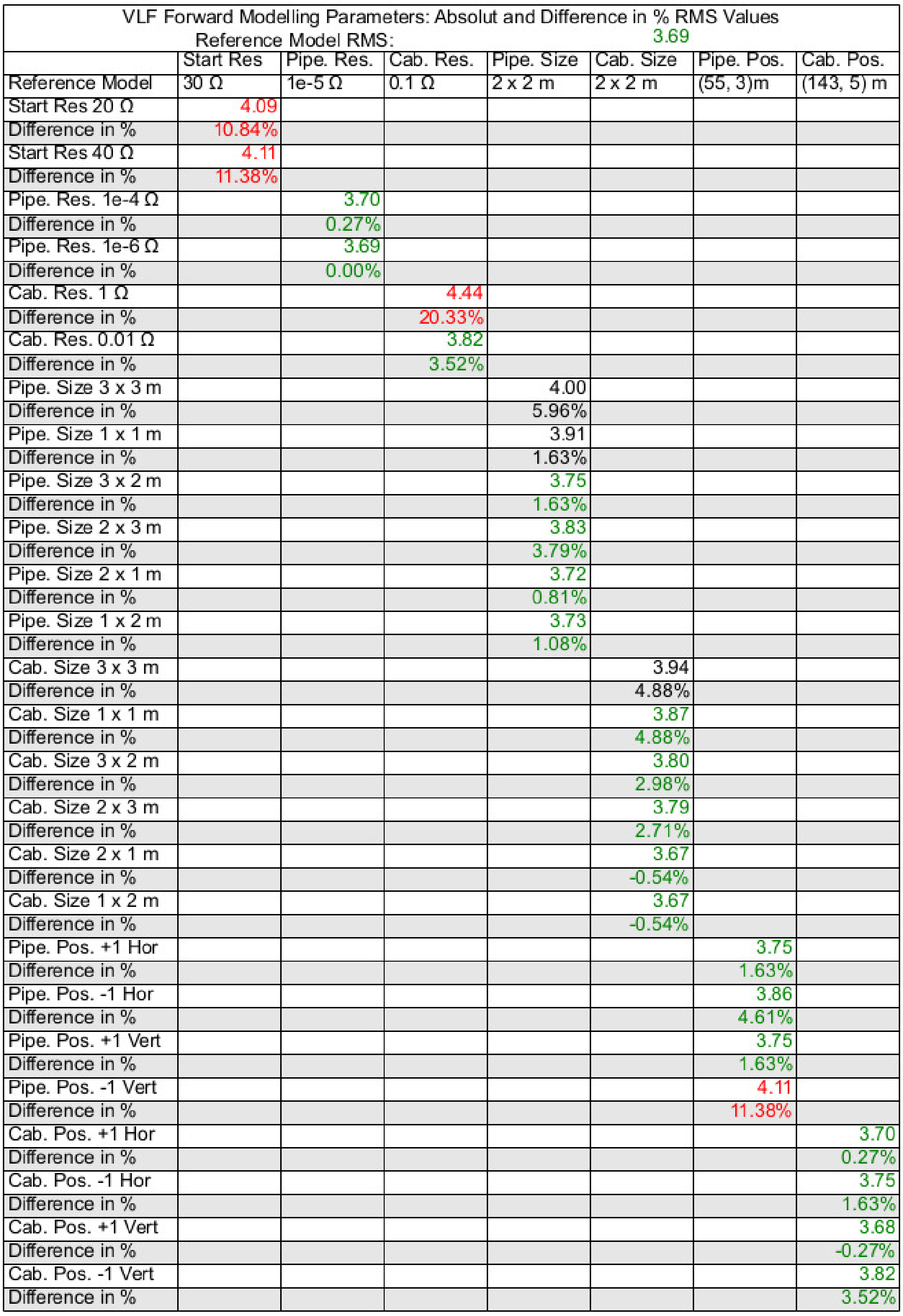

VLF Forward Modelling Parameters: Absolut and Difference in % RMS Values

Reference Model RMS: 3.69

	Start Res	Pipe. Res.	Cab. Res.	Pipe. Size	Cab. Size	Pipe. Pos.	Cab. Pos.
Reference Model	30 Ω	1e-5 Ω	0.1 Ω	2 x 2 m	2 x 2 m	(55, 3)m	(143, 5) m
Start Res 20 Ω	4.09						
Difference in %	10.84%						
Start Res 40 Ω	4.11						
Difference in %	11.38%						
Pipe. Res. 1e-4 Ω		3.70					
Difference in %		0.27%					
Pipe. Res. 1e-6 Ω		3.69					
Difference in %		0.00%					
Cab. Res. 1 Ω			4.44				
Difference in %			20.33%				
Cab. Res. 0.01 Ω			3.82				
Difference in %			3.52%				
Pipe. Size 3 x 3 m				4.00			
Difference in %				5.96%			
Pipe. Size 1 x 1 m				3.91			
Difference in %				1.63%			
Pipe. Size 3 x 2 m				3.75			
Difference in %				1.63%			
Pipe. Size 2 x 3 m				3.83			
Difference in %				3.79%			
Pipe. Size 2 x 1 m				3.72			
Difference in %				0.81%			
Pipe. Size 1 x 2 m				3.73			
Difference in %				1.08%			
Cab. Size 3 x 3 m					3.94		
Difference in %					4.88%		
Cab. Size 1 x 1 m					3.87		
Difference in %					4.88%		
Cab. Size 3 x 2 m					3.80		
Difference in %					2.98%		
Cab. Size 2 x 3 m					3.79		
Difference in %					2.71%		
Cab. Size 2 x 1 m					3.67		
Difference in %					-0.54%		
Cab. Size 1 x 2 m					3.67		
Difference in %					-0.54%		
Pipe. Pos. +1 Hor						3.75	
Difference in %						1.63%	
Pipe. Pos. -1 Hor						3.86	
Difference in %						4.61%	
Pipe. Pos. +1 Vert						3.75	
Difference in %						1.63%	
Pipe. Pos. -1 Vert						4.11	
Difference in %						11.38%	
Cab. Pos. +1 Hor							3.70
Difference in %							0.27%
Cab. Pos. -1 Hor							3.75
Difference in %							1.63%
Cab. Pos. +1 Vert							3.68
Difference in %							-0.27%
Cab. Pos. -1 Vert							3.82
Difference in %							3.52%

UAS-VLF Profile 4 and 5

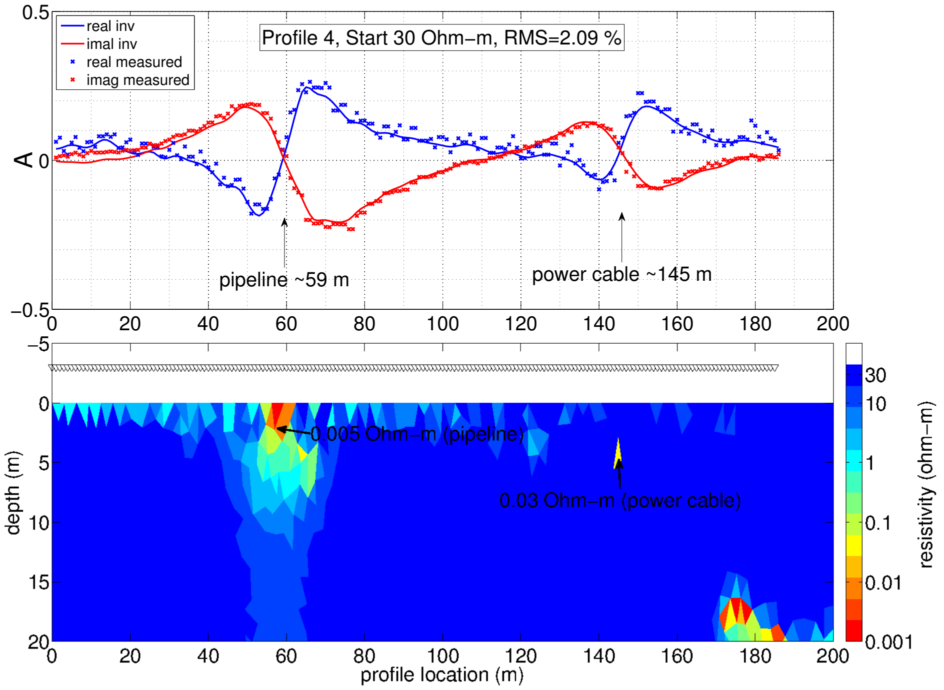

Figure 63: UAS-VLF of profile 4. **Top panel:** Tipper component A, real part in blue and imaginary part in red as a function of profile location. **Bottom panel:** Inversion model. Triangles denote sensor location and height above ground. Resistivities as a function of depth and profile location in a logarithmic Ohm-m scale. Anomalies at profile meters 59 and 145.

Figures 63 and 64 show the measured UAS-VLF data and the obtained inversion models of profiles 4 and 5. To determine the transfer functions, the 18.3 kHz, 20.9 kHz, and 23.4 kHz frequencies are used (cf. Figures 81 and 82 in the appendix). The general results of the inversion models agree well with the model of profile 3. As expected, the position of the anomalies are shifted along the profile (see Section 6.1.1).

It is noticeable that the pipeline anomaly has a larger volume than the power cable in all inversion models. This appears reasonable, considering that the pipeline has probably a larger cross section than the cable. The vertical position of the power cable anomaly in Figures 63 and 64 of approximately 5 m is quasi identical. In Figure 57, the inversion results show shallow anomalies. The depth of the power cable anomaly for profile 4 and 5 is closer to the forward model than the anomaly position of profile 3 in Figure 62. Despite the larger RMS of the models in Figures 63 and 64 compared to Figure 57, they seem more realistic because the cable is buried in the subsurface. Thus, the exact depth is not known. The results from the shifted ground-based data (cf. Figure 59) confirm this result. Another feature of the forward model is that the pipeline anomaly is located less deep than the cable anomaly. This is reproduced with the UAS-VLF models of profile 4 and 5 but not with the model of profile 3.

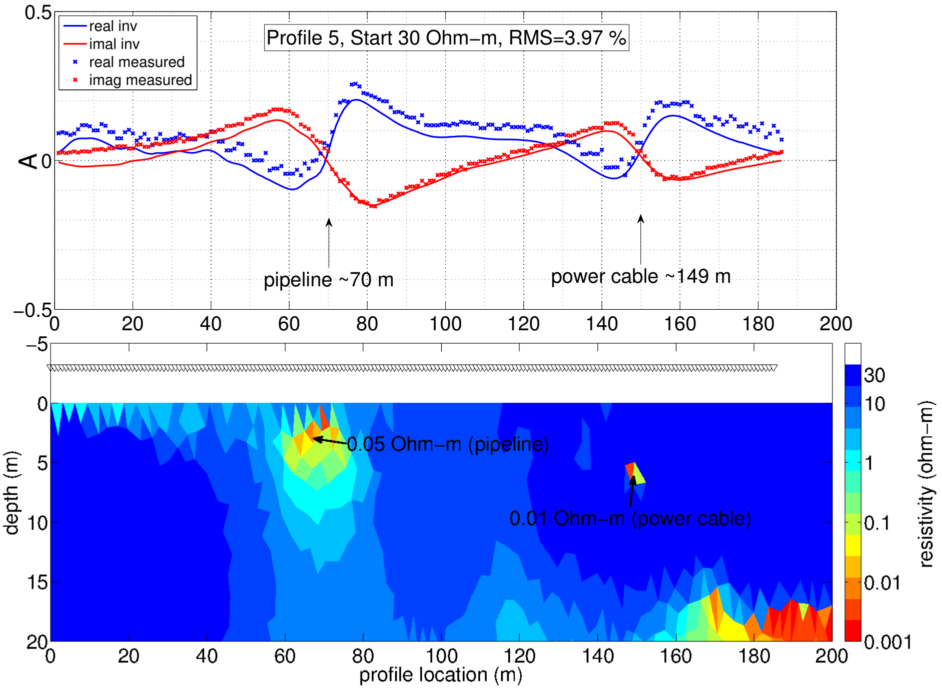

Figure 64: UAS-VLF of profile 5: **Top panel:** Tipper component A, real part in blue and imaginary part in red as a function of profile location. **Bottom panel:** Inversion model. Triangles denote sensor location and height above ground. Resistivities as a function of depth and profile location in a logarithmic Ohm-m scale.

Summary of the Anomaly Positions

A summary of the identified locations of the anomalies based on RMT and VLF measurements is given in Table 6. The locations agree well or differ only by 1 m (with exception of the power cable in profile 4). The deviations of the anomaly locations in the map view (cf. Figure 48) and the modelling and inversion results may have the following reasons: Firstly, during the field measurements, GPS coordinates (accuracy approximately 2 m) are taken at profile meter 0 and these coordinates are used to determine profile meter 0 in the map view. However, the coordinates seem to have a systematic error, since adding 2 m to the anomaly positions of the modelling and inversion results decreases the deviations. Secondly, in the map view the course pipeline anomaly shows a bend between profile 1 and 2. The location of this bend is determined by taking the GPS coordinate of a surface marker during field measurements. However, if the bending point of the pipeline is moved between profile 2 and 3, the location of the pipeline anomaly determined by modelling and inversion would agree well with the map view.

Table 6: Positions of the Anomalies

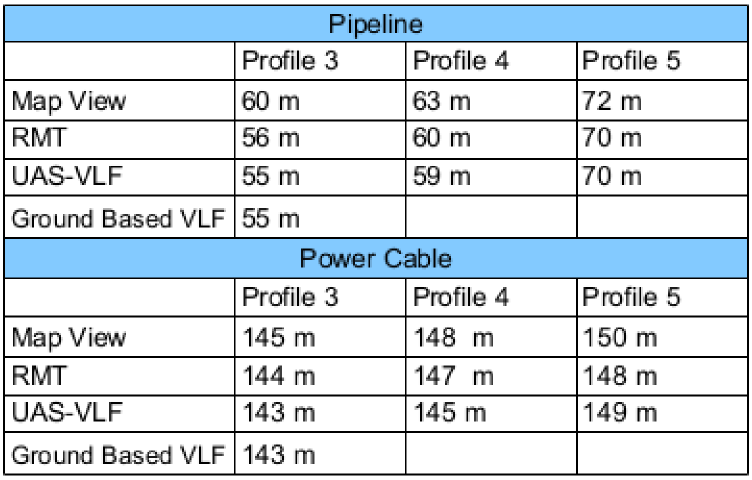

Pipeline			
	Profile 3	Profile 4	Profile 5
Map View	60 m	63 m	72 m
RMT	56 m	60 m	70 m
UAS-VLF	55 m	59 m	70 m
Ground Based VLF	55 m		
Power Cable			
	Profile 3	Profile 4	Profile 5
Map View	145 m	148 m	150 m
RMT	144 m	147 m	148 m
UAS-VLF	143 m	145 m	149 m
Ground Based VLF	143 m		

Discussion of the Wavre Results

The most important conclusion from the first measurement site is that it is possible to detect (anthropogenic) anomalies with the UAS-VLF method. Furthermore, the horizontal positions of the detected anomalies agree well with the RMT results of the previous section as well as with the ground-based VLF measurements which served as a reference. The UAS-VLF results are not in good agreement with positions seen in the survey area map, but this is probably caused by errors in the GPS coordinates used to determine the positions in Figure 48. However, if 2 m are subtracted of the profile locations of the anomalies in the map view, the deviation in the anomaly locations compared to the measurement results is small. This indicates a systematic error in the start position of the profiles drawn in Figure 48. Taking this systematic errors into account the one can state that the UAS-VLF method is well-suited for determining lateral locations of subsurface anomalies.

Furthermore, it is possible to obtain resistivity models of the subsurface with the UAS-VLF method that are comparable to those obtained from the RMT method. But, prior to the inversion, a background resistivity has to be included. Additionally, the resolution of the parameters (resistivities, anomaly positions, etc.) of the VLF models is coarser than the resolution from the RMT models. The results of the RMT inversions indicate depths of 2 m and 3 m, with either both anomalies in the same depth or a deeper pipeline anomaly, whereas for the UAS-VLF inversion results the depth of the anomalies vary from 0 m to more than 5 m, with the cable anomaly located deeper. The forward modelling studies indicate that the depth and size information is not reliable, but the position of the along the profile are resolved well.

Finally, including or neglecting displacement currents does not have a large impact on the inversion models; it is possible to receive a good fit of the transfer functions and a similar inversion result with sensor heights of 1 m and of 3 m. This indicates that the height of the sensor can be neglected in the inversion.

6.2 Cuxhaven

After the successful measurements in Switzerland, the survey area near Cuxhaven is chosen to investigate the feasibility of the UAS-VLF method to detect a natural geophysical feature (cf. Figure 65). Previous airborne EM-measurements of the *Federal Institute for Geosciences and Natural Resources* (cf. Figure 66 and 67 in Section 6.2.1) indicate a transition from salt to freshwater in the survey area. In this section, the survey area in Cuxhaven is introduced and RMT, ground-based VLF, and UAS-VLF data and the respective modelling and inversion results are presented and compared. The aim is to obtain subsurface resistivity models that agree well with the a priory information from BURVAL [2003]. From the comparison with BURVAL [2003], the feasibility of the UAS-VLF method for obtaining realistic subsurface resistivity models is investigated. During the campaign near Cuxhaven, solely the 23.4 kHz transmitter is received, so that the evaluation of the data of RMT as well as VLF is based on this frequency alone. That is the modelling and inversion in this section is performed with one frequency for all presented results. Thus, the received models represent a two layer case and especially the depth information of the apparent resistivities needs to be interpreted with caution. The appropriated skin depths in the survey area for the 23.4 kHz frequency range from 7 m for a 5 Ohm-m half space to 18 m for a 30 Ohm-m half space

6.2.1 Survey Area

The second UAS-VLF measurements were carried out in October 2012 near Cuxhaven, northern Germany. This test area includes a natural anomaly: a transition zone from salt- to freshwater (cf. Figure 65). In total, four parallel profiles A – D are investigated with the UAS-VLF and RMT method. Additionally, profile A and D are investigated with ground-based fixed-frame VLF.

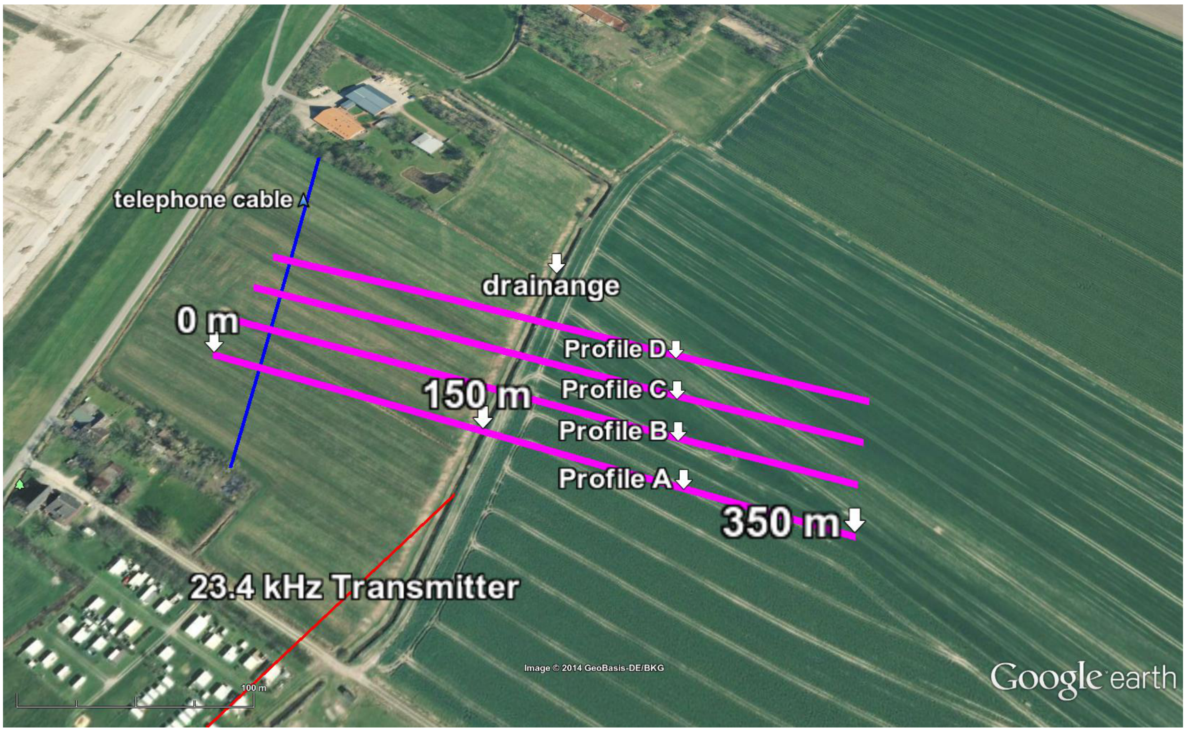

Figure 65: Survey area near Cuxhaven, Germany. The profiles – from bottom to top A, B, C, D – are plotted in purple. A telephone cable is plotted in blue. At profile meter 150 a drainage crosses the profiles. Transmitter direction is indicated in red [Google-earth, 2008].

The exact location of the site is chosen following a resistivity map and profile of airborne electromagnetic data from the Bremerhaven-Cuxhavener Rinne survey (cf. Figure 66 and 67) [BURVAL, 2003]. The basis for the decision is that the lateral contrast in the resistivities along a profile is as large as possible. A large lateral conductivity contrast has a strong effect on the transfer functions. A strong effect on the transfer functions is desirable to test the feasibility of UAS-VLF measurements.

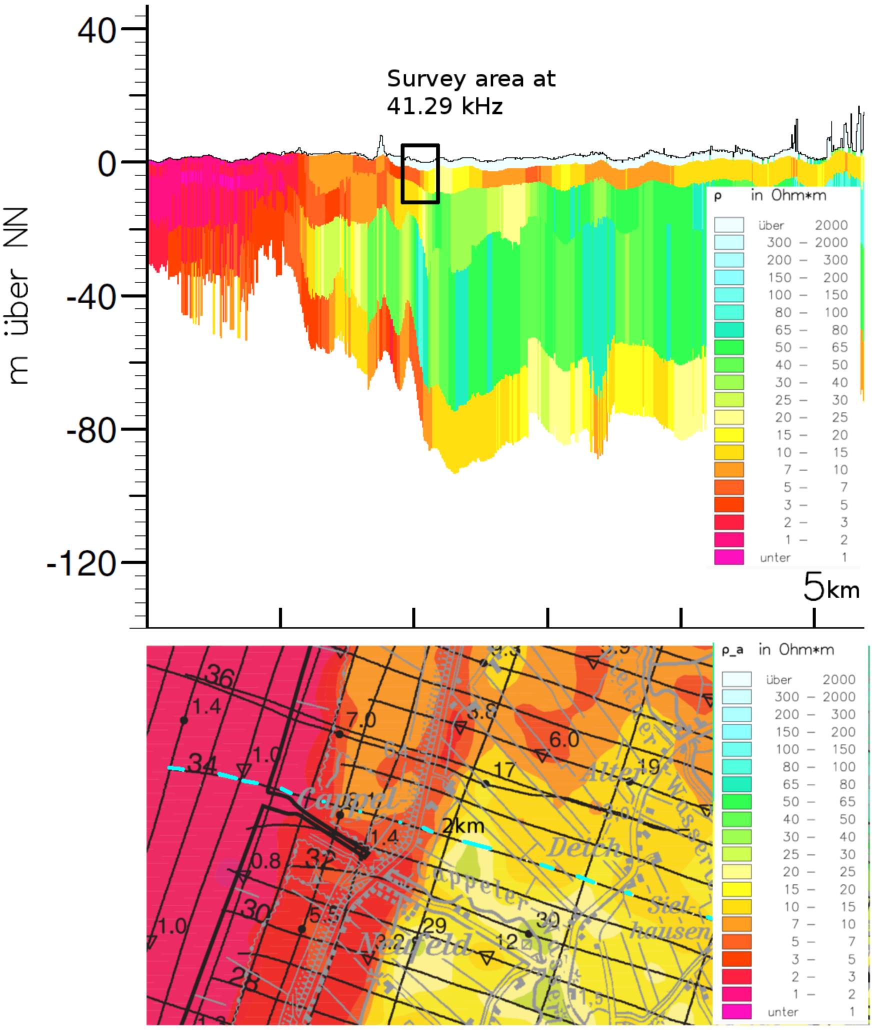

Figure 66: **Top:** Multiple layer inversion of profile 34 along a 5 km section. The Bremerhaven-Cuxhavener Rinne survey was carried out using different frequencies (0.4 kHz, 1.8 kHz, 8.6 kHz, 41.3 kHz (and 193 kHz, not included here)) leading to different investigation depths. For its vicinity to VLF frequencies, the determination of the survey area is oriented on the frequency 41.3 kHz, the one with the lowest depth of investigation in this image. The survey area is marked with a black rectangle (modified after BURVAL [2003]).

Bottom: Apparent resistivity map (frequency = 41.3 kHz) of the measurement site near Cuxhaven, Germany. Derived from airborne electromagnetic data from the Bremerhaven-Cuxhavener Rinne survey. 5 km of profile 34 is marked with blue dashes. The survey area is located at about 2 km (modified after BURVAL [2003]).

Figure 67: Zoom of Figure 66. The survey area is marked blue. Apparent resistivity map (frequency = 41.3 kHz), of the area near Cuxhaven, Germany. Derived from airborne electromagnetic data from the Bremerhaven-Cuxhavener Rinne survey (modified after BURVAL [2003]).

Although the apparent resistivity map is used as a general indicator for a suitable survey area, it is not exact enough because it is interpolated to 2D. To be sure that the location is suitable for a UAS-VLF field campaign, the profile sections are used to determine the applicability of the survey area. Note the differences in resistivity along profile 34 in the top of Figure 66 and the marked area in Figure 66.

6.2.2 RMT

The results of the RMT measurements are shown in Figure 68. The apparent resistivity data show a decrease at profile meter 15 due to a telephone cable. Generally, the apparent resistivity remains at 10 to 15 Ohm-m until profile meter 150. Then it decreases slightly below 10 Ohm-m until profile meter 175, where it starts to increase to almost 40 Ohm-m at profile meter 250. This confirms the BGR data of BURVAL [2003] and indicates the assumed salt- to freshwater transition at approximately profile meters 150 to 175. The shown phase information indicates the telephone cable anomaly at profile meter 15. Note that due to bad weather, the distance between the measuring points is increased to 50 m for the last 150 profile meters.

Additionally, Figure 68 shows the inversion result of the measured data (bottom panel). The model indicates the telephone cable and shows low resistivities until profile meter 150. The resistivity drops even lower around profile meters 150 to 175 at depths of 5 to 10 meters, thus confirming the previous conclusions.

These results are remarkable, since a drainage filled with water crosses the profile from profile meters 150 to 155 and one would expect a low resistive anomaly at this location. Or one could expect that the drainage serves as border for the salt to freshwater saturated zones. However, a low resistive anomaly is extended up to profile meter 175 and the subsurface resistivity stays low until profile meter 205. Because of the large gaps between the RMT stations beginning from profile meter 200, the results should be interpreted with caution. It is not possible to determine the nature of this extended anomaly from the data. It may be salt water intrusion as expected for profile meters 0 – 150, where the resistivity values are similar. However, it could also be soil saturated with freshwater. The origin of the saturation could be dammed up and accumulated water in front of the drainage (profile meters 155 to 200). However, this is speculation. Other reasons for the extended anomaly might be possible.

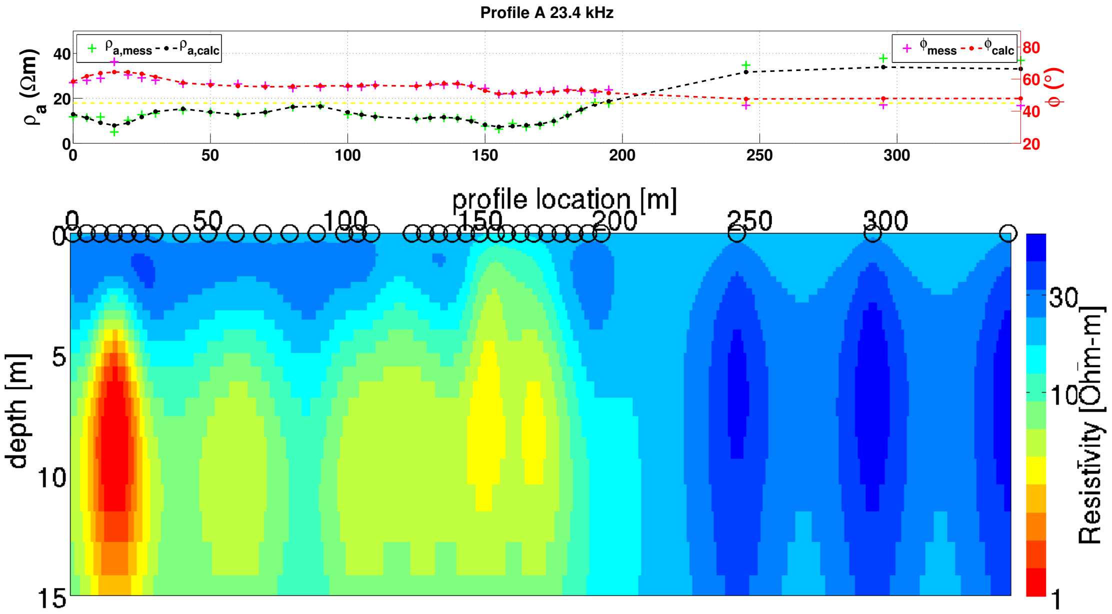

Figure 68: Top panel: Apparent resistivity and phase of profile A. **Bottom panel:** RMT inversion profile A, TE-mode. Resistivities as a function of depth and profile location in a logarithmic Ohm-m scale. The inversion model explains the data well with an RMS of 1.9 %. High conductive anomaly at profile meter 15. Drainage at profile meters 150 to 155. Low resistive subsurface left of the drainage and higher resistive subsurface right of it.

6.2.3 VLF

The four profiles A – D covered by the VLF measurements are presented in this section (cf. Section 6.2.1). The results of the UAS-VLF measurements are discussed and ground-based VLF measurements are compared to UAS-VLF measurements. In order to determine the transfer functions, the 23.4 kHz frequency is used solely (cf. Figure 80 in the appendix).

Profile A

Figure 69 shows the UAS-VLF results of profile A. The transfer functions exhibit a large shift away from the zero axis. The real part of the transfer function has a negative shift and the imaginary part a positive shift. As a result, the telephone cable anomaly at the beginning of the profile is visible in the data but not resolved by the inversion model. However, a good conducting anomaly is – despite the shift – visible after 150 m in the inversion model. The anomaly begins at the surface and extends to the subsurface becoming broader with increasing depth. Low resistive extensions continue deeper down at the sides of the anomaly than at its centre. The anomaly appears not to result solely from the drainage, because the location of the drainage is from profile meters 150 to 155 but the anomaly in the inversion model expands from 150 to 170 m at the surface. In the subsurface, its extension is even larger: from 130 to 180 m. Although this anomaly and its extension is also visible in the RMT results, it is much more distinct in the VLF data, that is its resistivity contrast is larger with approximately 1 Ohm-m and a surrounding half space of 30 Ohm-m. A subdivision of the subsurface in a highly conductive part (salt water) and less well conductive part (freshwater), as indicated by the RMT and BGR measurements (cf. Figures 68 and 66), is not visible in the inversion model. The shallow anomaly at profile meters 330 to 350 seems to be an artefact, as it is not visible in most other models. Due to the large shifts in the transfer functions, the RMS of the inversion model is 10.27 %.

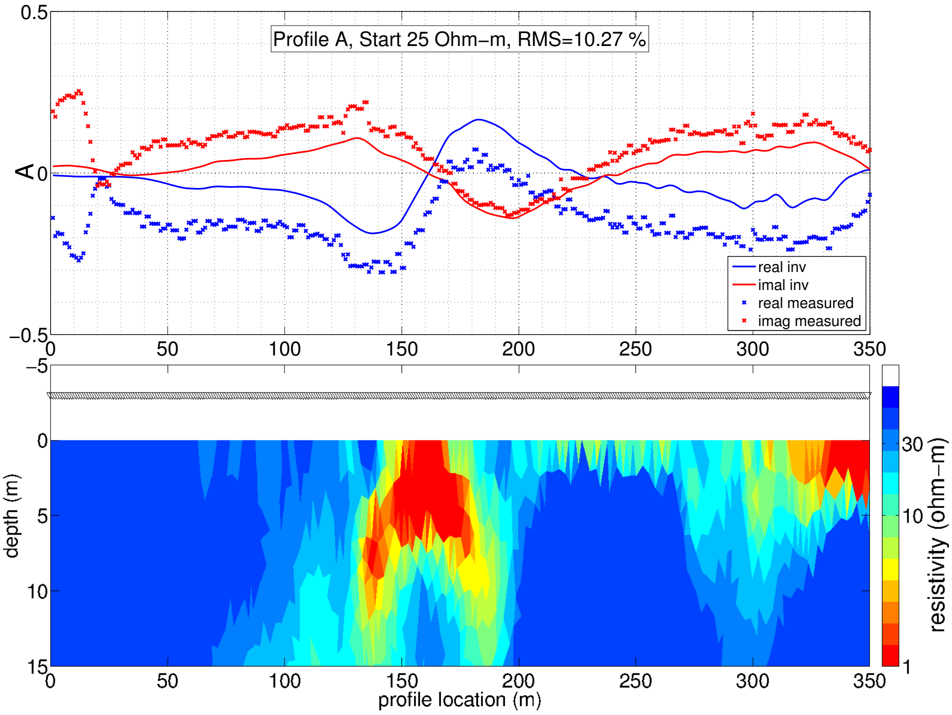

Figure 69: UAS-VLF of profile A: **Top panel:** Tipper component A, real part in blue and imaginary part in red as a function of profile location. **Bottom panel:** Inversion model. Triangles denote sensor location and height above ground. Resistivities as a function of depth and profile location in a logarithmic Ohm-m scale.

Because of the large shift of the transfer functions in Figure 69, Figure 70 shows the inversion result of shifted data (cf. Section 4.7). The shift has no large influence on the form and resistivity value of the anomaly around 150 to 175 m, but the telephone cable at the beginning of the profile is well-resolved. However, the subsurface around the telephone cable has a resistivity of 50 Ohm-m, whereas the area from profile meters 50 to 100 shows resistivities of around 10 Ohm-m. To the right of the anomaly, the background resistivities increase again. This is in accordance with the RMT results, if the 50 Ohm-m around the telephone cable is ignored. The reason why the resistivity value of the subsurface around the telephone cable is probably wrong in the models, is that VLF is mainly sensitive to lateral conductivity changes and thus resistivity contrasts are responsible for the shape of the transfer functions. The inversion generates the subsurface resistivity contrast to reproduce the transfer functions. However, similar transfer function shapes could be obtained if the telephone cable had a lower resistivity and its surroundings, too (important is that the contrast remains similar). After shifting the transfer functions to the zero line, an RMS of 2.4 % is achieved.

This strong increase in the quality of the quantitative explanation of the measured data by inversion of shifted data shows the necessity of a shift correction for measured data and motivates it (cf. Sections 4.7 and 5.2). As there is only one VLF transmitter available in this field campaign (and thus only a scalar analysis of the data is possible), the now presented results are the results of already shift corrected transfer functions (if necessary). Transfer functions determined with one frequency show shifts more often than transfer functions determined by more than one frequency (cf. Section 4.7 and 5.2). Corresponding inversion results of the original data are for the sake of completeness shown in the appendix.

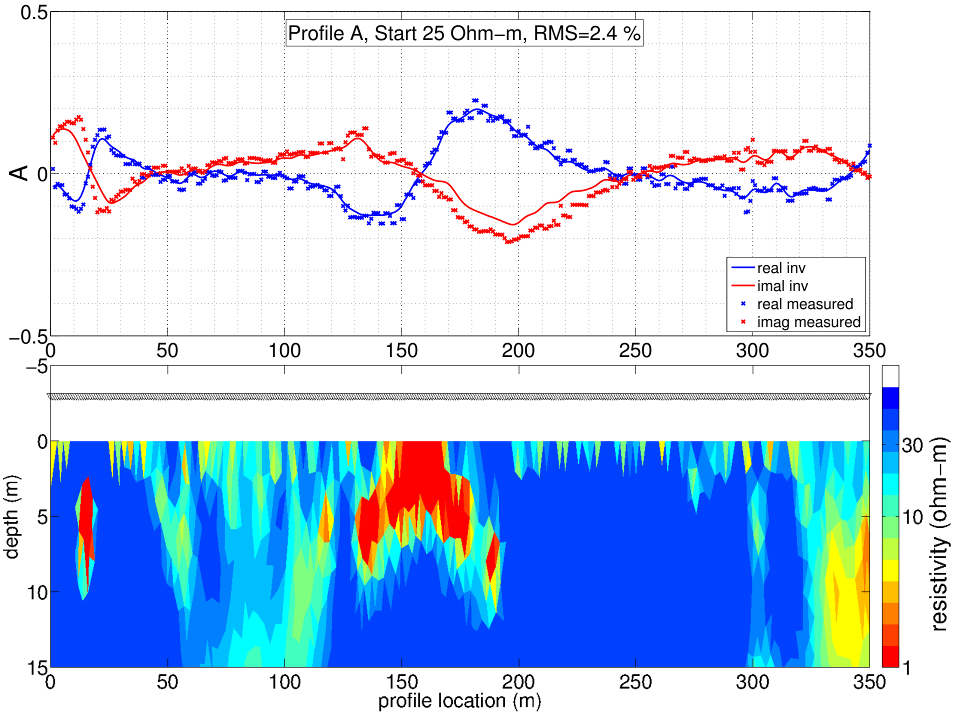

Figure 70: UAS-VLF of profile A, Tipper shifted. **Top panel:** Tipper component A, real part in blue and imaginary part in red as a function of profile location. **Bottom panel:** Inversion model. Triangles denote sensor location and height above ground. Resistivities as a function of depth and profile location in a logarithmic Ohm-m scale. Anomaly of a telephone cable at profile meter 15.

Figure 71 shows the inversion result of the ground-based VLF data of profile A with a station distance of 5 m. The transfer functions show the telephone cable anomaly at profile meter 15 and an anomaly at the assumed position of the transition from salt to freshwater in the range of 140 to 180 m. Additionally, several smaller anomalies are scattered in the subsurface inversion model. These scattered anomalies are probably artefacts resulting from jumps in the measured data. It is noticeable that the imaginary part of the transfer function is much less affected. Possible reasons for jumps in the transfer functions are discussed in Section 4. Also, it should be mentioned that Tipper determined with the scalar method – as it is done here – are much more likely to show jumps (cf. Figure 4.4). The effect of a disturbed transfer function may even be increased by the – compared to the UAS-VLF measurements – small number of data points. Outliers have a stronger impact if the number of data points is small. Additionally, it is more probable that a transmitter changes its transmitting characteristics (due to environmental changes in the path of the EM-waves or due to variations of the transmitted signal in time) during the measurement of a profile. A UAS-VLF measurement for a 350 m profile takes a little less than 6 min, whereas ground-based VLF measurements take almost

1.5 h. Despite all these disturbances, the crucial anomaly (i. e. the transition zone) detected by the UAS-VLF measurement is similar to the anomaly detected by the ground-based VLF measurements regarding position and shape. With an RMS of 2.5 %, the measured data is well explained by the inversion model.

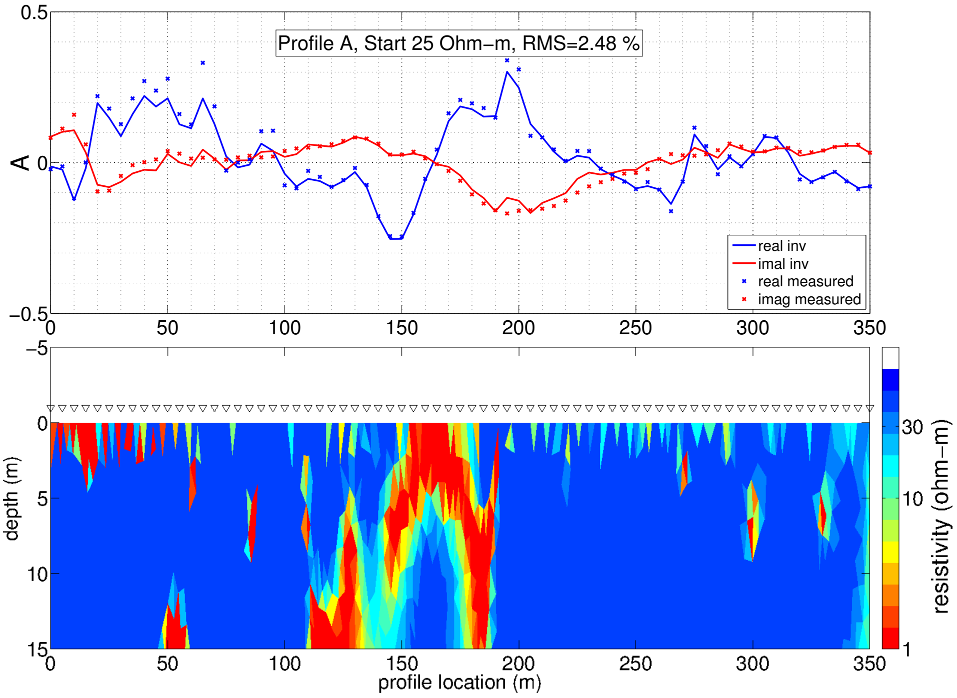

Figure 71: Ground-based VLF of profile A. **Top panel:** Tipper component A, real part in blue and imaginary part in red as a function of profile location. **Bottom panel:** Inversion model. Triangles denote sensor location and height above ground. Resistivities as a function of depth and profile location in a logarithmic Ohm-m scale. Anomaly of a telephone cable at profile meter 15. Several small anomalies due to scattered transfer function.

In Figure 72, a forward model of profile 3 is presented. The shown subsurface model is divided in one area with 5 Ohm-m resistivity at the begin of the profile and one area with 50 Ohm-m at the end of the profile. The area with 50 Ohm-m is slightly higher than the 30 Ohm-m result of the RMT data to investigate the effect of the resistivity contrast. The boundary of the two areas is at 175 m. The transfer functions of the UAS-VLF data are qualitatively reproduced by the forward model in the range of approximately 150 m to 250 m. For the real part of the transfer functions, the amplitudes agree well in the range of 150 m to 180 m, after 180 m the amplitude of the forward modelled transfer function decreases faster than the amplitude of the measured data. For the imaginary part of the transfer functions, the amplitudes agree in the range of 150 m to 170 m, after 170 m the amplitude of the forward modelled transfer function decreases faster than the amplitude of the measured data. However, a small wavelike feature is visible in the imaginary part of the forward modelled transfer function in the range of 170 m to 180 m and a similar feature is visible in the measured data in the range of 180 to 200 m. In contrast, the amplitudes of the Tipper amplitudes left of the transition zone are not explained by the forward model. Additionally, the telephone cable at profile meter 15 is not included in the forward model. These are the reasons why the forward model shows a high RMS of 6.68 %. Altogether, the forward model is not able to explain the UAS-VLF data completely. This indicates that the origin of the measured anomaly is not solely the transition from salt- to freshwater, but some other features (e. g. the anomaly of the drainage) need to be included to fully explain the data. A similar forward model with a 5 Ohm-m and a 30 Ohm-m area is shown in Figure 73. It is noticeable that the amplitudes of the transfer functions remain approximately the same, but the position of the minimum and maximum completely disagree with the transfer functions of UAS-VLF measurement. This indicates that the salt- to freshwater transition zone is located at approximately 175 m, which is more than 20 m away from the drainage.

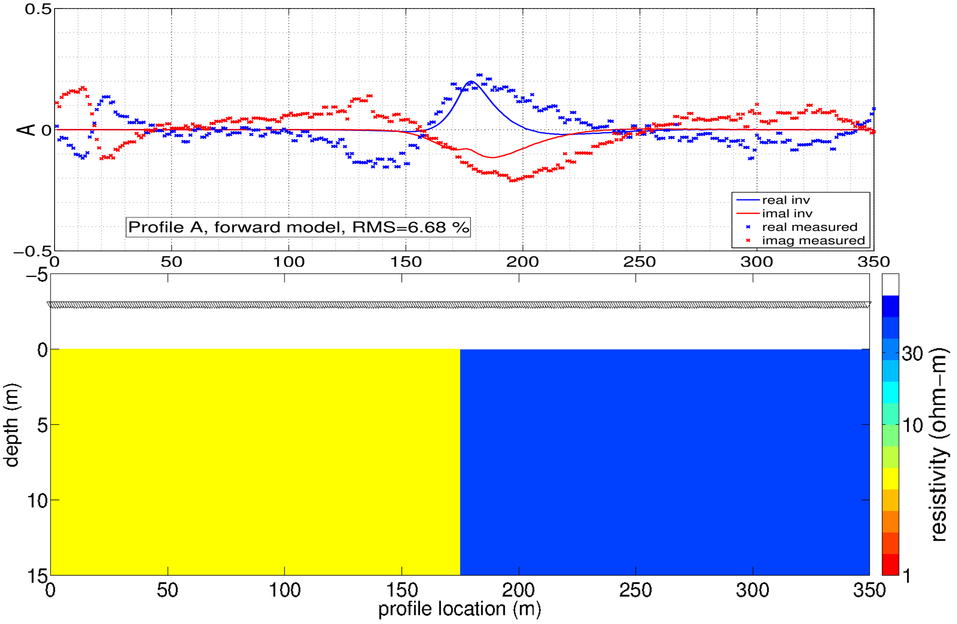

Figure 72: Forward model of profile A, transition (5 Ohm-m to 50 Ohm-m) at 175 m. **Top panel:** Tipper component A, real part in blue and imaginary part in red as a function of profile location. **Bottom panel:** Forward model: Triangles denote sensor location and height above ground. Resistivities as a function of depth and profile location in a logarithmic Ohm-m scale.

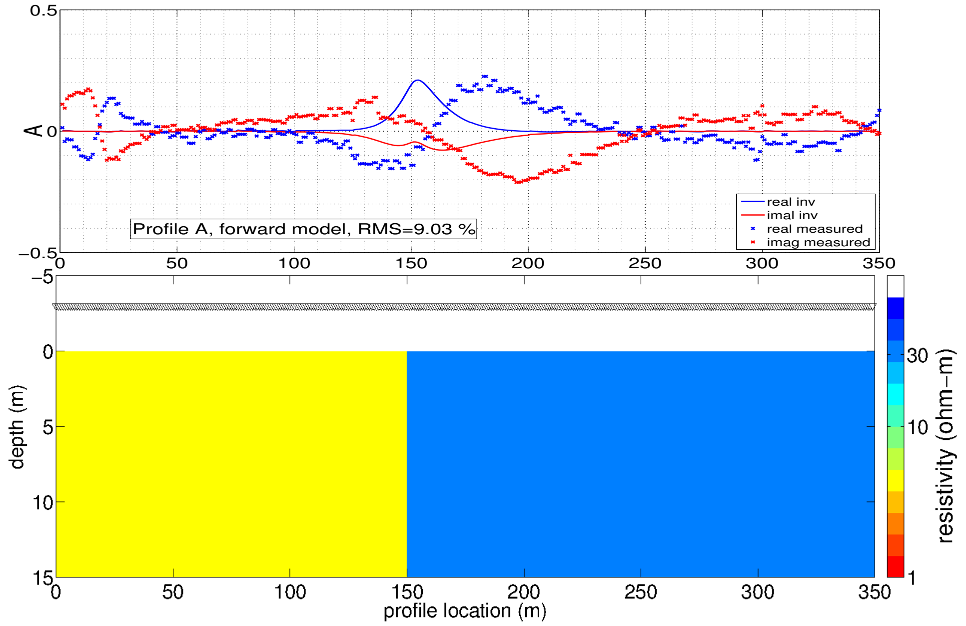

Figure 73: Forward model of profile A, transition (5 Ohm-m to 30 Ohm-m) at 150 m. **Top panel:** Tipper component A, real part in blue and imaginary part in red as a function of profile location. **Bottom panel:** Forward model: Triangles denote sensor location and height above ground. Resistivities as a function of depth and profile location in a logarithmic Ohm-m scale.

Profile B

Figure 74 shows the UAS-VLF results of the neighbouring profile B. They confirm the previous results (a plot of the unshifted data is shown in the appendix in Figure 84). The telephone cable is clearly visible as well as the transition zone. The salt- to freshwater transition zone ranges from 140 to 190 m and its anomaly is less deep at its borders. The expected general gradient from good conductive subsurface at the begin of the profile to less conductive subsurface at the end of the profile is confirmed. With 1.9 % RMS, the inversion explains the data well.

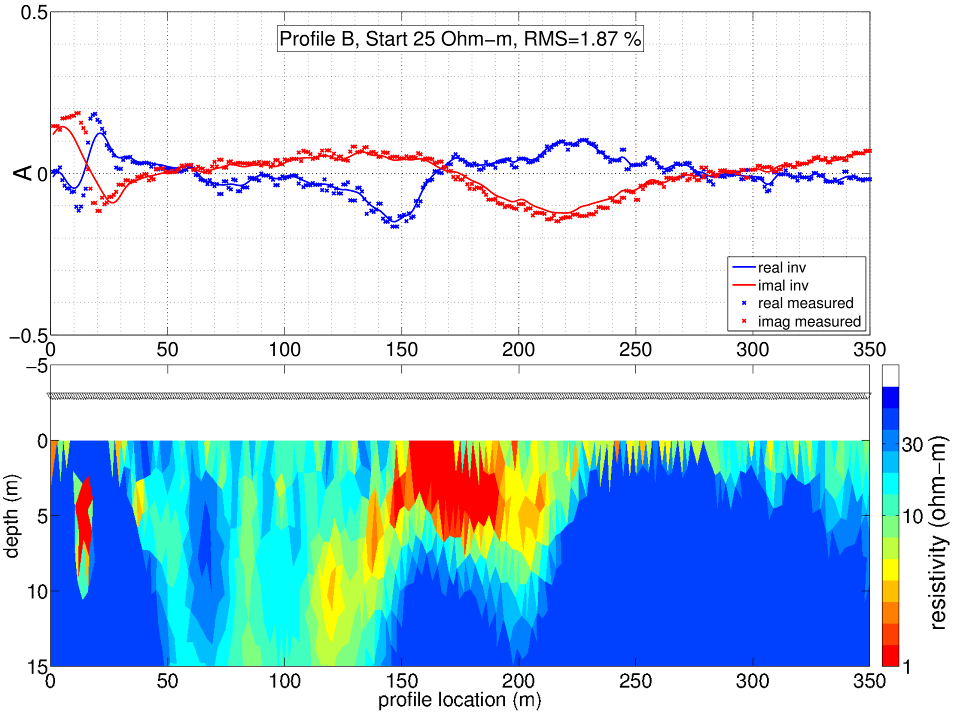

Figure 74: UAS-VLF of profile B, Tipper shifted. **Top panel:** Tipper component A, real part in blue and imaginary part in red as a function of profile location. **Bottom panel:** Inversion model. Triangles denote sensor location and height above ground. Resistivities as a function of depth and profile location in a logarithmic Ohm-m scale. Anomaly of a telephone cable at profile meter 15.

Profile C

Figures 75 to 77 show other data sets that denote the necessity of a shift of the raw data in order to be able to invert the data and obtain a reasonable result. Figure 75 shows the inversion result of the raw data of profile C. It can be seen that the obtained model does not explain the data at all. The model is shown to demonstrate the influence of a shift in the transfer functions on the resulting inversion model.

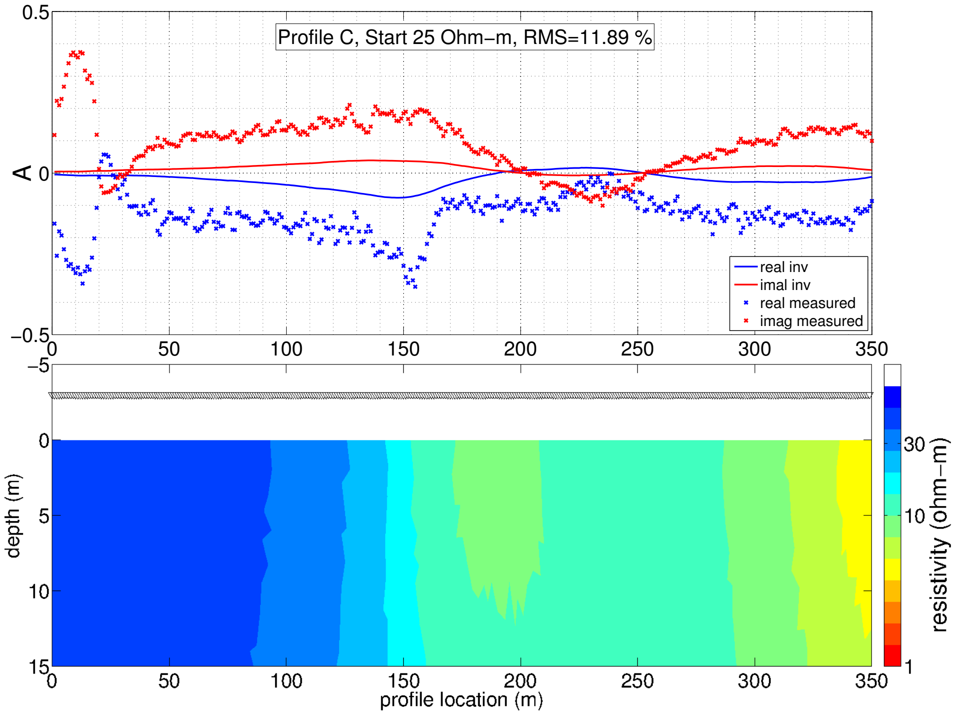

Figure 75: UAS-VLF of profile C. **Top panel:** Tipper component A, real part in blue and imaginary part in red as a function of profile location. **Bottom panel:** Inversion of profile C. Triangles denote sensor location and height above ground. Resistivities as a function of depth and profile location in a logarithmic Ohm-m scale.

In order to obtain a meaningful inversion model, it is necessary to include the transition zone anomaly in the starting model (i. e. a good conductor at profile meters 150 to 200). The result is shown in Figure 76. It contains a deep good conductor at profile meter 15 corresponding to the telephone cable and a shallow good conductor at 150 to 230 m.

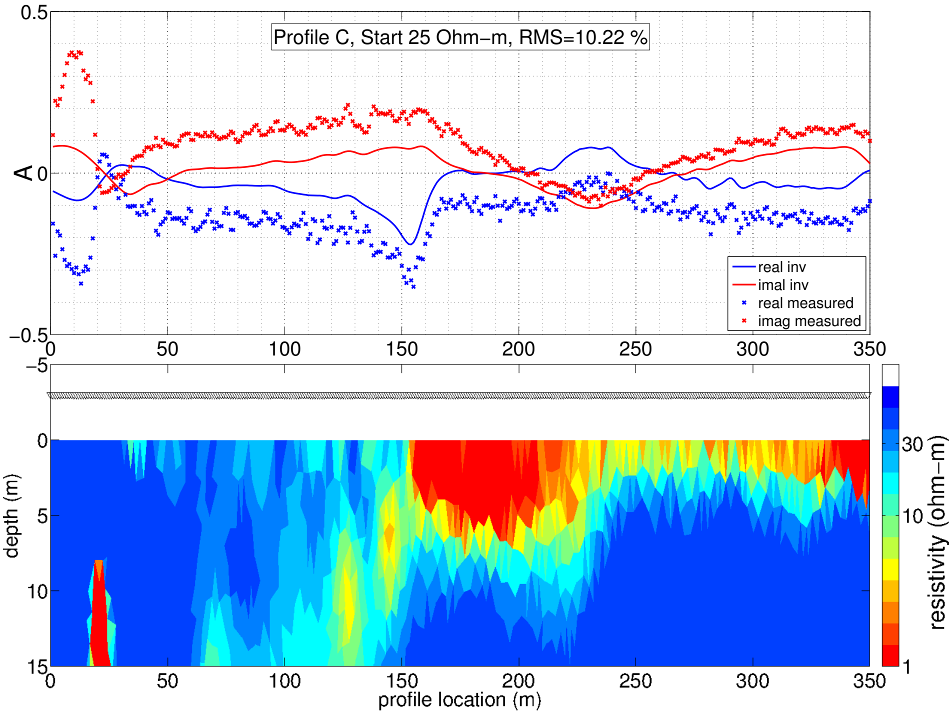

Figure 76: UAS-VLF of profile C, inversion with transition zone included in the start model. **Top panel:** Tipper component A, real part in blue and imaginary part in red as a function of profile location. **Bottom panel:** Inversion model. Triangles denote sensor location and height above ground. Resistivities as a function of depth and profile location in a logarithmic Ohm-m scale. Anomaly of a telephone cable at profile meter 15.

The inversion result obtained with shifted transfer functions is shown in Figure 77. For the shifted data, the same homogeneous half space of 25 Ohm-m is used as starting model as was used for the previous inversions. The telephone cable is resolved and the anomaly corresponding to the transition zone ranges from 150 to 230 m. In contrast to the unshifted model, the telephone cable anomaly is less deep (i. e. is limited in its extension in z-direction) and the anomaly of the transition zone only has a direct contact to the surface at 150 to 175 m. With an RMS of 3 %, the shifted transfer functions show the best fit. However, a negative aspect is the numerous scattered small anomalies resulting from the noisy transfer function. These oscillations of the transfer function probably stem from oscillatory movements of the sensor, which were clearly visible during the flight/measurement. None of the other presented profiles has such strong oscillations during the flight. The cause of the large movements of the sensor was strong wind.

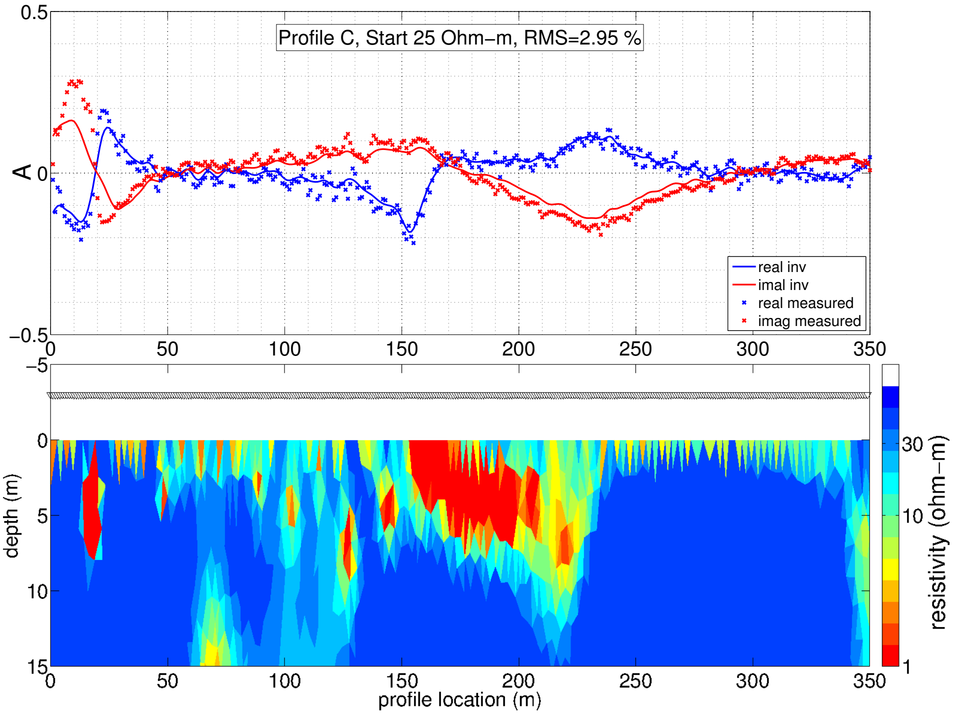

Figure 77: UAS-VLF of profile C, Tipper shifted. **Top panel:** Tipper component A, real part in blue and imaginary part in red as a function of profile location. **Bottom panel:** Inversion model. Triangles denote sensor location and height above ground. Resistivities as a function of depth and profile location in a logarithmic Ohm-m scale. Anomaly of a telephone cable at profile meter 15.

Profile D

Figure 78 shows the transfer functions of the UAS-VLF measurements of profile D (for comparison the unshifted data are shown in the appendix in Figure 85). Both, the telephone cable anomaly and the salt- to freshwater anomaly are clearly visible. It is noticeable that the anomaly of the transition zone lies several meters below the surface and it ranges from 130 to 225 m. It lies deeper than in previous profiles and additionally shows the largest expansion. The gradient from the well conducting salt-water saturated area at the begin of the profile to the less well conducting area to the end of the profile is clearly visible. Again, several small anomalies due to wavelike bumps in the transfer functions are visible. These bumps probably result from oscillatory movements of the sensor. Still, a good fit is achieved with an RMS of 1.2 %.

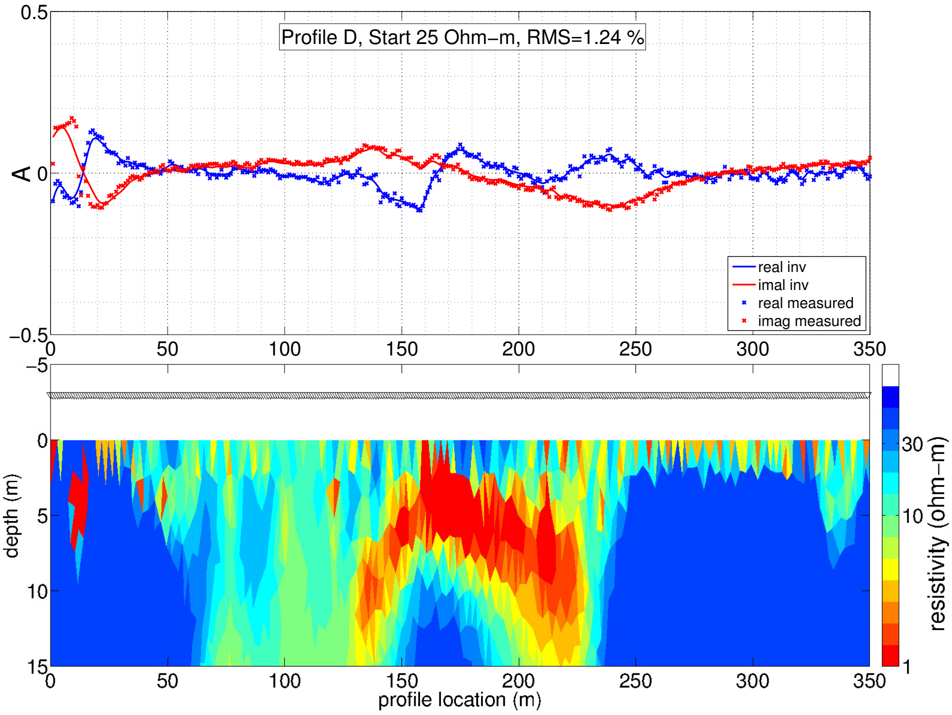

Figure 78: UAS-VLF of profile D, Tipper shifted. **Top panel:** Tipper component A, real part in blue and imaginary part in red as a function of profile location. **Bottom panel:** Inversion model. Triangles denote sensor location and height above ground. Resistivities as a function of depth and profile location in a logarithmic Ohm-m scale. Anomaly of a telephone cable at profile meter 15.

Figure 79 shows the transfer functions of the UAS-VLF measurements (for comparison the unshifted data are shown in the appendix in Figure 86). The transfer functions show the telephone cable anomaly at profile meter 15 and an extended anomaly from profile meter 110 to 230. The area where the resistivity of this anomaly is lowest lies around profile meter 160 to 220. Corresponding to previous models, the obtained inversion model indicates a transition zone anomaly behind the drainage. However, the transition zone anomaly obtained from this ground-based inversion differs from all previous results. It lies deeper in the subsurface and the area with the lowest resistivity ranges from 160 to 220 m. As in the ground-based measurements of profile A (cf. Figure 79), several smaller anomalies are scattered in the subsurface inversion model. An RMS of 2.2 % is achieved.

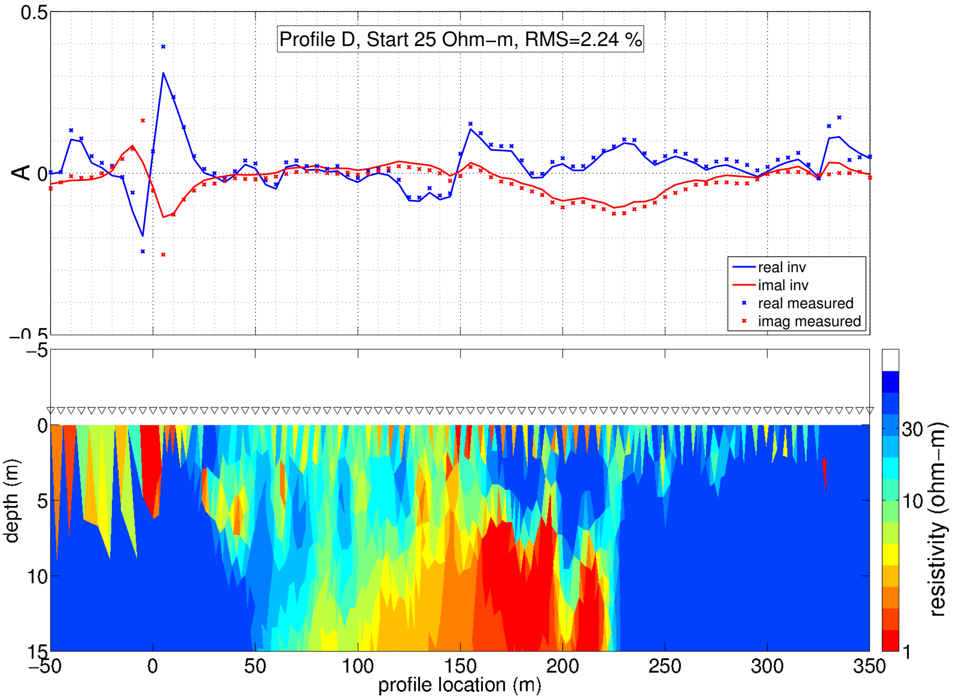

Figure 79: Ground-based VLF of profile D, Tipper shifted. **Top panel:** Tipper component A, real part in blue and imaginary part in red as a function of profile location. **Bottom panel:** Inversion model. Triangles denote sensor location and height above ground. Resistivities as a function of depth and profile location in a logarithmic Ohm-m scale. Extended anomaly due to salt- to freshwater transition at profile meter 110 to 230. Anomaly of a telephone cable at profile meter 15. Several small anomalies due to scattered transfer function.

Discussion of the Cuxhaven Results

The main conclusion of this chapter is that a natural anomaly like the observed salt- to freshwater transition zone is detectable by UAS-VLF measurements. A lateral conductivity change is clearly visible in the Tipper of all presented data. Furthermore, the zero crossing of the transfer functions lies behind the drainage. This indicates that not the drainage itself, which is an anthropogenic anomaly, is the main cause of the anomaly, but something behind the drainage. If the drainage would be the cause (i. e. a good conductor), the zero crossing should be exactly above it (similar to the pipeline and power cable discussed in Section 6.1.1). Additionally it is shown that for shifted transfer functions a homogeneous half-space is sufficient to receive reasonable inversion models.

Furthermore, the RMT data confirm the assumed salt- to freshwater transition zone since the resistivities left of the drainage are smaller than the resistivities to the right of it. At the position of the drainage itself and a few meters behind it, the resistivities drop even a bit more. Simplified, this subdivision in one part good conducting and one part bad conducting is a vertical contact. This vertical contact in the subsurface is not well reproduced by the UAS-VLF measurements. The reason for this is mainly that the resistivity in the first 50 profile meters is similar to the resistivities at the end of the profile. If the first 50 profile meters are ignored, a vertical contact in the subsurface is indicated. An explanation may be that since VLF is mainly sensitive to lateral conductivity changes and thus resistivity contrasts are responsible for the shape of the transfer functions, the inversion creates the required contrast to reproduce the transfer functions. In the case presented here, a good conducting anomaly of approximately 1 Ohm-m is surrounded by a bad conductor. However, the same transfer function could be obtained by an even better conducting anomaly (the anthropogenic anomalies investigated in Section 6.1.1 have values down to 10^{-5} Ohm-m) and a less bad conductor. This means that maybe the first 50 m of the obtained inversion models have to be regarded carefully with respect to their absolute resistivity values.

The forward modelling studies of profile A indicate that the salt- to freshwater transition zone is located at 175 m. However, thus some features of the measured transfer functions are reproduced well by the forward models, others are not. This indicates that the origin of the measured anomaly is not solely the salt- to freshwater transition zone.

7 Summary and Conclusions

In the present thesis, a feasibility study for the applicability of using the geophysical VLF method together with an unmanned aircraft is performed. The strength of the geophysical VLF method is the fast and low cost mapping of near-surface structures [Gharibi and Pedersen, 1999]. The advantages of a UAS are that it can to fly over heavily structured or dangerous terrain and it can fly at low altitudes. Instrument and platform combined are a safe, low cost, and high speed geophysical surveying method. For the first time ever the VLF method is used with an unmanned helicopter in the present thesis.

To be able to conduct UAS-VLF measurements, pre flight experiments needed to be conducted. The provided information enabled the construction of a suitable suspension for the VLF devices. Additionally, a processing algorithm is presented to determine the magnetic transfer functions. In a first field campaign, the capability of UAS-VLF to detect buried anthropogenic anomalies is demonstrated. A second field campaign shows the capability of UAS-VLF to detect a salt- to freshwater transition zone. As a reference, ground-based VLF and RMT measurements are carried out in both survey areas. Both field campaigns were carried out in cooperation with *Mobile Geophysical Technologies*. Modelling and inversion for both survey areas is conducted to provide a quantitative interpretation of the magnetic transfer functions.

The used VLF devices, the *ADU* data logger and the *SHFT* Sensor from *metronix*, are mounted on the unmanned helicopter *Scout B1-100* from *Aeroscout*. To determine the requirements of the suspension needed for this, pre-flight investigations are carried out. The effect of sensor rotations is investigated. The result is that transfer functions are very sensitive to rotations. Small sensor rotations of a few degree already have a non-negligible impact on the transfer functions. Furthermore, noise measurements of the devices are presented, discovering that the *ADU* data logger must have a minimum distance of 2 m and the *SHFT* sensor of 4 m to the helicopter. A suspension that takes these information into account is developed. The suspension is developed in cooperation with *Aeroscout* and *Mobile Geophysical Technologies*. A suitable suspension is finally constructed by *Aeroscout*. Additionally, the weight of sensor and logger is reduced to ensure airworthiness of the UAS. This reduction is realized by *Mobile Geophysical Technologies* in cooperation with *metronix*.

The developed computer code to process the UAS-VLF data is described step by step. Two approaches, to determine the transfer functions, a bivariate and a scalar one, are applied and their results compared. The bivariate determination of the transfer functions proposed by Pedersen et al. [1994] is superior to the scalar determination. The transfer functions determined by the bivariate method show less distortions, they are smoother, and are less susceptible to shifts. As an additional problem, the necessity to identify suitable transmitters for the analysis arose. It is necessary to pinpoint all available transmitters in a survey area and identify the transmitters that can be used to determine the transfer functions. For this, an algorithm is developed which compares the transmitter amplitudes to the background noise level. A method to illustrate transmitter availability in a survey area is presented. The resulting transfer functions of the developed processing algorithm are compared to the results of an algorithm from Becken [2013]. Both results agree well. However, the transfer functions determined with the algorithm developed in this thesis are less smooth. A rotation of the transfer functions is performed in order to be able to interpret the transfer functions with the 2D inversion algorithm MARE2DEM. For this, one component of the Tipper is minimized and the other is maximized. As a last step in the processing chain, shifts in the transfer functions are investigated and a technical method to compensate the shifts is presented. The applied method calculates the average of the transfer functions over a profile. Subsequently, the transfer functions are shifted towards the zero axis by this average value. Inversion results obtained with the shifted transfer functions are superior to the results of the unshifted transfer functions, because in some cases an inversion with the unshifted data is not able to explain the subsurface anomalies. However, a shift is not always necessary to obtain realistic subsurface models but because the inversion models are not able to reproduce the shift in the data, the resulting models show a large RMS.

A first proof-of-concept study with UAS-VLF measurements was carried out in Wavre, Switzerland. The test site contains two anthropogenic anomalies. The UAS-VLF system is able to detect the buried anomalies and determine their locations correctly. For the first time, inversion and modelling of measured UAS-VLF with an unmanned helicopter is conducted. The RMT data is used to determine the background resistivity for the VLF inversions in both surveys. A comparison of the UAS-VLF transfer functions and inversion results with ground-based VLF and RMT data is performed. The positions of the anomalies of UAS-VLF, ground-based VLF, and RMT agree well. Additionally, a forward model that includes a priori information is able to explain the measured data well. The influences of sensor height and displacement currents in inversions of UAS-VLF data are investigated – both have negligible effects on the outcome of the inversion models.

In a second campaign, the capability of the UAS-VLF method to detect a salt- to freshwater transition zone is investigated. The UAS-VLF method is able to identify the location of the transition zone correctly. Modelling and inversion of the UAS-VLF data is conducted. For this, in some cases it is necessary to handle shifts in the transfer functions. The received models agree well with the a priori information from BURVAL [2003], but the exact location of the transition zone deviates by 25 m from the expected position. This deviation is approved by a forward model that reproduces the location and resistivities of the transition zone. However, the forward model is not able to reproduce the transfer functions of the measured data completely and the obtained inversion models show some disagreements with the forward model, mainly a good conductor at the contact of the two zones of different resistivities. The comparison of the position of the transition zone anomaly from the UAS-VLF transfer functions and inversion results to that from ground-based VLF and RMT data shows a good agreement.

Worldwide for the first time, successfully carried out VLF measurements with an unmanned helicopter are presented. The measurements demonstrate the capability of the UAS-VLF method to detect buried anthropogenic anomalies and a salt- to freshwater transition zone. Although the amplitudes of subsurface anomalies in the transfer functions decrease with altitude, the anomalies are still clearly detectable with the UAS-VLF method. It is demonstrated that the UAS-VLF method is capable of finding anomalies in the subsurface and determining their locations. The combined advantages of UAS and the VLF method promise to become a powerful geophysical tool for fast mapping of near-surface resistivity structures.

8 Outlook

The present thesis demonstrates the feasibility of UAS-VLF measurement. This opens a lot of possible research paths. In the following, ideas for further research are depicted.

Further investigations to continue the development of the UAS-VLF method could be to study the effect of different sensor heights above the ground. This would enable to find out to what degree the amplitudes in the transfer functions decrease with altitude. Observations of a survey area at different altitudes might even provide additional information of the subsurface [Eppelbaum and Mishne, 2011]. For this, a field study combined with a forward modelling investigation could be suitable, since possible effects of sensor height are easier to study if the composition of the subsurface is known.

Furthermore, it could be beneficial to investigate what the (physical) origin of shifts in the transfer functions is which appear mainly in the scalar analysis and why a bivariate analysis prohibits these shifts. Understanding these effects can help to interpret the magnetic transfer functions. In this context, it would be interesting to find out why the bivariate analysis seems to reduce effects on the transfer functions originating from the sensor rotations. It would be ideal to repeatedly measure one profile at a survey area where many VLF transmitters are available. This way, transfer functions derived from varying sensor orientations could be compared. Additionally, measurements with different UAS velocities and at different times could be compared. This may improve the understanding of the effects behind shifts in the transfer functions and time dependencies of the transfer functions.

Additional information could be derived by a VLF-UAS measurement with an inclinometer installed on the sensor. This inclinometer information could permit to find correlations of gyrations in the transfer functions. The goal would be the development of a method to compensate rotational effects in the transfer functions in real time. Another possibility to obtain smoother transfer functions is to refine the processing algorithm developed in the present thesis (e. g. to apply a filter like the Fraser filter [Fraser, 1969]).

Furthermore, the effect of the electromagnetic helicopter noise can be investigated in more detail, taking into account the the effect of the gas supply of the helicopter. Detailed knowledge of the noise could provide an optimization of the suspension.

Additional studies could be conducted to investigate the effect of an inversion with several frequencies for typical UAS sensor heights (2 m - 10 m) as it is done in Pedersen and Oskooi [2004]. Similar investigations could be done using only the real and the imaginary part, respectively, of the transfer functions to conduct an inversion. Knowledge of the impact of these various inversion approaches can help to interpret the inversion models obtained with measured UAS-VLF data. In order to combine the strengths of RMT (information of the subsurface resistivity distribution), and UAS-VLF (fast mapping and information of location of lateral conductivity changes), a joint inversion of UAS-VLF and RMT data could be done. Furthermore, it would be interesting to conduct a 3D inversion of the UAS-VLF data. This could give information about the capability of UAS-VLF data to resolve 3D anomalies. Another approach to analyse UAS-VLF data is to derive current density pseudo-depth sections [Ogilvy and Lee, 1991] or to transform UAS-VLF data into maps of apparent resistivity and phase [Becken and Pedersen, 2003]. This was not done in the current thesis, but would provide additional information of subsurface structures.

References

Aeroscout, 2014. Product Brochure Aeroscout Scout B1-100 UAV Helicopter, http://www.aeroscout.ch/downloads/Aeroscout_Scout_B1-100_Brochure.pdf.

Austin, R., 2011. *Unmanned aircraft systems: UAVs design, development and deployment*, vol. 54, John Wiley & Sons.

Bastani, M. and Pedersen, L., 2001. Estimation of magnetotelluric transfer functions from radio transmitters, *Geophysics*, **66**(4), 1038–1051.

Becken, M., 2013. Personal communication.

Becken, M. and Pedersen, L. B., 2003. Transformation of VLF anomaly maps into apparent resistivity and phase, *Geophysics*, **68**(2), 497–505.

Bloomfield, P., 2004. *Fourier analysis of time series: an introduction*, John Wiley & Sons.

Bosch, F. and Müller, I., 2005. Improved karst exploration by VLF-EM-gradient survey: comparison with other geophysical methods, *Near Surface Geophysics*, **3**(4), 299–310.

Brasse, H., 2007. Manuskript zur vorlesung methoden der geoelektrischen und elektromagnetischen tiefensondierung, *Freie Universität Berlin*.

BURVAL, 2003. Bremerhaven-Cuxhavener Rinne survey, http://www.bgr.bund.de/EN/Themen/GG_Geophysik/Aerogeophysik/Projekte/abgeschlossen/BURVAL/BurVal_Project.html?nn=1555670.

Cagniard, L., 1953. Basic theory of the magneto-telluric method of geophysical prospecting, *Geophysics*, **18**(3), 605–635.

Chave, A. D. and Jones, A. G., 2012. *The magnetotelluric method: Theory and practice*, Cambridge University Press.

Clarke, R., 2014. Understanding the drone epidemic, *Computer Law & Security Review*, **30**(3), 230–246.

Colomina, I. and Molina, P., 2014. Unmanned aerial systems for photogrammetry and remote sensing: A review, *ISPRS Journal of Photogrammetry and Remote Sensing*, **92**, 79–97.

Constable, S. C., Parker, R. L., and Constable, C. G., 1987. Occam's Inversion: a practical algorithm for generating smooth models from EM sounding data, *Geophysics*, **52**(3), 289–300.

Egbert, G. D. and Booker, J. R., 1986. Robust estimation of geomagnetic transfer functions, *Geophysical Journal International*, **87**(1), 173–194.

Eppelbaum, L. and Mishne, A., 2011. Unmanned Airborne Magnetic and VLF Investigations: Effective Geophysical Methodology for the Near Future, *Positioning*, **2011**.

Eröss, R., Stoll, J., Bergers, R., and Tezkan, B., 2013. Three-component VLF using an unmanned aerial system as sensor platform, *First Break*, **31**(7), 33–41.

Fraser, D., 1969. Contouring of VLF-EM data, *Geophysics*, **34**(6), 958–967.

Gharibi, M. and Pedersen, L. B., 1999. Transformation of VLF data into apparent resistivities and phases, *Geophysics*, **64**(5), 1393–1402.

Google-earth, 2008. Aerial view at location near Cuxhaven, Germany.
53°45'58.7"N 8°32'51.5"E, Eye alt 458 feet.

Google-earth, 2012. Aerial view at location in Wavre, Switzerland.
47°01'29.6"N, 7°01'02.8"E, Eye alt 676 feet.

Hansen, P., Pereyra, V., and Scherer, G., 2012. *Least Squares Data Fitting with Applications*, Least Squares Data Fitting with Applications, Johns Hopkins University Press.

Hansen, P. C. and O'Leary, D. P., 1993. The use of the L-curve in the regularization of discrete ill-posed problems, *SIAM Journal on Scientific Computing*, **14**(6), 1487–1503.

Harris, F. J., 1978. On the use of windows for harmonic analysis with the discrete Fourier transform, *Proceedings of the IEEE*, **66**(1), 51–83.

ICAO, 2011. International Civil Aviation Organization, cir 328 an/190 edn.

Jackson, J. D., 1975. Classical Electrodynamics.

Key, K., 2014. Personal communication.

Key, K. et al., 2012. Marine EM inversion using unstructured grids: a 2D parallel adaptive finite element algorithm, in *2012 SEG Annual Meeting*, Society of Exploration Geophysicists.

Key, K. and Ovall, J., 2011. A parallel goal-oriented adaptive finite element method for 2.5-D electromagnetic modelling, *Geophysical Journal International*, **186**(1), 137–154.

Kipfinger, R. P., 1998. Unmanned airborne vehicle (UAV): flight testing and evaluation of two-channel E-field very low frequency (VLF) instrument., *U.S. GEOLOGICAL SURVEY*.

Logachev, A. and Hawkes, H., 1946. The development and applications of airborne magnetometers in the USSR, *Geophysics*, **11**(2), 135–147.

Mackie, R., Rieven, S., and Rodi, W., 1997. Users manual and software documentation for two-dimensional inversion of magnetotelluric data, GSY-USA, *Inc., San Francisco, Calif*.

Mackie, R. L., Madden, T. R., and Wannamaker, P. E., 1993. Three-dimensional magnetotelluric modeling using difference equations-theory and comparisons to integral equation solutions, *Geophysics*, **58**(2), 215–226.

Madden, T. R., 1972. Transmission Systems and Network Analogies to Geophysical Forward and Inverse Problems., Tech. rep., DTIC Document.

metronix ADU, 2014. ADU-07e-Overview,
http://www.geo-metronix.de/mtxgeo/index.php/adu-07e-logger.

metronix SHFT, 2014. SHFT-02e-Overview,
http://www.geo-metronix.de/mtxgeo/index.php/shft-02e-sensors-menu.

Ogilvy, R. and Lee, A., 1991. Interpretation of VLF-EM in-phase data using current density pseudo-sections, *Geophysical Prospecting*, **39**(4), 567–580.

Paal, G., 1965. Ore prospecting based on VLF-radio signals, *Geoexploration*, **3**(3), 139–147.

Pedersen, L. and Dynesius, L., 2008. Final report on the Multi Frequency VLF/LF receiver (MFR) project,.

Pedersen, L., Qian, W., Dynesius, L., and Zhang, P., 1994. An airborne tensor VLF system. From concept to realization, *Geophysical Prospecting*, **42**(8), 863–883.

Pedersen, L. B. and Oskooi, B., 2004. Airborne VLF measurements and variations of ground conductivity: a tutorial, *Surveys in Geophysics*, **25**(2), 151–181.

Pedersen, L. B., Persson, L., Bastani, M., and Byström, S., 2009. Airborne VLF measurements and mapping of ground conductivity in Sweden, *Journal of applied geophysics*, **67**(3), 250–258.

Polak, E., 1971. *Computational methods in optimization: a unified approach*, vol. 77, Academic press.

Radic, T. and Aschmann, L., 1998. Z/H measurement in the radio-frequency range (10 kHz up to 1 Mhz), *Tagungsband zur EEGS*, pp. 887–890.

Recher, S., 2002. *Dreidimensionale Erkundung von Altlasten mit Radio-Magnetotellurik-Vergleiche mit geophysikalischen, geochemischen und geologischen Analysen an Bodenproben aus Rammkernsondierungen*, Ph.D. thesis, University of Cologne.

Rodi, W. and Mackie, R. L., 2001. Nonlinear conjugate gradients algorithm for 2-D magnetotelluric inversion, *Geophysics*, **66**(1), 174–187.

Schmucker, U. and Weidelt, P., 1975. Electromagnetic induction in the earth, *Lecture Notes, Aarhus Univ., Denmark*.

Scholl, C., 2005. *The influence of multidimensional structures on the interpretation of LOTEM data with one-dimensional models and the application to data from Israel*, Ph.D. thesis, University of Cologne.

Telford, W., Geldart, L., and Sheriff, R., 1990. *Applied Geophysics*, Monograph series, Cambridge University Press.

Tezkan, B., Hördt, A., and Gobashy, M., 2000. Two-dimensional radiomagnetotelluric investigation of industrial and domestic waste sites in germany, *Journal of Applied Geophysics*, **44**(2), 237–256.

Tezkan, B., Stoll, J., Bergers, R., and Grossbach, H., 2011. Unmanned aircraft systems: a new geophysical measuring platform for aeromagnetic surveys., *First Break*, **V. 29**, 103–105.

Tikhonov, A. N. and Arsenin, V. Y., 1977. *Solutions of ill-posed problems*, V. H. Winston & Sons.

Vozoff, K., 1972. The magnetotelluric method in the exploration of sedimentary basins, *Geophysics*, **37**(1), 98–171.

Ward, S. H. and Hohmann, G. W., 1988. Electromagnetic theory for geophysical applications, *Electromagnetic methods in applied geophysics*, **1**, 131–311.

Appendix

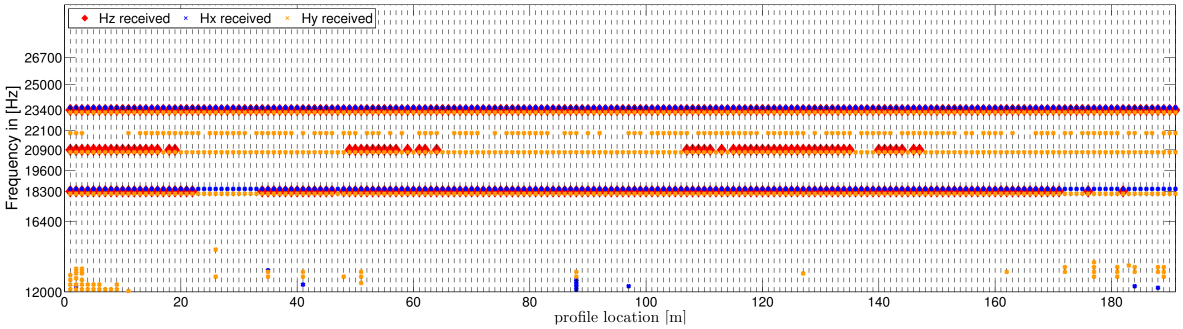

Figure 80: Overview of the transmitter availability during the VLF measurement of profile 3. On the y-axis frequencies of common VLF transmitters are denoted. The x-axis shows the location along the profile. Resolved transmitters receive colour marks. Red dots mark the H_z, blue dots mark the H_x and yellow dots mark the H_y component of the magnetic field. The 18.3 kHz and 23.4 kHz frequencies are used to determine the transfer functions.

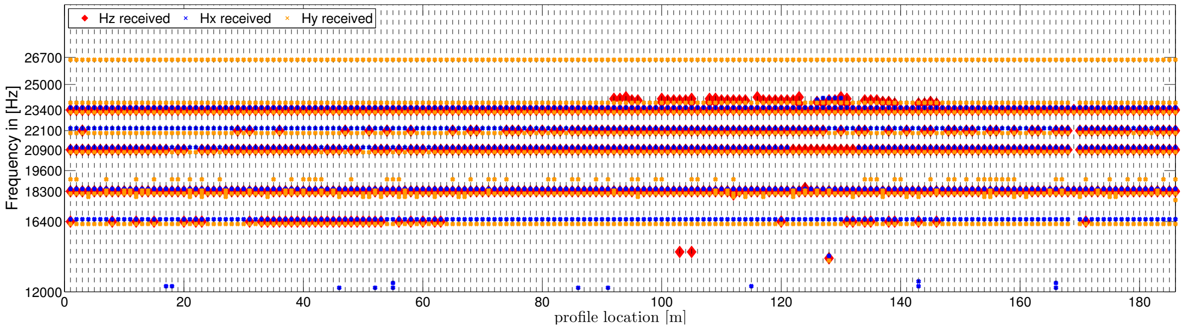

Figure 81: Overview of the transmitter availability during the VLF measurement of profile 4. On the y-axis frequencies of common VLF transmitters are denoted. The x-axis shows the location along the profile. Resolved transmitters receive colour marks. Red dots mark the H_z, blue dots mark the H_x and yellow dots mark the H_y component of the magnetic field. The 18.3 kHz, 20.9 kHz, and 23.4 kHz frequencies are used to determine the transfer functions.

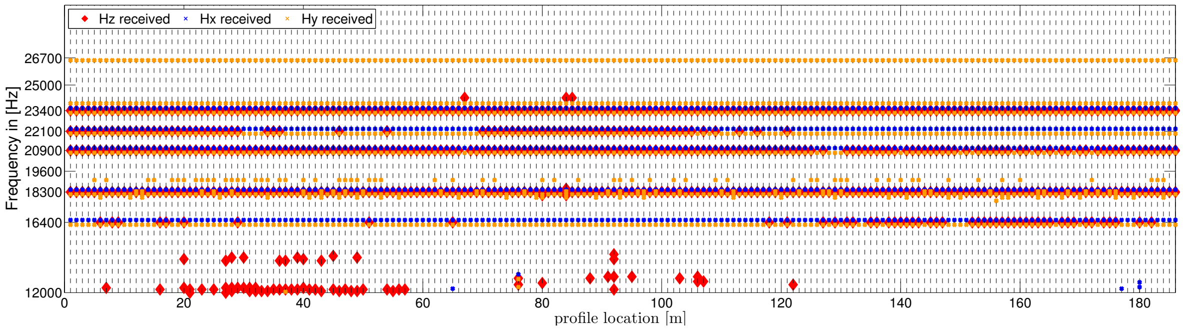

Figure 82: Overview of the transmitter availability during the VLF measurement of profile 5. On the y-axis frequencies of common VLF transmitters are denoted. The x-axis shows the location along the profile. Resolved transmitters receive colour marks. Red dots mark the H_z, blue dots mark the H_x and yellow dots mark the H_y component of the magnetic field. The 18.3 kHz, 20.9 kHz, and 23.4 kHz frequencies are used to determine the transfer functions.

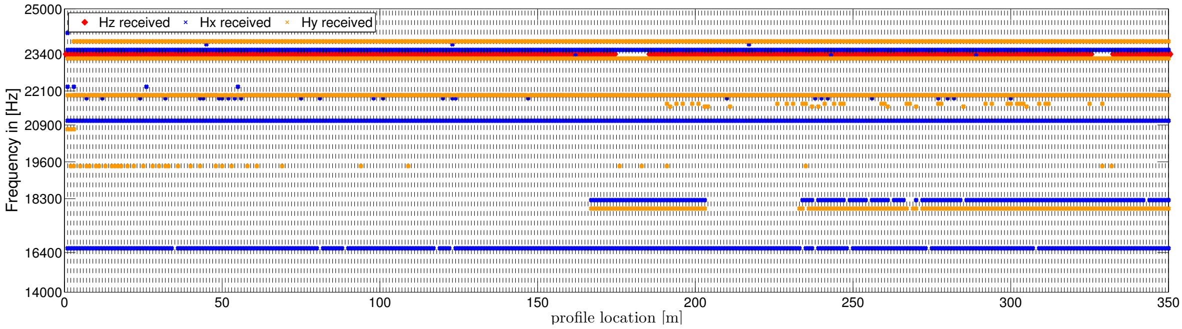

Figure 83: Overview of the transmitter availability during the VLF measurement of profile A. On the y-axis frequencies of common VLF transmitters are denoted. The x-axis shows the location along the profile. Resolved transmitters receive colour marks. Red dots mark the H_z, blue dots mark the H_x and yellow dots mark the H_y component of the magnetic field. Only the 23.4 kHz frequency is used to determine the transfer functions.

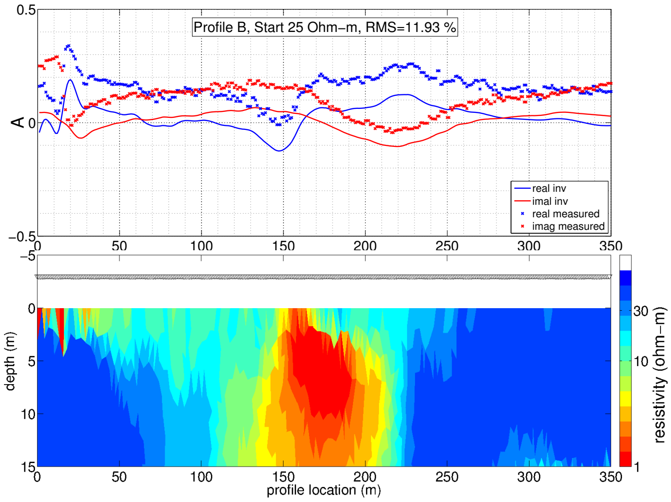

Figure 84: UAS-VLF of profile B. **Top panel:** Tipper component A, real part in blue and imaginary part in red as a function of profile location. **Bottom panel:** Inversion model. Triangles denote sensor location and height above ground. Resistivities as a function of depth and profile location in a logarithmic Ohm-m scale. Anomaly of a telephone cable at profile meter 15. Anomaly of a telephone cable at profile meters 15.

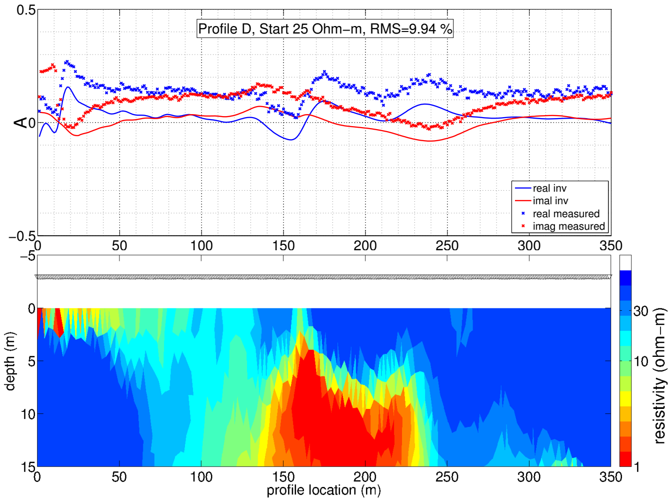

Figure 85: UAS-VLF of profile D. **Top panel:** Tipper component A, real part in blue and imaginary part in red as a function of profile location. **Bottom panel:** Inversion model. Triangles denote sensor location and height above ground. Resistivities as a function of depth and profile location in a logarithmic Ohm-m scale. Anomaly of a telephone cable at profile meter 15. Anomaly of a telephone cable at profile meters 15.

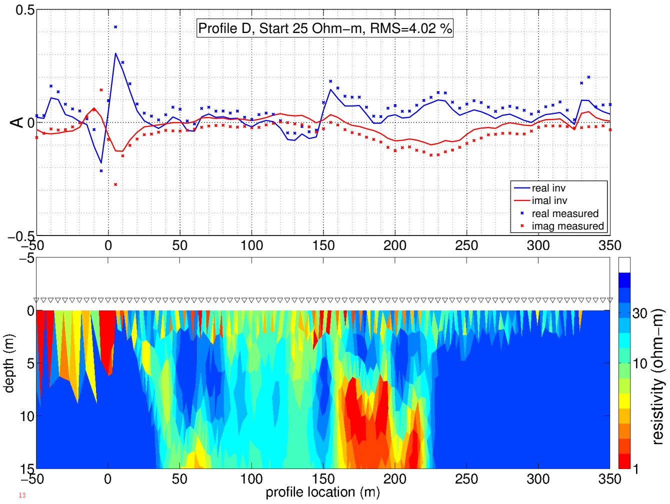

Figure 86: Ground-based VLF of profile D. **Top panel:** Tipper component A, real part in blue and imaginary part in red as a function of profile location. **Bottom panel:** Inversion model. Triangles denote sensor location and height above ground. Resistivities as a function of depth and profile location in a logarithmic Ohm-m scale. Anomaly of a telephone cable at profile meter 15. Anomaly of a telephone cable at profile meters 15. Several small anomalies due to scattered transfer function.

Danksagung

Als erstes möchte ich mich bei meinem Betreuer Prof. Dr. Bülent Tezkan bedanken. Er hat mich in den letzten Jahren begleitet und unterstützt und damit diese Arbeit ermöglicht. Auch in schwierigen Zeiten stand er mir bei und half mir mit seiner Zuversicht weiter.

Prof. Dr. Andreas Junge möchte ich für die Übernahme des Koreferats danken.

Rainer Bergers möchte ich für die Hilfe bei Planung der Messungen und deren Durchführung danken. Er hatte nicht nur diverse gute Ideen sondern auch für jedes auftauchende Hindernis eine passende Lösung parat.

Natalie möchte ich für ihre Unterstützung als SHK während und nach den Messkampagnen danken. Mein Dank geht auch an Sudha mit der stets eine konstruktive und positive Zusammenarbeit möglich war.

Ohne Johannes Stoll wäre diese Arbeit nicht zustande gekommen. Er war von Beginn an beteiligt und machte die Realisierung des Messungen erst möglich. Christoph Eck und seinem Team möchte ich für die tolle Zusammenarbeit danken. Für die Entwicklung einer Aufhängung für die Messgeräte und das stets positive und konstruktive Miteinander möchte ich meine Wertschätzung ausdrücken. Den Beteiligten aus der Firma *metronix* möchte ich für das zur Verfügung stellen der Messgeräte danken.

Für ihre konstruktiven Beiträge möchte ich Jochen Kamm, Kerry Key, Fernando Monteiro Santos, Michael Becken und Laust Pedersen danken. Meinen großen Dank möchte ich Amir, Mitch, Oliver, Jan, Pritam, Marc, Juliane und Sonja ausdrücken, die mich im Endspurt der Arbeit tatkräftig unterstützt haben.

Ein spezieller Dank geht an Klaus, mit dem ich gerne das Büro geteilt habe und der schnörkellos half wenn er konnte. Lorenz, Amir, Anne, Juliane, Aljona und Shari danke ich für vielen Stunden die wir außerhalb der Uni miteinander verbracht haben.

Ganz besonders genossen habe ich die Unterstützung von Michael. Der mich bei unseren täglichen Mensabesuchen nicht selten in der Spur hielt wenn es mal turbulent wurde und auch außerhalb der Universität stets für mich da war. Auch Lukas möchte ich danken, der mich freundschaftlich durch diese Jahre begleitet hat. Als meinem persönlichen Fels in der Brandung möchte ich Jan Jikeli danken. Er war für mich da wie es kein anderer sein konnte.

Für ihre Geduld und Unterstützung möchte ich Sonja danken und meiner Familie, die stets an mich geglaubt hat.

Diese Forschungsarbeit wurde gefördert durch das *Geotechnologien* Programm des Bundesministeriums für Bildung und Forschung. Sie basiert auf einer gemeinsamen Initiative des Bundesministeriums für Bildung und Forschung und der Deutschen Forschungsgemeinschaft.

Erklärung

Ich versichere, dass ich die von mir vorgelegte Dissertation selbständig angefertigt, die benutzten Quellen und Hilfsmittel vollständig angegeben und die Stellen der Arbeit einschließlich Tabellen, Karten und Abbildungen, die anderen Werken im Wortlaut oder dem Sinn nach entnommen sind, in jedem Einzelfall als Entlehnung kenntlich gemacht habe; dass diese Dissertation noch keiner anderen Fakultät oder Universität zur Prüfung vorgelegen hat; dass sie abgesehen von unten angegebenen Teilpublikationen noch nicht veröffentlicht worden ist sowie, dass ich eine solche Veröffentlichung vor Abschluss des Promotionsverfahrens nicht vornehmen werde. Die Bestimmungen dieser Promotionsordnung sind mir bekannt. Die von mir vorgelegte Dissertation ist von Prof. Dr. Bülent Tezkan betreut worden.

Köln, den 27. April 2015

Teilpublikationen

Eröss, R., Stoll, J., Bergers, R., & Tezkan, B., 2013. Three-component VLF using an unmanned aerial system as sensor platform, First Break, 31(7), 33–41.